INSTITUTE OF PHYSICS, POLISH ACADEMY OF SCIENCES

DOCTORAL THESIS

Zero-energy modes in ferromagnetic topological crystalline insulators

---

Author:
Grzegorz P. MAZUR

Advisor:
Prof. dr hab.
Maciej SAWICKI

Auxillary advisor:
Dr. Krzysztof DYBKO

May 27, 2019

The work was supported by the Polish National Science Center Grants

PRELUDIUM (2015/19/N/ST3/02626)
ETIUDA (2017/24/T/ST3/00501)

Part of the work was supported by the International Research Centre MagTop funded by the Foundation for Polish Science through the IRA Programme financed by EU within SG OP Programme.

"I love to talk about nothing. It's the only thing I know anything about."

Oscar Wilde

Abstract

This Ph.D. thesis focuses on the area of topological crystalline insulators (TCIs). TCIs are a unique class of topological insulators, which hosts gapless boundary states due to mirror symmetry of the crystal. Material studied here is SnTe, a valley-degenerate, narrow gap semiconductor which realizes a TCI state. A great deal of attention given to topological materials comes from the possibility of generating non-abelian excitations in a topological matter in a superconducting state. Unexpectedly series of experiments found that a junction between metal and topological material resembles characteristics of superconducting point contact in virtually all the classes of topological matter. Some of the reports additionally claim to observe zero-bias conductance peaks. As zero-bias conductance peaks are often linked with non-abelian excitations in a superconductor these findings were interpreted as interfacial superconductivity formed by a metal and topological surface states. By employing state of the art SQUID magnetometry, conductance spectroscopy and electrical transport together with thorough structural characterization, I examined the possible sources of such excitations in single crystals of SnTe and its alloys. The zero-energy states vanish in topologically trivial phase, while magnetic doping in the TCI phase enhances the signal at zero bias. Simultaneously, these states diminished with the applied external magnetic field. Surprisingly, gapless boundary states are not the only topologically non-trivial states hosted at the surface of TCI. It was recently experimentally found that crystal surface imperfections like naturally occurring atomic terraces give rise to unusual kind of 1D topological states on the TCI surface. Different scenarios, taking the 1D states into account are discussed in terms of possible sources of the observed superconducting point contact phenomenology.

Streszczenie

Niniejsza rozprawa doktorska jest poświęcona eksperymentalnym badaniom topologicznych izolatorów krystalicznych. Topologiczne izolatory krystaliczne stanowią oddzielną klasę materiałów topologicznych w których symetria zwierciadlana prowadzi do powstania metalicznych stanów na powierzchni kryształów. W szczególności, praca poświęcona jest badaniom materiałów opartych na tellurku cyny (SnTe), silnie zdegenerowanemu półprzewodnikowi o wąskiej przerwie energetycznej, w którym obserwowany jest stan topologicznego izolatora krystalicznego. Jednym z powodów dla którego materiały topologiczne są w ostatnim czasie intensywnie badane, jest możliwość uzyskania w nich topologicznego nadprzewodnictwa (na przykład w heterostrukturach nadprzewodnik/izolator topologiczny). Topologiczne nadprzewodnictwo charakteryzuje się istnieniem nieabelowych wzbudzeń, atrakcyjnych z punktu widzenia obliczeń kwantowych. W ostatnim czasie, pojawiły się również niespodziewane doniesienia, dotyczące kontaktów punktowych pomiędzy metalem a materiałem topologicznym. Okazało się, że takie złącze wykazuje charakterystykę obserwowaną dla nadprzewodzących kontaktów punktowych. Część z tych doniesień sugeruje, że zaobserwowano również wzrost przewodnictwa różniczkowego w okolicach zerowego napięcia. Ponieważ wzrost przewodnictwa różniczkowego jest często wiązanyz fazą topologicznego nadprzewodnika, uznano, że na międzywierzchni pomiędzy metalem a materiałem topologicznym zostaje wyindukowany stan nadprzewodzący z niekonwencjonalnym parametrem porządku. Stosując metody magnetometrii, spektroskopii przewodnictwa oraz charakteryzacji strukturalnej, podjęto próbę znalezienia źródła obserwowanych anomalii w monokryształach SnTe oraz powiązanych stopach. W trakcie tych poszukiwań wykazano, że charakterystyki typowe dla nadprzewodzących kontaktów punktowych nie pojawiają się w bogatych w ołów kryształów (Pb,Sn)Te - charakteryzujących się trywialną strukturą pasmową.

Domieszkowanie jonami magnetycznymi nie wpłynęło w sposób jakościowy na wyniki spektroskopii przewodnictwa, zaobserwowano jednak zachowanie krytyczne w funkcji pola magnetycznego i temperatury w fazie ferro-, para- i diamagnetycznej. Po raz pierwszy w kontekście obserwowanych anomalii przewodnictwa różniczkowego, zbadano i przedyskutowano rolę nadprzewodzących wytrąceń, dyslokacji oraz międzywierzchni metal/materiał topologiczny. Na podstawie przeprowadzonych badań stwierdzono, że obserwowane anomalie przewodnictwa różniczkowego, nie wykazują cech charakterystycznych dla układów dwu- i trójwymiarowych. W końcowej części rozprawy przedyskutowano również rolę jednowymiarowych topologicznie nietrywialnych stanów zaobserwowanych na stopniach atomowych w kryształach topologicznych izolatorów krystalicznych oraz omówiono dotychczasowe modele teoretyczne opisujące możliwe źródła anomalii w przewodnictwie różniczkowym.

Acknowledgements

I'm grateful to Dr Krzysztof Dybko for the entire guidance during my graduate studies. He helped me understand physics of topological materials and the art of experimental physics in general. It was a real privilege to work under such a mentor, thanks Krzysiek!

I'm indebted to Prof. Maciej Sawicki who helped me transition to condensed matter physics, learned to critically look at any experimental result and especially made me really skilled with making and interpreting magnetization measurements.

I admire help of Prof. dr. hab. Tomasz Dietl in guiding me throughout my graduate course and for providing virtually everything necessary to accomplish experimental and theoretical tasks I had to overcome during my PhD.

I'm grateful to Prof. Tomasz Story for many discussions on IV-VI semiconductors and for sharing his laboratory and sample resources.

The state of the art IV-VI crystals were prepared by Dr hab. Andrzej Szczerbakow and Msc. Eng. Jędrzej Korczak. Without such a great material doing any of this work would be impossible.

I'm indebted to to Prof. Sawomir Kret for the transmission electron microscope measurements.

I'm grateful to Mrs. Elzbieta Lusakowska for the AFM measurements and help with the crystal orientation.

I'm also indebted to Dr Jaroslaw Domagala for XRD characterization of measured crystals.

I'm grateful to Dr Maciej Zgirski and Dr Marek Foltyn for all the time they spent on helping me improving my laboratory skills.

I would also like to express my gratitude to Dr. Timo Hyart for all the scientific discussions which helped me better understand my experimental work.

Contents

List of Figures

List of Tables

For my loving wife and son.

Chapter 1

Topological Materials

1.1 Introduction and motivation

Zero-energy modes, signalizing the presence of topologically protected Majorana-type quasiparticles, were predicted to emerge at one-dimensional (1D) junctions of unconventional superconductors and topologically trivial systems, i.e., at the terminations of relevant 1D quantum wires [1] or at boundaries, such as vortices, of 2D counterparts [2]. A class of systems was then identified, in which differential conductance $\mathrm{d}I/\mathrm{d}V$ reveals signatures of Majorana bound states (MBSs) in the form of a symmetric zero-bias conductance peak (ZBCP) appearing in the specific range of magnetic fields. Such a spectrum was observed in semiconductor nanowires coupled with *s*-type superconductors, in which the Rashba spin-orbit coupling and a Zeeman splitting lead to a MBS localized at the wire ends. The excellent review was written by Alicea [3], the recent experimental progress in the Majorana nanowires is reviewed by Lutchyn and coworkers [4]. These studies culminated recently by the observation of the robust quantized value of the ZBCP in differential conductance of epitaxially grown Al/InSb nanowires [5], as theoretically expected for MBSs and, together with a related work for Al/InAs [6], illustrate interplay of topological and non-topological effects in differential conductance spectra of proximitized Rashba nanowires. Another relevant platform constitutes chains of magnetic atoms, as Fe, deposited on a superconductor, as Pb, whose mid-gap states can be probed by scanning tunneling microscopy [7].

Other examples are the layered triplet superconductor Sr_2RuO_4, where a broad ZBCP was detected at the side edges [8], and Bi_2Te_3 deposited on superconducting $NbSe_2$, in which signatures of MBS were found around vortices [9].

Generally speaking, there are two ways of realizing superconductivity in topologically non-trivial systems. One is to put topological material in proximity with an ordinary, s-wave superconductor, as proposed by Fu and Kane [2]. This approach might be technically very complicated and the success will mainly depend on the quality of the interface between TI and the superconductor. Alternatively one can look for a topological material which will be intrinsically superconducting. The most prominent member of this family is Cu intercalated Bi_2Se_3. Its topological surface showed only a Giaever gap spectrum according to scanning tunneling spectroscopy [10], a finding consistent with photoemission data for Bi_2Se_3 | $NbSe_2$ [11]. In contrast, soft point-contact spectroscopy studies of $Cu_xBi_2Se_3$ did reveal a ZBCP [12] but, at the same time, indicated a sensitivity of the outcome to mechanical stress [13]. Finally $Cu_xBi_2Se_3$ have been confirmed as unconventional superconductor by nuclear magnetic resonance [14] and specific heat measurements [15].

In the context of this thesis particularly relevant are characteristics of metal | semiconductor junctions collected earlier for IV-VI semiconductor compounds. In the case of superconducting $Pb_{1-x}Tl_xTe$, a conventional Giaever spectrum was observed using soft point-contacts [16]. In contrast, the same experimental approach points to the presence of ZBCP in the superconducting gap of $Sn_{1-x}In_xTe$, whose character and magnitude suggests the presence of Andreev bound states in the regime of low In concentrations resulting in $T_c \lesssim 1.2\,\mathrm{K}$ (ref. [16, 17]), whereas conventional Andreev reflection was found for higher In densities [17, 18].

All the systems described above are expected to exhibit some superconducting features. They are either doped TIs or strongly-spin orbital materials put into proximity with a superconductor. A true surprise came when a point-contact spectroscopy was performed on a topological material surface. These experiments revealed that junctions between normal metals and topological material are resembling characteristics of superconducting point contacts. Additionally, several reports claim to observe zero-bias conductance peak (ZBCP) which is an spectroscopic feature inherent to unconventional superconductors. Series of experiments involving hard point-contacts have shown ZBCP imposed on a gap, whose decay with the magnetic field and temperature could be described in a way specific to superconductors, i.e., by the BCS-like critical formulae [19–23]. For instance, in polycrystalline $Pb_{0.6}Sn_{0.4}Te$ ZBCP signatures persist up to T_c of 5.5 K but the shape and characteristics of the spectra depend strongly on the metal used for the tip[19].

Tip-induced ZBCPs, not accompanied by bulk superconductivity, were also detected in topological semimetals Cd_3As_2 (ref. [20, 21]) and TaAs (ref. [22, 23]) with T_c up to 7 K which, however, were not found by soft-point contact spectroscopy [21]. These findings have, therefore, been interpreted in terms of a local superconductivity induced mechanically by the tip. Another case is represented by exfoliated and patterned topological $Bi_{1.33}Sb_{0.67}Se_3$ nanoflakes with evaporated metal contacts, in which a logarithmic decay of ZBCP with temperature, and its complex dependence on the magnetic field and gate voltage were assigned to the Kondo effect [24]. A series of very recent experiments on tungsten carbide (WC), $MoTe_2$ and WTe_2 also report features characteristic for superconducting point contacts. All the relevant experiments reported to date are gathered in a table below together with a critical temperature T_C at which superconducting behavior vanishes.

Material	Type	T_C (K)	Year
Bi_2Se_3 [24]	TI	1.8	2016
$Pb_{0.60}Sn_{0.40}Te$ [19]	TCI	6.5	2016
Cd_3As_2 [20, 21]	Dirac Semimetal	13	2016
TaAs [22, 23]	Weyl Semimetal	7	2017
$MoTe_2$ [25]	Dirac Semimetal	5	2018
WC [26, 27]	Nodal line Semimetal	12	2018
ZrSiS[28]	Nodal line Semimetal	7	2018
WTe_2[29]	Weyl Semimetal	6	2019

TABLE 1.1: A collection of topological materials where superconducting point contacts were observed.

Although it is very interesting why such exotic features like zero-bias conductance peaks appear in the point-contact spectroscopy, the first question is, why we observe features characteristic for a superconductors between two metals in a normal state? These observations are surprisingly robust among many classes of topological materials, in many different samples coming from independent sources (Table 1.1). All of the collected evidence suggest we may deal with a new phenomenon specific to topological matter. However, besides of topologically non-trivial band structure, all the compounds share another property which was, surprisingly, overlooked by the community, namely at least one of the topological material constituents is a superconductor. This in turn indicates, that the observed superconducting phenomenology may be caused by superconducting nanoinclusions.

Research presented in this thesis is devoted to check possible trivial mechanisms and search for the superconductivity in the samples of IV-VI semiconductors. The topological phase diagram of a IV-VI based topological crystalline insulators is one of the best experimentally surveyed among topological materials, in general. The role of topologically non-trivial states in the system may reveal their impact of the superconducting behavior of a point contact. Detailed structural, magnetic and transport characterization is performed and trivial mechanisms resulting in superconductivity are carefully discussed. Finally, I will discuss possible scenarios which can explain or, at least, point to a new direction in understanding physical mechanism behind observed phenomena.

1.2 Topological Insulators

1.2.1 Hall Effect

To discuss a role of a non-trivial band topology in solids and its impact on the charge transport, I start with consideration of a flow of current in a simple 2D electron system. In the considered system, current flows from left to right through a bar shaped sample depicted on Fig 1.1.Two pairs of separate probes measure voltage drop. Usually, the current flows in a diffusive way from left to right and voltmeter readings should not be distinguishable on each side of of the sample. However, in the presence of an external magnetic field B, perpendicular to the direction of current flow a Lorentz force $\boldsymbol{F} = q \cdot (\boldsymbol{E} + \boldsymbol{B} \times \boldsymbol{v})$ will start deflecting path of the charge carriers. This leads to a charge accumulation on the sample edges, and thus creates additional electric field $\boldsymbol{E}_\mathbf{y}$ in the y direction of the plane to balance Lorentz force. Appearance of the voltage difference between top and bottom edges of the sample is known as a Hall effect after Edwin Hall who discovered it in 1879. Nowadays Hall effect serves as an important tool for estimating carrier concentration in conducting materials or for sensing magnetic fields.

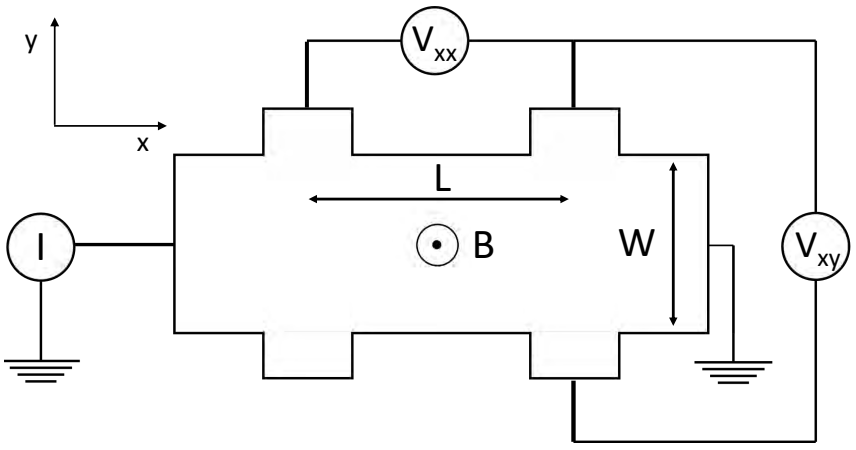

FIGURE 1.1: The Hall bar.

To estimate V_{xx} and V_{xy} and corresponding resistances, let us consider a classical particle moving in the electric $\boldsymbol{E}$ and magnetic fields $\boldsymbol{B}$ with velocity $\boldsymbol{v}$. The equation of motion can be written as:

$$m\frac{d\boldsymbol{v}}{dt} = -e\boldsymbol{E} - e\boldsymbol{v} \times \boldsymbol{B} - \frac{m\boldsymbol{v}}{\tau} \tag{1.1}$$

Where τ is an momentum relaxation time and describes average time between the collisions, assuming electrons are behaving as classical particles. e and m is the electron charge and mass respectively. This equation was first proposed and solved by Paul Drude and consequently referred to as *Drude model*.

From the stationary solution $\frac{dv}{dt}$=0 we can evaluate the velocity:

$$\boldsymbol{v} = -\frac{e\tau}{m}\boldsymbol{E} \tag{1.2}$$

We can also define carrier mobility as:

$$\mu = \frac{e\tau}{m} \tag{1.3}$$

This quantity characterizes how quickly a carrier can move through a conducting medium under an applied electric field. Very often mobility value is used to characterize crystal quality. Best and cleanest semiconducting AlGaAs/GaAs quantum wells can reach values as high as $35 \cdot 10^6\ cm^2\ V^{-1}\ s^{-1}$ [30, 31], whereas for strongly degenerate semiconductors like SnTe its of the order of 100 $cm^2\ V^{-1}\ s^{-1}$ as it will be shown in this thesis. The relation between the velocity and current density is given by:

$$\boldsymbol{J} = -ne\boldsymbol{v}. \tag{1.4}$$

Where n is carrier density. When we plug the expression 1.2 to the above equation, we arrive at the Ohm's law:

$$\boldsymbol{J} = \frac{ne^2\tau}{m}\boldsymbol{E}. \tag{1.5}$$

This simple law tells us how the current flows in response to an electric field. Proportionality constant is called conductivity σ and it's defined as:

$$\sigma = \frac{ne^2\tau}{m}. \tag{1.6}$$

In the presence of magnetic field this proportionality constant is not a single number, but a tensor in a following form:

$$\sigma = \begin{bmatrix} \sigma^{xx} & \sigma^{xy} \\ \sigma^{yx} & \sigma^{yy} \end{bmatrix}, \tag{1.7}$$

Equation 1.4 can also be written in a matrix notation

$$\sigma = \begin{bmatrix} 1 & \omega_C\tau \\ -\omega_C\tau & 1 \end{bmatrix} \boldsymbol{J} = \frac{ne^2\tau}{m}\boldsymbol{E}, \tag{1.8}$$

where $\omega_C = eB/m$ is a cyclotron frequency. Naturally it is connected with the resistivity tensor by a the identity $\rho\sigma$=1. So it's quite straightforward to simply write the resistivity tensor:

$$\rho = \sigma^{-1} = \begin{bmatrix} \rho^{xx} & \rho^{xy} \\ \rho^{yx} & \rho^{yy} \end{bmatrix}. \tag{1.9}$$

In terms of real experiment, one usually obtains *resistance* R through the measurement of a voltage drop. Resistance is related to the resistivity by geometrical factor. The nice property of ρ_{xy} is that there is no geometrical factor and so R_{xy} equals exactly to ρ_{xy}. If the Hall bar depicted in the Fig 1.1 has a width of W, and we let the current flow in the x direction we will obtain following form for R_{xy}:

$$R_{xy} = \frac{V_y}{I_x} = \frac{WE_y}{WJ_x} = \frac{E_y}{J_x} = \rho_{xy}. \tag{1.10}$$

Now we can define the Hall coefficient which relates current flowing in the x direction I_x and the corresponding electric field E_y in the y direction:

$$R_H = -\frac{E_y}{J_x B} = \frac{\rho_{xy}}{B}. \tag{1.11}$$

Which in terms of the Drude model can be expressed as:

$$R_H = \frac{V_H d}{IB} = \frac{1}{ne}. \tag{1.12}$$

So finally we can write down expressions for transversal and longitudinal resistances we're going to measure on the Hall bar device:

$$\rho_{xx} = \frac{V_{xx}}{I} = \frac{m}{ne^2\tau}, \qquad \rho_{xy} = \frac{V_{xy}}{I} = \frac{B}{ne}. \tag{1.13}$$

1.2.2 Quantum Hall Effect

This is not the entire story. If we keep increasing the magnetic field or obtain a sample with small n, the electrons will start to move in a cyclotron orbits. Provided that the system is so clean that the scattering events will not break the phase of charge carriers, the bulk of a sample will become insulating.

However, the electrons which are close enough to the edge of a Hall bar will start to bounce from the left to right. For the opposite edge, the electrons will skip in the opposite direction (Fig 1.2). This phenomenon is called chiral edge transport, and was first experimentally seen in a silicon based metal-oxide-semiconductor field effect transistor (MOSFET) and its called the Quantum Hall effect (QHE). Results of this experiment is depicted in the Fig 1.3. Let us briefly examine what happens in a QHE state. The starting point here is Hamiltonian of an electron moving in external magnetic field.

$$H = \frac{1}{2m}(\boldsymbol{p} + e\boldsymbol{A}) \tag{1.14}$$

Our electron is restricted to move in a 2 dimensional plane (x,y), and magnetic field is set constant and perpendicular to this plane meaning, $\nabla \times \boldsymbol{A} = B\hat{\boldsymbol{z}}$. This is not a unique choice by any means, however the resulting physical picture is gauge-invariant. The eigenproblem now reads:

$$H\psi(x,y) = \left[\frac{p_x^2}{2m} + \frac{1}{2m}(p_y - eBx)^2\right]\psi(\boldsymbol{r}) = E\psi(\boldsymbol{x},\boldsymbol{y}). \tag{1.15}$$

As momentum p_y is transnationally invariant and commutates with Hamiltonian , it's appealing to use separation of variables ansatz e.g. $\psi_k(x,y) = e^{iky} f_k(x)$. By acting with this wave function on the above Hamiltonian, we arrive at:

$$H = \frac{p_x^2}{2m} + \frac{1}{2}m\omega_c(x - x_0)^2, \tag{1.16}$$

where $x_0 = \hbar k_y / m\omega_c$ in analogy to classical harmonic oscillator we can define a characteristic length

$$l_B = \sqrt{\frac{\hbar}{eB}}. \tag{1.17}$$

l_B is called a magnetic length and determines the size of cyclotron orbit. For example, $l_B \approx 26\,\text{nm}$ at 1 T . Knowing the explicit solution of the problem is the harmonic oscillator, we can write the expression for eigenenergies:

$$E_n = \hbar\omega_c\left(n + \frac{1}{2}\right). \tag{1.18}$$

Typically for the harmonic oscillators, the energy spectrum consists of levels, in this case separated by $\hbar\omega_c$. These are commonly know as *Landau levels*. The Landau levels are highly degenerate, as the energy does not depend on k_y.

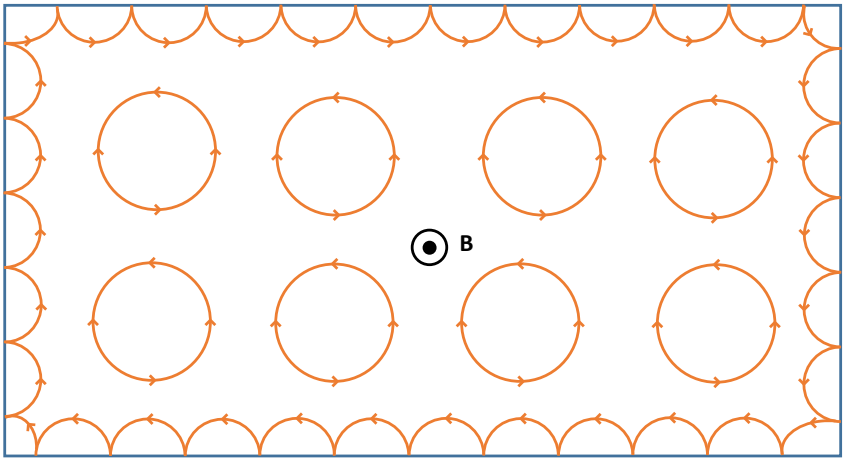

FIGURE 1.2: Schematic illustration of sample in the QHE state. Electrons inside the bulk are moving in cyclotron orbits making bulk insulating, while current flows along the edge of a sample.

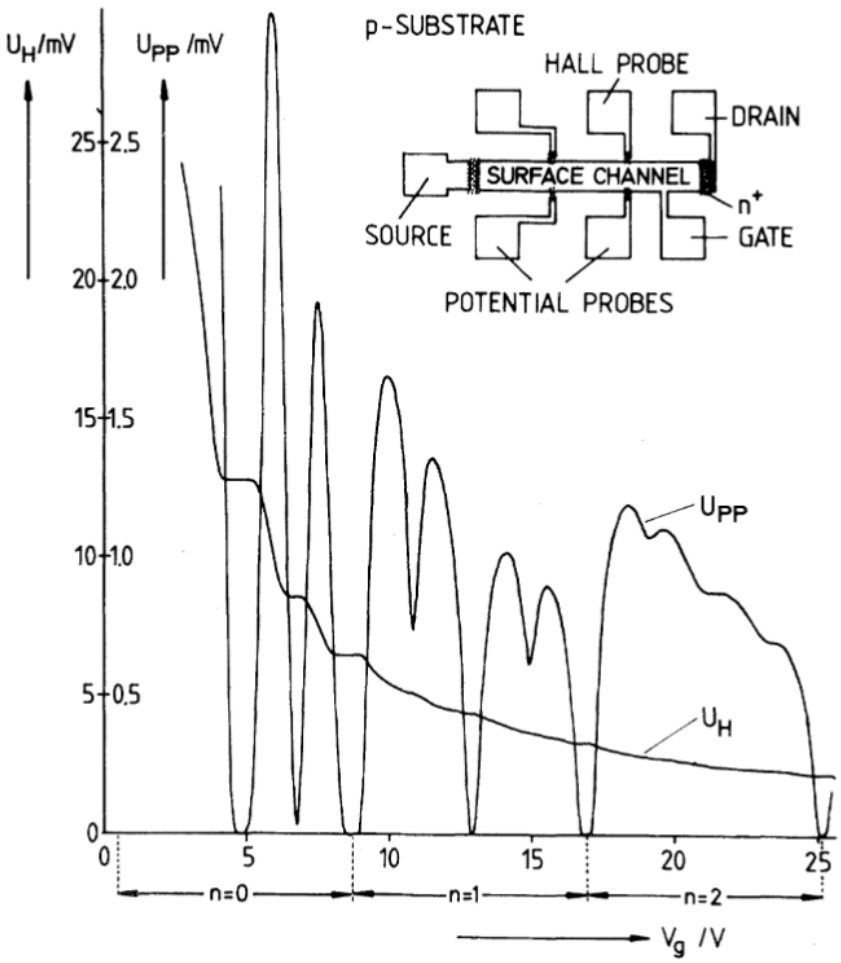

FIGURE 1.3: Discovery of Hall conductance quantization. After: [32]

For a system with linear dimensions L_x and L_y and periodic boundary conditions, we find that k_y is quantized:

$$k_y = \frac{2\pi}{L_y} m_y,\ m_y \in \mathbb{Z}, \tag{1.19}$$

Where $\mathbb{Z}$ defines a set of all integers. A more careful treatment is required for L_x. Note, that wavefunctions are exponentially localized around $x_0 = -kl_B^2$ so we would expect the allowed k values to be in range $-L_x/l_B^2 \geq k \geq 0$. The number of states at the Landau level is equal to:

$$N_L = \frac{L_y}{2\pi} \int_{-L_x/l_B^2}^{0} dk = \frac{eBL_xL_y}{2\pi\hbar} \tag{1.20}$$

The degeneracy at the Landau level increases with magnetic field, as well as the separation between neighboring states. When magnetic field is high enough, so $\hbar\omega_c >> k_B T$ (Quantum Hall regime) the degeneracy gets so high that the electrons are fully filling only a few lowest Landau levels. Such electron ordering has striking and remarkable consequences. Under change of carrier density or magnetic field Hall conductance forms a sequence of quantized plateux in the units $\sigma_{xy} = e^2/h$. Consequently due to the insulating bulk as shown in the Fig 1.3 the conducitivity σ_{xx}=0. We can understand it by tracing the position of the *Fermi level* E_F. If E_F intersects a Landau Level, we see a finite bulk conductivity. However, when E_F resides between two neighbouring Landau levels with indicies n and $n+1$ the bulk is insulating and so σ_{xx}=0. This effect was first observed in Bismuth single crystal by Lev Schubnikov and Wander Johannes de Haas [33] and subsequently called Schubnikov-de Haas oscillations. However, Landau Levels alone cannot explain exactly quantized QHE plateux.

In 1982 Thouless, Kohomoto, Nightingale and den Nijs (TKKN) recognized that QHE is not only quantum mechanical but also topological [34]. To understand the conductance qunatization it is necessary to introduce concept of a Berry phase. The Berry phase plays an essential role not only in the physics of topological insulators, but in many different fields of physics. The derivation goes along the line presented in Ref. [35]. Let $\boldsymbol{R}$(t) be a time-dependent set of parameters spanning a vector space. The n-th egienstate is denoted as $|n, \boldsymbol{R}(t)\rangle$. Shroedinger equation for such eigenproblem reads:

$$H(\boldsymbol{R}(t))\,|n, \boldsymbol{R}(t)\rangle = E_n[\boldsymbol{R}(t)]\,|n, \boldsymbol{R}(t)\rangle \tag{1.21}$$

If we assume adiabatic time evolution of $\boldsymbol{R}$ starting at t=0 and $\boldsymbol{R}_0$ we can write time-dependent Schroedinger equation for this state, in somewhat standard way:

$$H[\boldsymbol{R}(t)]\,|n,t\rangle = i\hbar\frac{\partial}{\partial t}\,|n,t\rangle \tag{1.22}$$

The n-th eigenstate at time t is given by:

$$|n,t\rangle = \exp\left(\frac{i}{\hbar}\int_0^t dt^{'} L_n[\boldsymbol{R}(t^{'}])\right)|n,\boldsymbol{R}(t)\rangle\,, \tag{1.23}$$

where

$$L_n[\boldsymbol{R}(t^{'})] = i\hbar\dot{\boldsymbol{R}}(t^{'})\cdot\left\langle n,\boldsymbol{R}(t^{'})\right|\nabla_R\left|n,\boldsymbol{R}(t^{'})\right\rangle - E_n[\boldsymbol{R}(t^{'})]. \tag{1.24}$$

We can factorize this time dependent state to the form of:

$$|n,t\rangle = \exp\left(-\int_0^t dt^{'}\dot{\boldsymbol{R}}(t^{'})\cdot\left\langle n,\boldsymbol{R}(t^{'})\right|\nabla_R\left|n,\boldsymbol{R}(t^{'})\right\rangle\right)|n,\boldsymbol{R}(t)\rangle\times\exp\left(\int_0^t dt^{'}E_n[\boldsymbol{R}(t^{'})]\right) \tag{1.25}$$

The first exponential term is the non-trivial quantum-mechanical phase accumulated during the time evolution. The second term is completely trivial, dynamical phase present for any eigenstate, even if the parameters don't change. If $\boldsymbol{R}$ moves on a closed loop C and returns from its original value at $t = 0$ at time $t = T$. The *Berry phase*, γ_n[C] is defined as:

$$\gamma_n[C] \equiv \int_0^T dt\dot{\boldsymbol{R}}(t)\cdot i\,\langle n,\boldsymbol{R}(t)|\,\nabla_R\,|n,\boldsymbol{R}(t)\rangle = \oint_C d\boldsymbol{R}\cdot i\,\langle n,\boldsymbol{R}(t)|\,\nabla_R\,|n,\boldsymbol{R}(t)\rangle \tag{1.26}$$

This brings us to the definition of a Berry connection, which is an analogue of a vector potential for magnetic field:

$$\boldsymbol{A}_n = -i\,\langle n,\boldsymbol{R}(t)|\,\nabla_R\,|n,\boldsymbol{R}(t)\rangle \tag{1.27}$$

The curl operator of Berry connection is known as Berry curvature

$$\boldsymbol{B}_n = \nabla_R\times\boldsymbol{A}_n(\boldsymbol{R}) \tag{1.28}$$

The two are related by the Stokes' theorem:

$$\oint_C d\boldsymbol{R}\cdot\boldsymbol{A}_n(\boldsymbol{R}) = -\int_S d\boldsymbol{S}\cdot\boldsymbol{B}(\boldsymbol{R}) \tag{1.29}$$

A seminal idea of TKNN was noticing the connection between Berry phase

and quantized Hall plateux. If we sum over all available Bloch states $|\mu_m(\boldsymbol{k})\rangle$ and integrate the Berry curvature over the Brillouin zone, we find TKNN invariant:

$$\nu = \sum_{m=1}^{N} \frac{1}{2\pi} \int_{BZ} \nabla \times i \langle \mu_m(\boldsymbol{k}) | \nabla | \mu_m(\boldsymbol{k}) \rangle \, d^2\boldsymbol{k} \tag{1.30}$$

$$= \sum_{m=1}^{N} \frac{1}{2\pi} \int_{BZ} F_m d^2\boldsymbol{k} = -\frac{1}{2\pi} \gamma_n[\partial \mathrm{BZ}] \tag{1.31}$$

As ν is restricted to be an multiple of 2π. This is essentially equivalent to:

$$\gamma_n[\partial \mathrm{BZ}] = 2\pi m, m \in \mathbb{Z} \tag{1.32}$$

So in other words, change of phase of the wave function after encircling closed loop over the Brillouin zone boundary necessarily needs to be an single-valued multiple of 2π. That is why σ_{xy} is quantized to integer multiples of e^2/h. The discovery of Quantum Hall Effect reshaped the way we understand physics of electrons in solids and in fact its the first discovered topological phase of matter.

1.2.3 Topological Insulators

Another groundbreaking discovery came in 2004 when Andre Geim and Konstatin Novoselov report successful exfoliation of single graphite flakes – the graphene [36]. Among plenty fascinating properties like room-temperature quantum Hall effect [37] or extraordinary mechanical stability and flexibility, it was predicted that graphene can host new topological quantum state [38] called quantum spin Hall effect(QSHE). It assumes existence of two copies of chiral, counter propagating edge states. A key to understanding this is spin-orbit coupling. If electrons move through the crystal, it experiences electric field coming from the lattice. If we recall Lorentz transformation for a particle moving in 3D space, we can naively deduce impact of the crystalline lattice electric field on electron motion:

$$E'_x = E_x, \quad E'_y = \frac{E_y - vB_z}{\sqrt{1-v^2}}, \quad E'_z = \frac{E_z + vB_y}{\sqrt{1-v^2}}, \tag{1.33}$$

$$B'_x = B_x, \quad B'_y = \frac{B_y + vE_z}{\sqrt{1-v^2}}, \quad B'_z = \frac{B_z - vE_y}{\sqrt{1-v^2}}. \tag{1.34}$$

Electrons moving perpendicularly to an electric field, will experience magnetic field component in their rest frames. This magnetic field couples to their

spins and consequently Zeeman splits two spin directions proportionally to the momentum. Changing momentum and spin simultaneously results in the same energy value, which means this interaction is time-reversal invariant. This has very important consequence for the band structure symmetries. According to Kramers thorem, each Bloch eigenstate at wave vector $\boldsymbol{k}$ has a degenerate, time-reversed partner. Fig 1.4 illustrates that the band structure is mirror symmetric about zero momentum with respect to the spin. At the Brillouin zone edges and $\boldsymbol{k}$=0 time reversed states have the same momentum.This type of points of reciprocal space are called time-reversal invariant momenta (TRIM). For the system with high spin-oribt coupling, these states will become spin non-degenerate. As seen in the Fig 1.4 spin-orbit-split states can recombine again crossing the Fermi level in two fundamentally different ways. Fermi level can either intersect even (Fig 1.4a) or an odd (Fig 1.4b) number of Kramers pairs. For the latter case, the Kramers pairs in the surface states "switch partners", and as a result, the surface state is guaranteed to cross any energy inside the bulk gap, whereas in the first case we can smoothly decompose our system into atomic insulator. These two possibilities define how we can classify hamiltonians, and lead to so called $\mathbb{Z}_2$ topological invariant [38, 39]. Accordingly corresponding topological invariant ν is defined as the number of Kramers pairs in the bulk energy gap modulo 2.

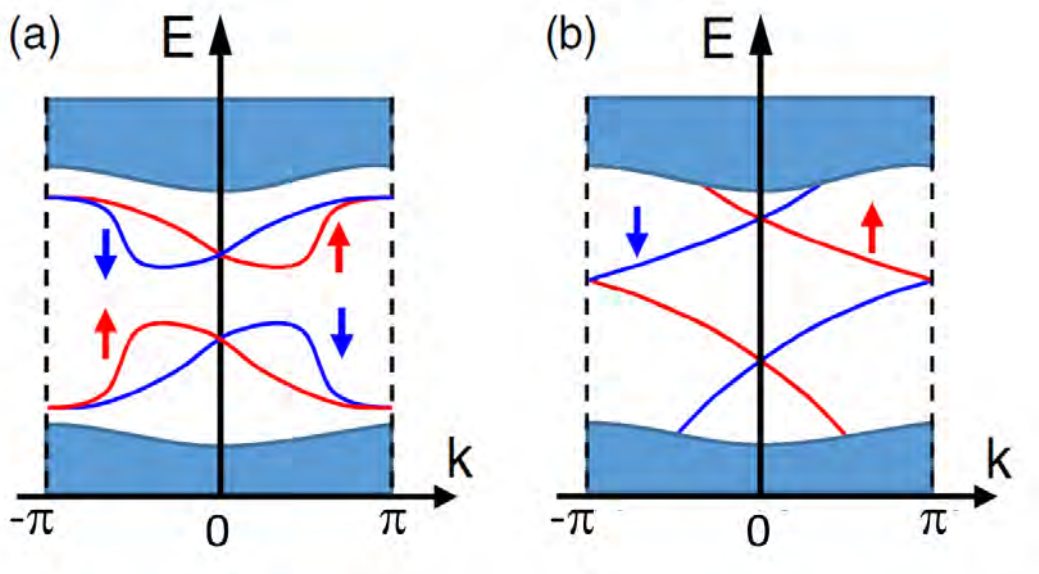

FIGURE 1.4: Illustrations of the Kramers pairs of bands (a) for topologically trivial and (b) non-trivial cases. Adapted from [35].

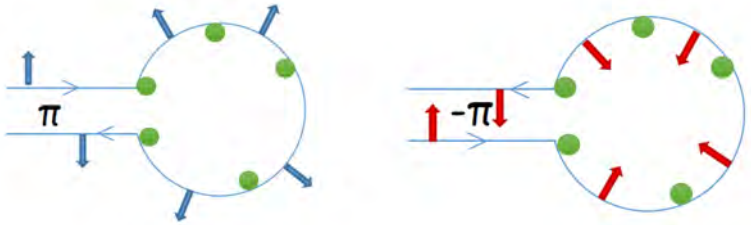

FIGURE 1.5: Forbidden backscattering in a topological insulator. Due to geometric phase of π two backscattering path destructively interfere.

Quantum Spin Hall Effect The first experimental realization of $\mathbb{Z}_2$ topological order is the Quantum Spin Hall effect. Atlernatively, the same phenomenon is called the 2D topological insulator. The effect essentially consists of a two, time reversed copies of Quantum Hall effect (Fig 1.2). This results in a helical transport along the sample edges. Both in QHE and QSHE edge states are topologically protected. In the Hall bar geometry the two probe conductance for the QSHE always assumes values of $2e^2/h$ due to right and left moving states, whereas for the QHE system the conduction is just a multiple of e^2/h.
It is instructive to discuss their robustness against disorder, as microscopically the picture is different. QHE is observed in big, macroscopic samples, and still yields remarkable quantization accuracy. There is virtually no available state to backscatter as bulk states are completely occupied. At the same time, bulk separates counter propagating edge modes on the opposite edges of a sample. In the Quantum spin Hall state there are two counter propagating edge states per sample edge, but the scattering is forbidden by very strong spin-orbit interaction which couples spin to pseudo-momentum. The only available scattering mechanism is a spin-rotation or spin-flip. The former is also forbidden because two different paths of propagation will always have a geometric phase of π and would destructively interfere as depicted in the Fig 1.5. Only magnetic impurity, which can break time-reversal symmetry can provide such a scattering channel.

The first experimental realization of 2D Topological Insulator As pointed out in the introductory paragraph, the gap opening is of the order of ten of microelectron volts, insufficient to realize a QSHE. Naturally, a system made entirely from carbon is not expected to have strong-spin orbit coupling. However, proposal by Kane and Mele initiated a theoretical quest for alternative materials. This quest was accomplished by Bernevig, Hughes and Zhang

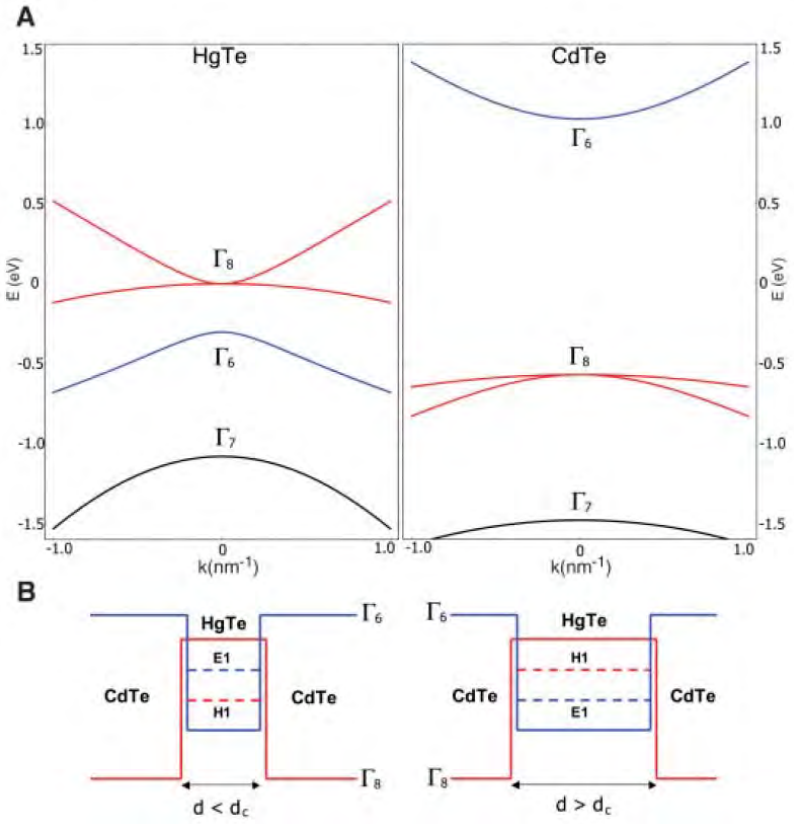

FIGURE 1.6: A theoretical proposal of realizing two dimensional Topological Insulator. Panel **a** depicts band structure of bulk HgTe (left) and CdTe (right). **b** Band diagram for Γ point in the quantum well. Right panel depcits topologically nontrivial band ordering for sufficiently thick wells. Left panel illustrates trivial band ordering for quantum wells thinner than d_c= 6.5 nm. Figure adapted from [40]

(BHZ) who in 2006 proposed CdTe/HgTe/CdTe quantum wells (QWs) as a convenient platform to realize Kane-Mele model [40].

Unusual properties of HgTe band structures were known to community since the middle of the sixties. Piotrzkowski et al. [41] were first to notice that spin-orbit splitted anion p-type orbitals are laying above cation s-type orbitals. In fact, the spin-orbit coupling is so strong, it inverts the sign of the semiconducting gap and changes the usual roles of two bands as seen in the Fig 1.6. In the case of CdTe situation is completely trivial and resemble band ordering of conventional semiconductors with Γ_6 and Γ_8 acting as a conduction and valence band respectively. Placing HgTe quantum well between CdTe layers will make the band gap smaller and for sufficiently thin QWs will restore conventional band ordering. However, there's a critical thickness $d_c \approx 6.5$ nm above which the bands will be inverted. This remarkable property of HgTe

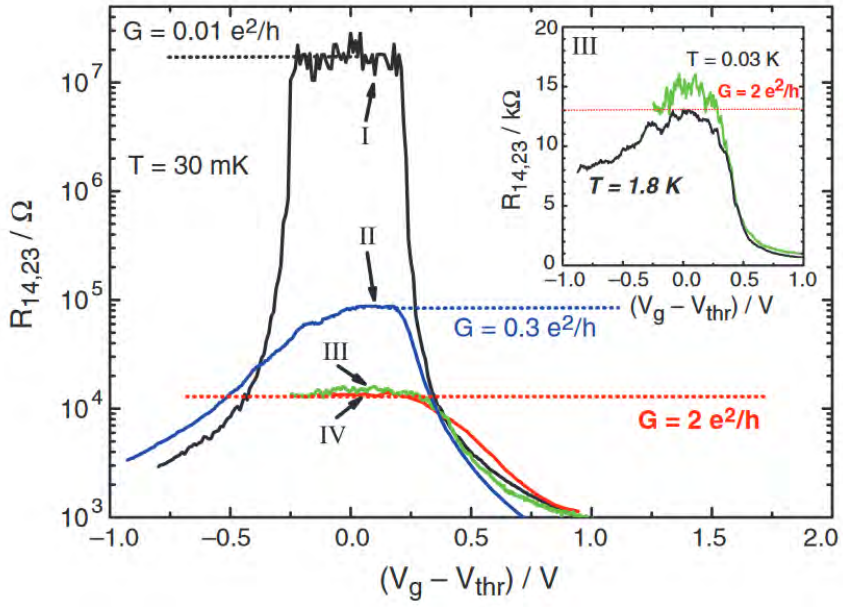

FIGURE 1.7: An experimental realization of the two dimensional Topological Insulator. Gate sweeps for four different devices, measured in a four terminal configurations are presented on the graph. Trace I was collected for 5.5 nm QW with 20 um distance between the leads. Traces II, III and IV were collected for 7.3 nm thick QW with 20, 1 and 0.5 um distance between the leads. Inset compares two temperatures for device III. Figure adapted from Ref. [42]

QWs provides a control parameter which allows for probing trivial and non-trivial band topologies. BHZ found that in the inverted gap regime, bands need to close and reopen to create edge states. After this seminal prediction group of L. Molenkamp [42] at the University of Wuerzburg, prepared HgTe QWs using molecular beam epitaxy. Figure 1.7 illustrates first observation of a 2 dimensional topological insulator. For a topologically trivial 5.5 nm-thick quantum well resembled an insulating character when Fermi level is tuned into the gap as shown in the Fig 1.7 (black line). A spectacular result confirming BHZ prediction was shown for thicker QWs (7.3 nm). Indeed litographically defined small Hall bars shown predicted conductance values of $2e^2/h$ when the Fermi level is placed in the gap. Unexpectedly, larger device with 20 μm channel length didn't fulfill theory expectation and was significantly less conductive as shown with the blue line in the Fig 1.7. Surprising lack of robust, large-scale quantization is not understood. The community looked for relevant scattering mechanisms which would break time reversal symmetry, like Kondo effect [43], charge puddles [44, 45], electrical noise [46] or charged impurities effectively acting as magnetic scatterers [47]. The clean

cut experimental evidence which could explain short channel length is yet to be discovered. Existence of edge states was further confirmed by H-bar geometry [48] suitable for non-local measurements and by scanning SQUID microscopy [49]. Subsequently InAs/GaSb quantum wells were predicted [50] and experimentally verified [51] to exhibit properties of 2D TI. For this material inverted band structure comes from an anticrossing of InAs and GaSb in the quantum well, and the resulting band gap is very small (5 meV). Some reports suggest that quantized resistance value, expected for quantum spin Hall insulator can arise in a trivial phase (Nichele et al.[52]). Within this picture, measured resistance accidentally fits expected value and can be observed for any system with trivial edge states. The newest development in this field was observed for monolayer of WTe_2 which is a Quantum Spin Hall insulator [53–55]. This offers very promising route for making easy-to-fabricate 2D TIs structures, without a necessity of complex MBE growth technology. Despite the ease of fabrication, the problem of short edge channels is persisting and for the WTe_2 edge channels are as short as few hundreds of nanometers, even though QSHE was observed up to 100 K in this material. Nevertheless, BHZ theoretical proposal, and beautiful experimental confirmation by Koenig et. al. [42] started a new field of condensed matter physics - topological materials.

1.2.4 3D Topological Insulators

Naturally, after successful confirmation of 2D TI phase, the community started considerations on the extension of the idea for three dimensions. For such a 3D TI, instead of topologically protected edge state states, we would have topologically protected two-dimensional electron gas (2DEG) spanning the entire surface of a sample. A 3D TI can be realized in two different ways. A first scenario, called a weak topological insulator is realized by stacking several layers of 2D TIs on each other. As a result surface state inherits the spin character of QSH insulator, yet, these states may not be protected against disorder [56]. A completely new phase of matter, so called *Strong Topological Insulators* arise for materials with odd number of band inversions (so non zero $\mathbb{Z}_2$ invariant). These types of materials have a helical, metallic surface state. This means, spin-momentum locking prevents backscattering around the Dirac cone, preserving time reversal symmetry similarly to the 2D case (see Fig 1.8).

The first realized 3D TI was a $Bi_{1-x}Sb_x$ alloy [57]. However, the model 3D TI

system is realized in Bismuth chalcogenides, Bi_2Te_3 and Bi_2Se_3. These materials were already widely studied before due to high thermoelectric performance. Odd number of band inversions at the Γ point of Brillouin zone, high spin-orbit coupling, and n-type conductivity makes them ideally suited for *angle-resolved photoemission spectroscopy* (ARPES). Moreover, large bulk band gap (300 meV) makes surface states robust even at room temperature. In one of many experiments done on this system group led by M.Z. Hasan shown linear dispersion of surface states in the vicinity of Γ point[58]. Subsequently, Hsieh et al. [59] shown spin-resolved ARPES measurements on Bi_2Te_3 and $Bi_{2-\delta}Ca_\delta Se_3$. The Ca doping was used to tune the Fermi energy in the band gap. These experiments confirmed spin-momentum locked electron transport around the Dirac cone, protected by time reversal symmetry.

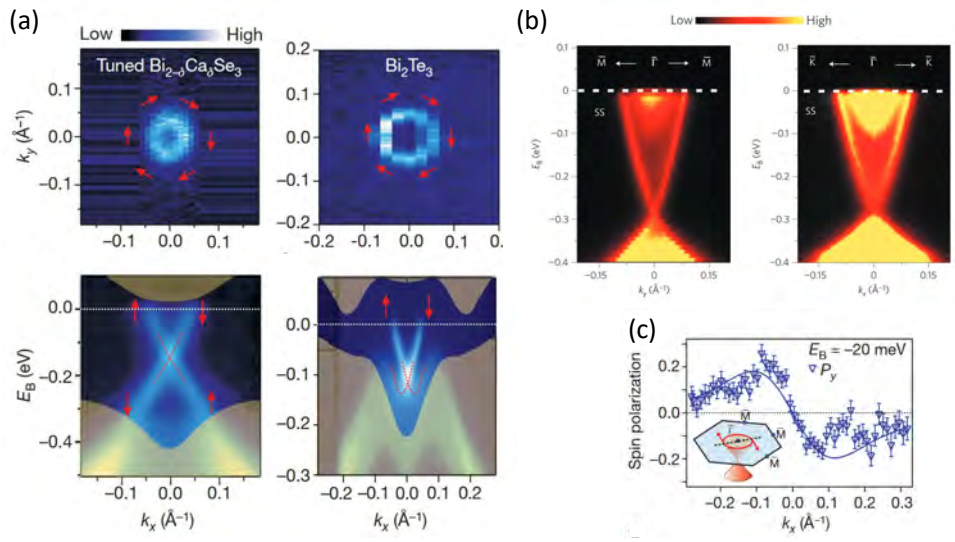

FIGURE 1.8: (a) Spin resolved ARPES measurements taken around Γ point on Bi_2Te_3 and $Bi_{2-\delta}Ca_\delta Se_3$ as presented in Hsieh et al. [59].(b) Energy dispersion of (111) surface in Bi_2Se_3.(c) Measurement of surface state y spin component along Γ - M [59]

1.2.5 Topological Crystalline Insulators

It turns out that HgTe quantum wells and 3D TIs are only the tip of an iceberg. Shortly afterwards people turned their attention from time-reversal symmetry protected systems to something completely new. In fact, there is an entire classification of topological phases based on the underlying symmetry which leads to non-trivial topology. A pedagogical review on this matter is given by Ando and Fu [60]. It was first proposed by Liang Fu in 2011 [61] to classify band insulators with respect to the point-group symmetry of the

parent crystals. This proposal coined the name Topological Crystalline Insulators (TCIs). A first member of this broad family is a crystal with mirror symmetry which defines topological protection by the mirror Chern number N_m [62].

The mirror symmetry is defined by the product of two-fold rotation C_2 and spatial inversion P. If we define mirror plane as x = 0, the mirror operator is given by:

$$M(x) = PC_2(x) \tag{1.35}$$

$$x \to -x, \;\; s_y \to -s_y, \;\; s_z \to -s_z \tag{1.36}$$

These two ingredients are necessary, as spin is a pseudo-vector and does not change sign under the inversion operation. For the particles with spin-$\frac{1}{2}$ a twofold rotation means rotation by 2π, so the electron wave function will pick up a minus sign. This satisfies the relation for a mirror operation $M^2 = -1$ and consequently leads to eigenvalues of $+i$ or $-i$ [60].

Naturally occurring crystals preserve mirror symmetry. For such a system, we can choose mirror invariant Bloch states $|\mu_m(\boldsymbol{k})\rangle$ as eigenstates of M. According to the reasoning presented in the above paragraph, this will lead to two sets of Bloch states $|\mu_{m,\pm i}(\boldsymbol{k})\rangle$, for two eigenvalues of the mirror operator $M(x)$. We can define a topological invariant $\nu_{\pm i}$ for each set of Bloch eigenstates. As pointed out in Ref. [60], the sum of these invariants is equivalent to TKNN topological invariant (Eq. 1.31) which determines conductance quantization in the Quantum Hall Effect. Difference of these invariants however, defines the Mirror chern number N_m [61], and for systems with $N_m \neq 0$ is a signature TCI phase.

1.2.6 Experimental realization of the TCI phase

The first material which was theoretically predicted to realize TCI phase is SnTe and its related alloys (Pb,Sn)Te [63] and (Pb,Sn)Se. Underlying mirror symmetry of these fcc rock-salt crystals, give rise to metallic surface states. The plane of two L points in [111] direction along with the Γ point forms space mirror plane in a momentum space about [110] axis (1.9(c)). This leads to a mirror Chern number of N_m=-2 [63] and consequently predicts formation

of two Dirac cones, arising from two spin-polarized surface states with opposite mirror eigenvalues. Each of the two mirror-symmetric lines X_1-Γ-X_1 and X_2-Γ-X_2, give rise to two Driac Cones, making a total of 4. Due to topological protection arising from mirror symmetry only surfaces with preserved mirror symmetry are expected to host topological surface states (TSS). Three surfaces fulfilling these conditions are (100), (110), (111). Tin Telluride crystal naturally grows in [100] direction forming (100) and (111) crystal facets. More detailed description of growth techniques will be given in the next chapter devoted to properties of IV-VI materials.

Experimentally, Dziawa et al. [64] revealed the presence of TSS in $Pb_{1-x}Sn_xSe$ single crystals, simultaneously indications of TSS were presented for SnTe [65]. A spin resolved ARPES measurements were subsequently reported for $Pb_{1-x}Sn_xTe$ [66] establishing IV-VI semiconductors as model TCI system. Figure 1.9(a) illustrates single Dirac cones structure expected for a 3D topological insulator. In stark contrast, the double Dirac cone in $Pb_{1-x}Sn_xTe$ around each of the X point, is seen in the Fig 1.9(b), as theoretically predicted. Use of ternary compounds was dictated by tremendously high carrier density in SnTe. $Pb_{0.77}Sn_{0.23}Se$ however, can be doped to achieve n-type conductivity thus populating midgap states. Additionally, in this system band inversion occurs as a function of temperature which gives unique opportunity of witnessing birth of topological surface states (Fig 1.10(b)). Later, ARPES measurements were performed for different composition at various temperatures making band structure of $Pb_{1-x}Sn_xSe$ one of the best understood among all topological materials [67].

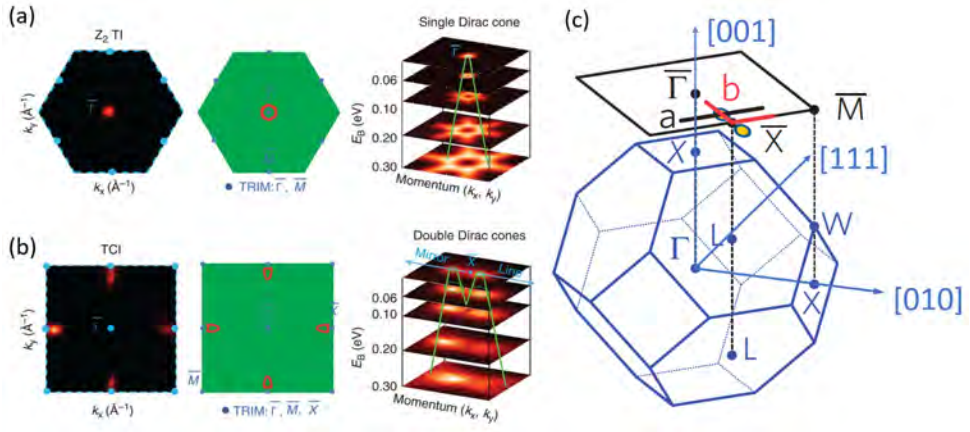

FIGURE 1.9: (a,b) Spin resolved ARPES measurements taken around Γ point on $Pb_{1-x}Sn_xTe$ as presented in Hsieh et al. [59].Brillouin zone of FFC IV-VI semiconductor. Adapted from Ref. [64].

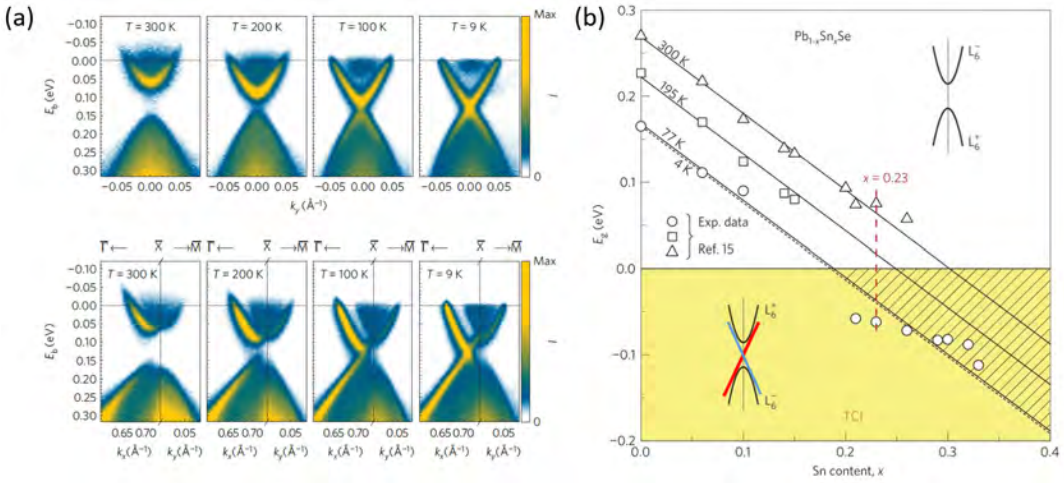

FIGURE 1.10: (a) Temperature dependence of a energy dispersion in the vicinity of $\bar{X}$. (b) Energy dispersion measured along the ($\bar{\Gamma}$-$\bar{X}$-$\bar{\Gamma}$) line in the Brillouin Zone. Spectra clearly show emerging Dirac-like bands below 100 K. Panel (b) illustrates composition dependence of the bandgap of $Pb_{1-x}Sn_xSe$ at various temperature. As reported by Dziawa et al. [64].

1.3 Transport experiments on Topological Crystalline Insulators

Since the Fermi level in SnTe lies deeply in the valence band, probing transport properties of topological surface states is difficult. Contrary to the bismuth chalcogenides based topological insulators these materials cannot be easily exfoliated. Achieving higher surface-to-bulk ratio is thus only possible by growing thin films and nanostructures. SnTe based thin films have been grown on a variety of substrates such as BaF_2 [68], Bi_2Te_3 [69], CdTe [70], $SrTiO_3$ [71],Si [72] and GaAs [73]. However, achieving high quality of these films proved to be really challenging as layers with nanometric thicknesses tend to be very rough, which leads to reduced carrier mobility. TCIs should exhibit particularly interesting transport properties compared to $\mathbb{Z}_2$ TIs. As a consequence of mirror symmetry, the number of occupied Dirac cones should strongly depend on the position of Fermi level (see Fig.1.11). In the center of the gap four Dirac cones exists at the surface of SnTe, however these four Dirac cones merge into two as Fermi level moves towards valence band. Two different transport phenomena can suggest existence of topological surface states in IV-VI semiconductors.

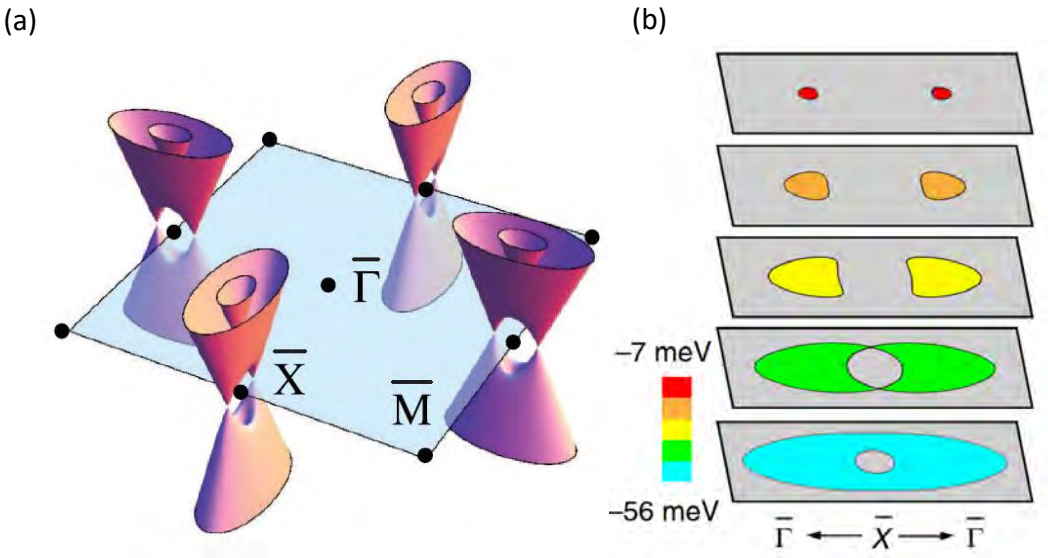

FIGURE 1.11: (a) Temperature dependence of a energy dispersion in the vicinity of $\bar{X}$. (b) Energy dispersion measured along the ($\bar{\Gamma}$-$\bar{X}$-$\bar{\Gamma}$) line in the Brillouin Zone. Spectra clearly show emerging Dirac-like bands below 100 K. Panel (b) illustrates composition dependence of the bandgap of $Pb_{1-x}Sn_xSe$ at various temperature. Panel (a) is adapted from the work of Okada et al. [74], panel (b) comes from the work by Hsieh et al. [63].

Weak antilocalization As mentioned in the introductory section, Dirac fermions present in TCIs have Berry phase of π. The same mechanism which is responsible for absence of backscattering presented in the Fig 1.5, is responsible for the *weak antilocalization* (WAL) effect. When electron travels along closed trajectory, it can move along, two, time-reversed paths. π Berry phase leads to the destructive interference, which reduces the probability of localizing electrons along that path. An opposite phenomenon called *Weak localization* (WL) happens when there is no π phase shift. The electron can travel along time reversed paths and interfere constructively. As the probability of finding electron travelling along these paths is enhanced, the ability of transferring charge is reduced. This leads to positive correction to the zero-field resistivity and leads to negative magnetoresistance upon application of magnetic field. Similarly a non-zero magnetic field will lead to positive magnetoresistance in the case of weak antilocalization. It is important to stress, weak antilocalization is not uniquely observed in topological materials or even material with the linear band dispersion. In fact, any thin metallic film with strong spin-orbit could exhibit the weak-antilocalization effect. This can happen due to Dresselhaus spin-orbit interaction for the systems without inversion center.

If Rashba split 2D bands exist at the surface of a topologically trivial material one will also observe WAL in magnetotransport measurements. This can happen if a depletion layer appears on the surface of a film, due to formation of a native oxide or for the case of non-symmetric quantum wells. Alternatively, crossover from WL to WAL is observed when light metal (e.g. Mg) is doped with high-spin orbital material (like Au). In that case, WAL is due to a phase change caused by spin rotation whenever an electron is scattered on such impurity. However, for a system like SnTe none of the abovementioned scenarios is plausible. First rocksalt structure of SnTe guarantees inversion center at each atom position. Formation of inversion layer can be easily avoided by capping sample with an insulating material. That is why WAL observed in SnTe thin films most likely comes from topological surface states.

Correction to magnetoresistance caused by WAL or WL in 2D system is described by Hikami-Larkin-Nagaoka [75] formula:

$$\Delta\sigma_{\perp}(B) = N\alpha\frac{e^2}{\pi h}\left[\psi\left(\frac{1}{2}+\frac{B_{\perp}}{B}\right)-\ln\frac{B_{\perp}}{B}\right],\ B_{\perp}=\frac{\hbar}{4|e|\,\ell_{\varphi}^2}, \tag{1.37}$$

Where l_{φ} is the phase coherence length, ψ is the digamma function, and N is a number of independent coherent channels. α is a symplectic universality class and for WAL it takes the value $-1/2$ whereas for WL one expects $\alpha = 1$. Measurements of WAL are particularly interesting in SnTe where number of conducting coherent channels can be changed by tuning a position of the Fermi level. This is because of the valley degeneracy, and multiple Dirac cones present in SnTe. Assaf et al. [68] prepared 40 nm thick (001) SnTe//BaF_2 thin films grown at five different temperatures for the study of weak antilocalization in this system. They found, that Hall mobility, carrier concentration as well as film morphology strongly depends on the growth temperature. This opened a possibility of studying WAL as a function of Fermi level position. Results of their experiments are summarized in the Fig 1.12. Panel (a) distinguishes three transport regimes depending on the Fermi level position (E_F). For low values of E_F assumes four Dirac surface valleys and zero bulk contribution. It should be noted that, the authors decided discuss their results, changing the sign of weak antilocalization prefactor to 1/2, however it is more common to use negative value instead. Thus the maximum value of α is 4 ($4 \times 1/2$ for each surface). Second regime considers transport after the Lifshitz transition i.e. when Dirac cones merge into four pairs of concentring energy contours as shown in the Fig 1.12(a). In this

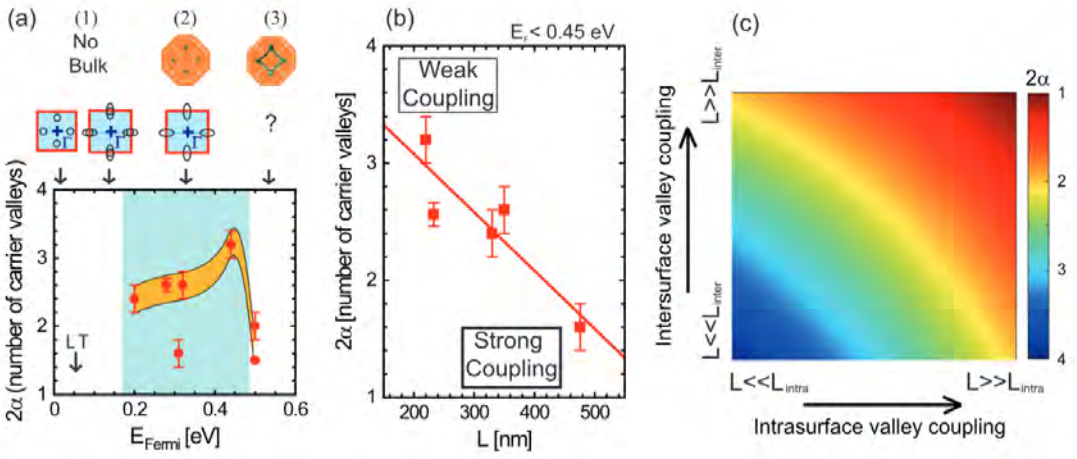

FIGURE 1.12: Fermi surface changes from as analyzed by WAL experiments. (a) 2α corresponds to a number of valleys plotted against the Fermi level position. (b) Number of carrier valleys as a function of phase coherence length. (c) Diagram illustrating variation of the number of valleys for itner- and intrasurface valley coupling. As reported in [68].

regime, number of surface valleys should be reduced by the factor of 2. Now in the last regime of transport when Fermi level is below 0.5 eV (as measured from the center of a gap), valleys at L point merge into large, tubular Fermi surface. In this regime both bulk and surface bands are occupied and α is approaching to $1/2$. Similar behavior is observed in other TIs with high carrier density. It can be explained by coupling of top and bottom surfaces by the bulk reservoir, which all together form single diffusive channel [76–79]. This is in good agreement with the trend presented in the 1.12(b), which shows scaling of the phase coherence length ℓ_φ with the number of coherent channels. As ℓ_φ increases carriers can coherently scatter between surfaces/valleys without phase-breaking processes which in the end leads to the formation of single coherent channel.

This is further confirmed in experiments which allow changing the carrier density with the gate. Thanks to the van der Waals structure of bismuth based TIs one can achieve reasonably high surface to bulk ratio, by the simple exfoliation. By depleting the bulk carriers several experiments shown top and bottom surfaces can be decoupled which is indicated by a change from $\alpha = -1/2$ to $\alpha = -1$. This change is attributed to formation of 2 independent coherent channels.

Recently, Dybko et al. [80] presented experiment which examines WAL in both the parallel and perpendicular field, varying the SnTe film thickness

from 10 to 100 nm. Measurements in the parallel field, allow to probe spatial extent of topological surface state λ, as proposed by Tkachov and Hankiewicz [81]. Although, spatial extent of topological 2DEG is not expected to vary with the thickness, experiments done by the authors reveal that, within the model of Tkachov and Hankewicz, such dependence exist. Surprisingly, the authors observed that λ always equals about 40 % of the film thickness. For comparison, ARPES measurements for Bi_2Se_3 found the spatial extent of TSS to be of the order of 2-3 nm [82]. The obtained result is yet another confirmation of the reservoir model mentioned beforehand. Recall that, topological Dirac fermions can scatter between surfaces via bulk reservoir without losing the phase coherence.

The number of experiments done on TCIs is modest, as compared to the TIs based on bismuth chalcogenides. The general behavior of low-field magnetoresistance is similar between the two. The distinction is the valley degeneracy in SnTe material class. This should manifest as higher number of coherent channels. Nevertheless, to date only one report on IV-VI based TCIs claimed to achieve more than one coherent channel in a controllable way [68].

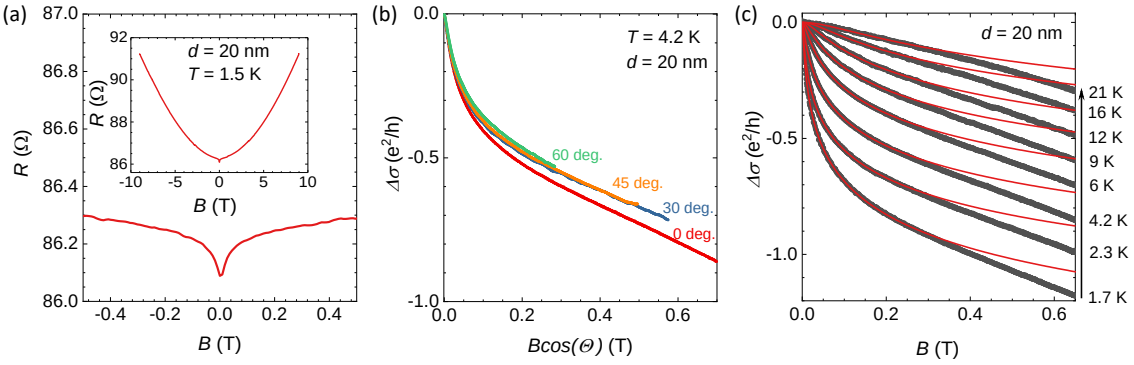

FIGURE 1.13: Representative example of weak antliocalization measurements in TCIs for 20 nm thick SnTe film. Panel (a) resistance as a function of magnetic field, inset present magnetoresistance measured up to 9 T.(b) Low field magnetoresistance angular dependence.(c) Low-field magnetoresistance measured and fitted with HLN formula at various temperatures. As reported by [80].

Quantum oscillations As described in the introductory section, density of states in a 2 dimensional electron gas (2DEG) splits to Landau levels, when subjected to sufficiently high magnetic fields. This splitting leads to oscillatory behavior of conductivity (Shubnikov - de Haas (SdH) oscillations), magnetization (de Haas - van Alphen (dHvA) oscillations) and other measurable

quantities like thermal conductivity, thermal EMF etc. These quantum oscillations are extremely useful in studies of 3D topological insulators. As 3D TIs and TCIs host 2DEG on their surface it is possible to distinguish its contribution from bulk conductivity.

Magnetoresistance oscillations were discovered in 1930 during low temperature studies of pure Bismuth crystals [33]. Schubnikov and de Haas observed that magnetoresistance oscillates periodically with the inverse of magnetic field. Interestingly, until the end of 50s people thought these oscillations are intrinsic Bismuth properties, until the same phenomenon was discovered in high mobility samples of InAs and InSb [83]. Since that time SdH oscillations became a basic tool used for characterization of new materials. It is commonly used to obtain effective g factor, effective mass and extreme cross sections of the Fermi surfaces. Oscillatory part of conductivity related to SdH effect is given by [35, 84]:

$$\Delta\sigma_{xx} \propto \cos\left[2\pi\left(\frac{F}{B} - \frac{1}{2} + \beta\right)\right] \tag{1.38}$$

where B is the magnetic field, F is the oscillation frequency and β is a phase shift. It is straightforward to obtain Berry phase γ from phase shift β, as β=$\gamma/2\pi$. Discrimination of the phase factor is then very powerful tool for distinguishing Dirac fermions with Berry phase of π with $\beta = 1/2$ from electrons with parabolic dispersion for which β=0 [85, 86].

Knowing the frequency F one can easily calculate the extremal cross-section of the Fermi surface normal to the field direction:

$$F = \frac{\hbar}{2\pi e S}, \tag{1.39}$$

However, for the case of topological properties of SnTe, we're mostly interested in the angular dependence. For a 2D system F should depend like $1/\cos\theta$. As such, for thin films SdH oscillations should vanish completetly for $\theta = 90^o$. In the case of TCIs every surface with mirror symmetry hosts 2DEG, which can lead to anomalous SdH frequency angular dependence. To date there were few reports on detecting quantum oscillations coming from TSS in SnTe material class.

The first report of quantum oscillations assigned to TSS in TCIs came in 2013 from the group of Yoichi Ando. Thin, 30 nm SnTe film was grown on Bi_2Te_3

buffer layer to improve quality of SnTe filmvb . As Bi_2Te_3 is intrinsically n-type, interface forms a p-n junction and causes band bending on the free SnTe surface[69]. The authors observed clear SdH oscillations and assigned them to the n-type Dirac fermions residing at (111) surface of SnTe. Okazaki et al. [87] measured magnetotransport up to 30 T in single crystalline 2 μm SnTe film grown on (111) BaF_2 substrate. The authors didn't attribute measured oscillations to TSS although they determine $1/\cos\theta$ dependence of measured SdH frequencies. This is because for (111) oriented SnTe films this behavior can come from elongated bulk Fermi ellipsoids. An interesting conclusion

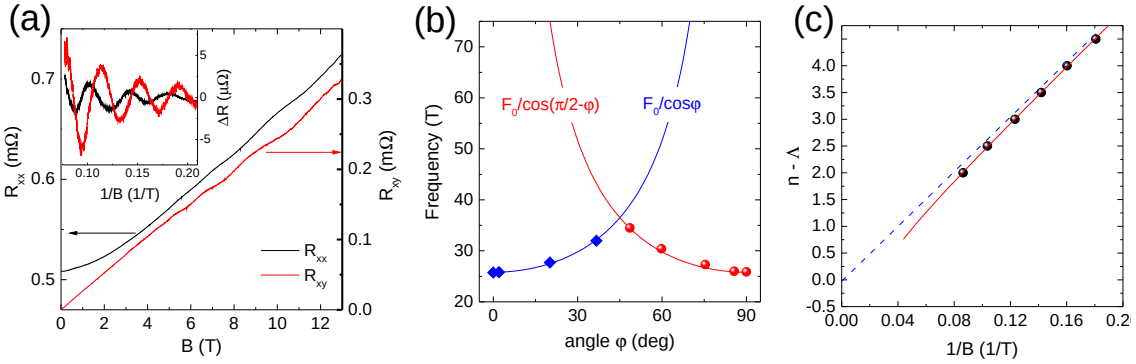

FIGURE 1.14: Representative example of SdH oscillations in TCIs for SnTe bulk crystal. Panel (a) R_{xx} and R_{xy} as a function of magnetic field, inset presents oscillatory component obtained by background subtraction.(b) Frequencies of SdH oscillations, blue lines and points represents contribution from top and bottom surface of the crystal, red lines and points correspond to side surfaces. (c) Analysis of Landau Level indicies for R_{xx} surfaces indicating Berry phase of π. Figure adapted from Ref [84].

came from magnetotransport and magnetization measurements performed on a SnTe bulk crystal. Dybko et.al [84] experimentally confirmed that as grown SnTe bulk crystal is surrounded on all sides by the metallic 2D topological surface states. Contribution from neighbouring, perpendicular surfaces manifested in both SdH and dHvA effects by angle measurement. This is best seen in the Fig 1.14. Panel (b) illustrates angular dependence of observed SdH frequencies. By titling the field with respect to the (001) one observes two frequencies contributing to the spectra. According to the interpretation put forward by the authors, they come from neighboring crystal surfaces. Indeed, at the characteristic angle of 45^o the 2DEG residing on the side surface takes the dominant role in the SdH oscillations. By analyzing Landau level indices authors determine Berry phase of π which is expected for Dirac fermions.

1.3.1 Future prospects

In principle TCIs based on IV-VI semiconductors offer much richer landscape of phenomena which can appear due to violation of mirror symmetry in the crystal, and multiple Dirac cones present in this system. A topological 2DEG at the surface of TCI should exhibit a quantum Hall effect, however so far there was no report on this regard. Several proposals suggested how to achieve Quantum Anomalous Hall [88, 89] effect, which is particularly interesting because of high quantized conductivity value. By placing thin SnTe film between two layers of ferromagnetic insulators (EuS), Assaf et al. [90] observed proximity induced ferromagnetism and its impact on transport properties of SnTe, however no indication of Quantum Anomalous Hall Effect has been observed. Despite the fact, SnTe or SnSe grown in a [111] crystallographic direction are predicted to realize Quantum Spin Hall state [91, 92], so far TCIs have only been realized in three dimensional systems. Transition to a Quantum Spin Hall state shows oscillatory thickness dependence leading to a complex phase diagram of topological phase transition. Interestingly, a thin TCI film grown in the [001] crystallographic direction is theoretically predicted to realize another 2D topological crystalline phase, which ultimately may lead to the creation of topological transistor. In this state thin films of SnTe or (Pb,Sn)Te(Se) host spin-filtered edge states over wide range of film thicknesses. Application of external electric field will break the mirror symmetry, open the edge gap and consequently drive the system to a topologically trivial state [93]. All above mentioned proposals are awaiting experimental realization, with the film quality improvement as the biggest challenge. Hypothetically using an insulating buffer with cubic crystal structure can improve structural quality of thin IV-VI films. A ballistic quantum transport was achieved for PbTe thin films grown on Eu-doped PbTe [94, 95]. Eu will introduce disorder to the buffer layer which will drive the system into insulating state through Anderson localization. It can be hypothesized that TCIs film grown on Eu-doped PbSe or SnTe may lead to high-quality thin films and consequently observation of quantum transport mediated by topological edge/surface states.

1.4 Characteristics of IV-VI semiconductors

Lead telluride and tin telluride are narrow gap semiconductors taking the rock-salt structure (Fig. 1.15. The crystal lattice consists of two equivalent face centered cubic sublattices displaced by a half of lattice parameter in the <111> direction. For PbTe lattice parameter is equal to a=6.46 Å at room temperature. Under hydrostatic pressure PbTe undergoes a phase transition to a orthorombic phase, and becomes wide band gap semicondcutor.
For tin tellruide, lattice parameter is equal to $a = 6.30$ Å for the samples with low carrier density. For strongly doped SnTe crystals however, the lattice parameter depends also on the carrier concentration. It decreases as carrier denisty increaseas as described in [96]

$$a_0 = 6.327 - 1.7 \times 10^{-23}\, p\, [cm^{-3}] \tag{1.40}$$

where p corresponds to tin concentration. High hole density in SnTe is due to tin vacancies which reduces the lattice parameter (usualy number of tin vacancies is of the order of atomic percent). For the samples with $p = 10^{20} - 10^{21}$ cm^{-3} lattice parameter decreases by 0.3 % down to 6.31 Å. This effect becomes less prominent with the Pb doping as Pb reduces conentration of holes to $p = 10^{17} - 10^{19}$ cm^{-3} for lead telluride. SnTe similarly to PbTe undergoes a phase transition to the orthorhombic phase under hydrostatic pressure of the order of P=20 kbar.

There are several reports on the low-temperature crystal structure of SnTe and its alloys with Pb, where its NaCl cubic lattice transforms to a rhombohedral structure. The temperature of this phase transition decreases with increasing concentration of Pb, and consequently as carrier density increases. Contrary to the orthorhombic phase, transition to a rhombohedral structure does not have a substantial influence on the material band structure. This is because rock-salt structure of IV-VI semiconductors deforms only by a few degrees along <111> direction.
Lead and tin tellurides form solid solutions in the whole composition range. The lattice parameter for these obeys the Vegards law and is described by formula below [97]:

$$a_0 = 6.46 - 0.13y\, [\text{Å}] \tag{1.41}$$

Crystals of $Pb_{1-y}Sn_yTe$ are solid solutions of SnTe and PbTe.

Magnetic Mn^{2+} ions if introduced to the lattice, are substiting Sn^{2+} and Pb^{2+} cations.

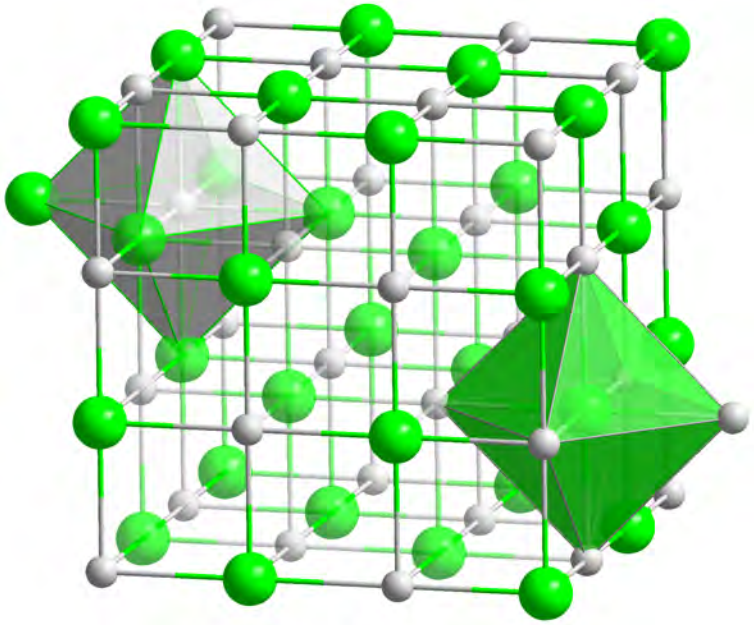

FIGURE 1.15: Rock salt crystal structure.

Properties of bulk SnTe band structure $Pb_{1-y}Sn_yTe$ is a narrow gap semiconductor. In the helium temperatures the band gap of SnTe is E_0=300 meV and E_0=190 meV for PbTe. With the increasing amount of tin for $Pb_{1-y}Sn_yTe$ band gap is decreasing from E_0=190 meV for PbTe to reach zero for approximately $y = 0.35$. For higher Sn concentration the band gap inverts and increases to approximately 300 meV for SnTe in the liquid helium temperature. Of course, the band gap depends on temperature as well, and in the room temperature, zero band gap is seen for $y = 0.6$. Both valence and conduction bands are strongly non-parabolic. The bottom of conduction band and top of valence band are located in the L-point of the Brillouin Zone i.e at the border of the Brillouin Zone in the [111] direction. Both valence and conduction bands have 4 equivalent energy valleys along [111] direction, also the effective mass in these materials is highly anisotropic (K=m_l/m_t=10). PbTe and SnTe have second valence Σ band which lays approximately 200-300 meV below the edge of the main valence band.

1.4.1 Generation of charge carriers in IV-VI semiconductors

As in IV-VI semiconductors, charge carriers can be used to drive the system into the ferromagnetic or superconducting state, it is instructive to discuss mechanisms of charge generation and ways of controlling the charge density.

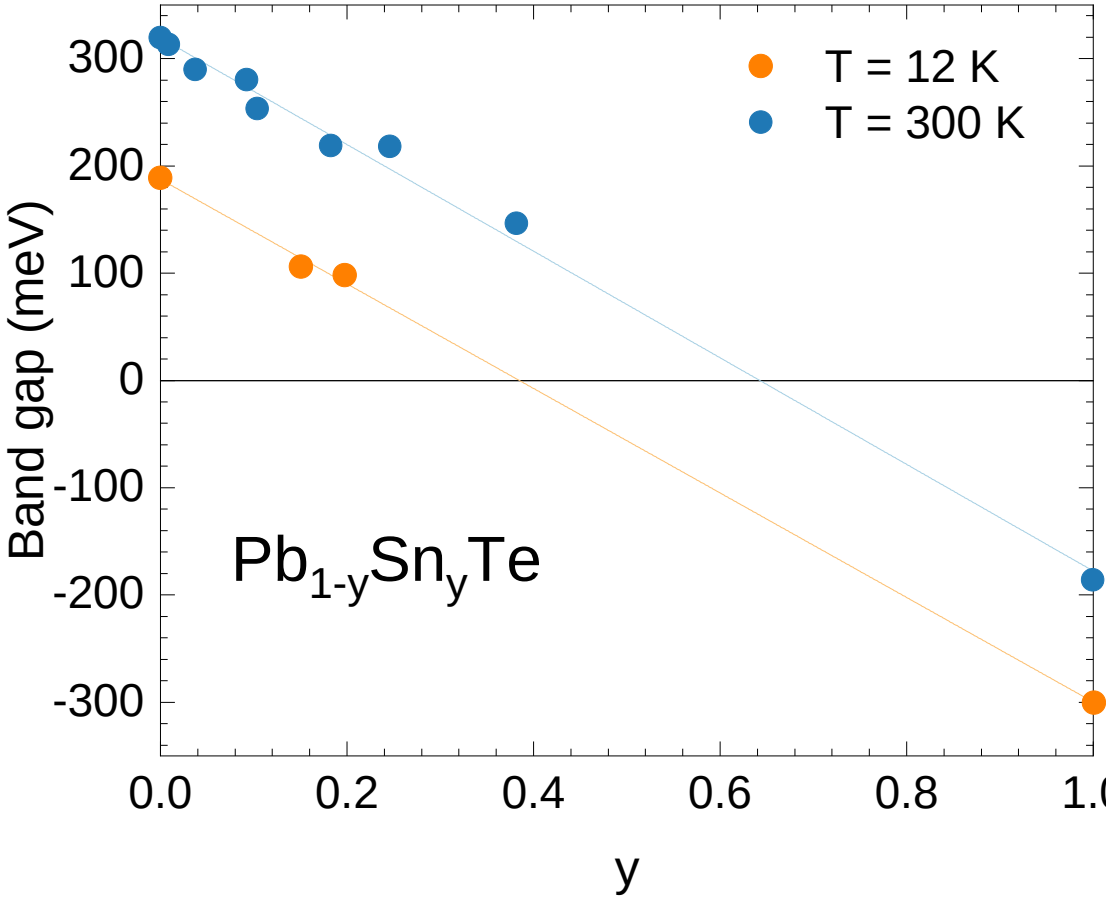

FIGURE 1.16: Dependence of the energy gap on the tin concentration **y** and temperature for $Pb_{1-y}Sn_yTe$. Experimental points are taken from the, laser emission, absorption, photovoltaic effect and tunneling measurements [98].

The carrier density in IV-VI semiconductors is governed by the number of metal and nonmetal-vacancies, which create holes and electrons respectively. Previous works on these materials do not suggest any correlation between the amount of Mn ions in IV-VI matrix and the conduction type or density. Detailed research on IV-VI materials shown they are highly degenerate, usually p-type semiconductors with very high carrier density which weakly depends on temperature. This materials class exhibit metallic conductivity. For sufficiently strong p-doping SnTe and SnMnTe can superconduct, however, even a minor amount of manganese ions can destroy superconductivity as pointed out in the Ref. [99].

Hemstreet [100], as well as Pratt & Parada [101, 102], found an explanation of the metallic behavior of these semiconductors. They noticed a correlation between material density and carrier density. In short, p-type doping is realized by metal vacancies (Tellurium excess), whereas n-type conduction is due to Tellurium vacancies (Pb, Sn excess). The results coming from these

calculations can be summarized as follows:

1. If metallic vacancy is created (i.e., Sn or Pb is removed from the lattice), it removes 4 valence electrons. This is because the outer valence shell of Pb contain four electrons $6s^2 6p^2$. Simultaneously, from a group of the valence band one energy state is separated and moves towards conduction band. This free state in the valence band after taking into account spin degeneration generates two conduction holes.

2. Non-metallic vacancy (Te) - if a Te atom is removed, 6 charge carriers in valence band are removed as well (outer Te shell - $5s^2 5p^4$). At the same time, as suggested by theoretical works, 4 states are separated from the conduction band. This means that six valence electron are gone, but there are eight less states for carriers in the conduction band. As a result, two excess electrons go to the conduction band and promote n-type conductivity.

1.5 Dilute Magnetic Semiconductors

SnTe among many topological materials is known to exhibit low-temperature ferromagnetic phase when doped with manganese. This offers a possibility of studying interactions between topological states and ferromagnetic ordering. A brief overview of semiconductors doped with magnetic atoms is given below.

$Sn_{1-x}Mn_xTe$ is a member of a broader family called *dilute magnetic semiconductors* (DMS). In this type of compounds a part of the cations are substituted by atoms with non-zero magnetic moment. Usually these magnetic elements are 3d transition metals or rare earths [103–105]. In the early days of DMS, most of the research was devoted to manganese doped II-VI semiconductors like $Cd_{1-x}Mn_xTe$ or $Zn_{1-x}Mn_xSe$. Before discussing magnetic properties of Mn doped IV-VI semiconductors, we briefly survey magnetic interactions occurring in DMS's.

1.5.1 Magnetic interactions in Dilute Magnetic Semiconductors

For canonical ferromagnetic materials magnetic ordering emerge due to the direct interaction between atoms possessing magnetic moments. This interaction is called *direct exchange*, and assumes non-zero overlap between wavefunctions of neighbouring atomic orbitals. The interaction is purely quantum mechanical and is a result of the Coulomb energy difference between neighbouring spinful magnetic ions. Naturally, its strength falls rapidly with the distance between the atoms and usually vanishes for separations greater then 0.5 nm.

Exchange interaction does not necessarily need to result from the wavefunction overlap of the neighbouring orbitals. Sometimes, it can be mediated via non-magnetic neighbour due to hybridization between atomic orbitals. In the *superexchange* model a paired valence band electrons of the semiconducting lattice and d electrons of the localized moment are virtually exchanged. This usually leads to an antiferromagnetic coupling, as ferromagnetic contribution sharply decays with the increasing interatomic distance. Superexchange interaction dominates in II-V and II-VI DMS's.

For materials with high carrier density, spin-polarized gas of charge carriers can mediate interaction between magnetic ions. The most common type of interaction is called RKKY interaction, after Ruderman, Kittel, Kasuya and Yosida [106–108]. RKKY considered a problem of an atom with localized magnetic moment surrounded by a Fermi sea of itinerant carriers. They will respond to the non-zero magnetic moment of an atom with non-uniform, oscillatory spatial spin density distribution to screen it. Qualitatively it is very similar to the Friedel oscillations of charge density caused by a charged, point-like perturbation. Ruderman and Kittel preformed calculations to solve this problem assuming parabolic dispersion and full degeneracy of the electron gas. The spatial dependence proposed within this model is shown in the Fig 1.17 and the resulting interaction energy density is given below:

$$F(\xi) = \frac{(\sin(\xi) - \xi\cos(\xi))}{\xi^4} \tag{1.42}$$

where: $\xi = 2k_F r$ and k_F is a Fermi wave vector. In the qualitative picture of this interaction, magnetic ion is polarizing the spins of charge carriers which

then travel through a crystal and align the next magnetic ions ferromagnetically or antiferromagnetically, depending on the phase of $F(\xi)$. RKKY interaction strength decreases with the distance between magnetic atoms in an oscillatory way as seen in the Fig 1.17. Oscillating character of this interaction can either force ferro- or antiferromagnetic ordering of the localized spins. For disordered systems, it can lead to a spin-glass phase.RKKY interaction is usually observed in a conducting systems with randomly distributed magnetic ions or in rare earth metals.

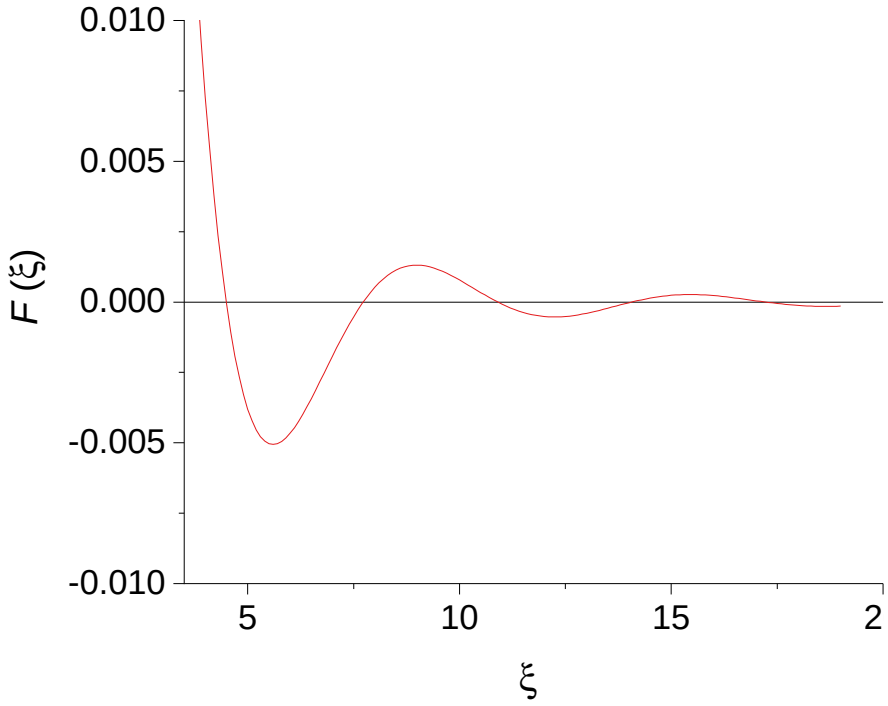

FIGURE 1.17: RKKY energy density as a function of parameter ξ which is proportional to distance between magnetic ions.

1.5.2 p-d Zener model

A breakthrough in DMS research came in the beginning of the new millennium. Despite initial progress in doping semiconductors with magnetic ions, the ferromagnetic phase emerged well below the temperature of liquid nitrogen, making potential applications elusive. This have changed with the emergence of (III, Mn)V DMS's, especially $Ga_{1-x}Mn_xAs$. Almost instantly, first reports for this system yielded ferromagnetism at temperatures as high as 110 K, unprecedented by any other DMS [109]. RKKY interaction can explain this only in a qualitative way. For sufficiently high hole concentrations and Mn doping levels, the value of ξ (1.42) is smaller than the first

zero of F(ξ). This implies that hole-mediated exchange interaction will lead to a ferromagnetic ordering in $Ga_{1-x}Mn_xAs$. Also, in this regard RKKY interaction can be thought as limiting case of carrier mediated magnetism proposed by Clarence Zener in the 50's [110]. However, the RKKY model has some drawbacks when comes to describe ferromagnetic phase in III-V DMS's. For instance, it does not capture the spin splitting of carrier bands induced by the Mn ions [111]. In 2001 Dietl et al. [112, 113] proposed a *p-d Zener model* of hole-mediated ferromagnetism. Within this approach spin-splitting of the bands results in lowering energy of conduction holes, at the same time neglecting the oscillatory behavior of RKKY interaction. This model captures the effect of strain on the magnetic anisotropy in $Ga_{1-x}Mn_xAs$ [114], as well as explained with good accuracy high temperature ferromagnetic phase [115]. Additionally, within this framework one can find that some semiconductors should be ferromagnetic at the room temperature. Magnetically doped GaN and ZnO are supposed to exhibit ferromagnetism at room temperature for hole concentration of the order of $5 \times 10^{20}\,\mathrm{cm}^{-3}$. However, as such high carrier concentration is usually not observed in oxides nor nitrides, a room temperature ferromagnetic semiconductors still remains to be realized.

IV-VI Dilute Magnetic Semiconductors Mn doped IV-VI semiconductors can be conceptually divided into two groups, with respect to carrier concentration. First group consists of the compounds with low carrier density like $Pb_{1-x}Mn_xTe$ or $Pb_{1-x}Mn_xSe$ with carrier density between 10^{17}-$10^{19}\,\mathrm{cm}^{-3}$ [116]. All of these compounds are paramagnetic, for $Pb_{1-x}Mn_xTe$ a low-temperature spin-glass phase has been reported [117]. In a spin-glass phase the magnetic moments of the magnetic ions are frozen in random directions. This randomness is due to competition of interaction between the spins as they are randomly distributed over the crystal lattice. This competition may be caused by the position of the ions, if an antiferromagnetic interaction is present in the material or, if both ferro and antiferromagnetic interactions are competing. In the second group of IV-VI DMS there are materials with rather high carrier concentration like $Sn_{1-x}Mn_xTe$ and $Ge_{1-x}Mn_xTe$. Usually carrier concentration in these materials falls between $10^{20} - 10^{22}\,\mathrm{cm}^{-3}$. These systems often exhibit low temperature ferromagnetic phase. The first systematically studied IV-VI ferromagnetic semiconductor is $Pb_{1-y-x}Sn_yMn_xTe$ and $Sn_{1-x}Mn_xTe$. Story et al. [118] reported that ferromagnetic phase can be controlled by concentration of free carriers. In the figure 1.18, the Curie

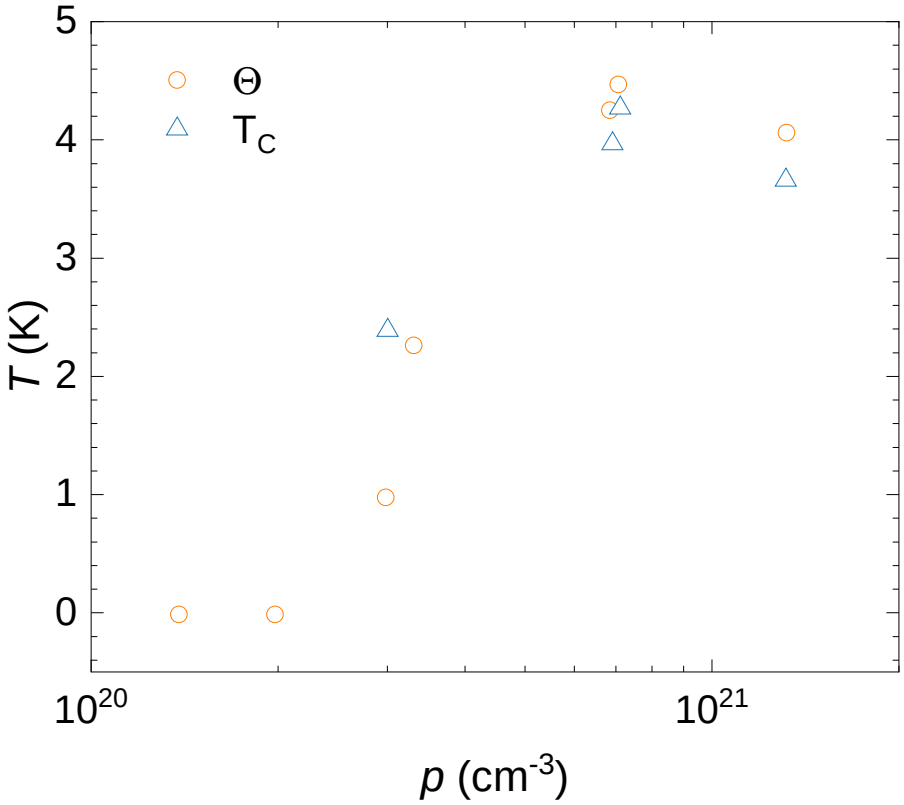

FIGURE 1.18: Curie temperature (T_C) and Curie-Weiss temperature (Θ) for $Pb_{0.25}Sn_{0.72}Mn_{0.3}Te$ at various carrier densities. Reproduced from data reported by [118].

and Curie-Weiss temperatures are plotted as a function of carrier density for $Pb_{0.25}Sn_{0.72}Mn_{0.3}Te$. The Curie-Weiss temperature is a measure of all magnetic interactions present in the material. Its non-zero value indicates that some interaction between magnetic ions is indeed present in the studied system. The Curie temperature is defined as a transition temperature to a ferromagnetic phase. One can straightforwardly deduce from the figure, that for some critical carrier density p_c, the ferromagnetic ordering emerges suggesting that the mechanism which drives magnetic ordering is related to a carrier density. Swagten et al. [119] noticed that this can be explained by invoking RKKY interaction and band structure of $Pb_{1-y}Sn_yTe$. Existence of a second valence Σ band is essential for ferromagnetic interaction to occur. The Σ band is very strongly, twelve-fold degenerate which not only affects the Fermi wave vector, but also the prefactor of RKKY interaction [118]. Secondly, the effective hole mass in the Σ band is much greater than hole mass in the L-band. According to the plasma reflectivity measurements[120], effective mass in a parabolic Σ band can reach m^*_Σ=1.7m_e whereas for non-parabolic L-band it is only m^*_L=0.05m_e according to Ref. [121]. Knowing the impor-

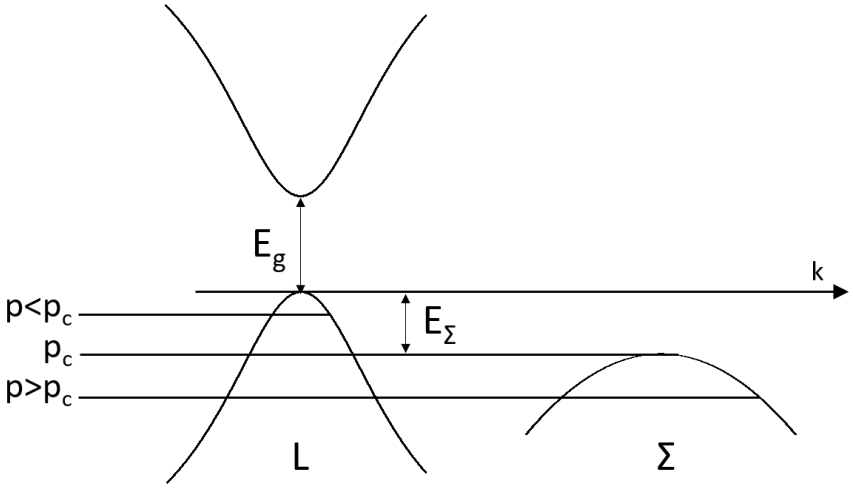

FIGURE 1.19: A schematic of a band structure of $Pb_{1-x-y}Sn_yMn_xTe$. For high carrier density the second valence band with heavy holes becomes populated. For the carrier density smaller then critical density p_c only the light hole band is occupied.Reproduced from the Ref. [119]

tance of the second valence band and the carrier density, we can now look at the scheme presented in the Fig. 1.19 and data in the Fig 1.18. For the carrier density p lower than p_c=2.5$\times$ 10^{20} cm^{-3} only L-band is occupied which results in a weak RKKY coupling. Now if p > p_c i.e. Fermi level lies within the Σ band introducing heavy conduction holes. This results in a much stronger RKKY coupling and orders diluted Mn ions ferromagnetically. Later studies explored magnetic phase diagram of $Pb_{1-x-y}Sn_yMn_xTe$[122], and found that the critical carrier density p_c weakly depends on the Mn concentration. It changes from p_c=2.5$\times$ 10^{20} cm^{-3} for 3 and 8 % of Mn to p_c=3$\times$ 10^{20} cm^{-3} for 12 % of Mn.

As PbTe and SnTe are fully soluble, $Pb_{1-x}Mn_xTe$ and $Sn_{1-x}Mn_xTe$ can be considered as a limiting cases of mixed compounds $Pb_{1-x-y}Sn_yMn_xTe$, we can assume that the difference in magnetic behavior comes from the difference in carrier density.

In terms of topological properties of $Sn_{1-x}Mn_xTe$, the physical picture is less clear. Although ARPES measurements haven't been performed either on the bulk crystals nor thin films, there are arguments, that Mn alloying does not

restore trivial band ordering. First, the crystallographic structure is unaffected by the doping, as well as lattice parameter does not fall in the topologically trivial regime (PbTe). Story et al. [123] explored the band structure of paramagnetic (Pb,Mn,Sn)Se where Mn doping up to 4 atomic percent didn't affect the TCI state. Instead, the band inversion point temperature was lowered. Also, as time-reversal symmetry is not critical for the existence of the mirror-symmetry protected topological states, they should be robust against ferromagnetism. Taking into account all the above arguments, we will assume throughout this thesis that Mn-doped $Pb_{1-y}Sn_yTe$ is topological, at least in the vicinity of liquid helium temperature.

Chapter 2

Experimental Techniques

2.1 SQUID Magnetometry

A substantial amount of research in this thesis was done by using SQUID magnetometry. In particular, I have been using commercially available SQUID magnetometers Quantum Design Magnetic Property Measurement System (MPMS). These systems are capable of doing measurements in the temperature range of 1.8-400 K and generate a magnetic field up to 7 T. Laboratory of Cryogenic and Spintronic research has two magnetometers of this kind. The manufacturer guarantees sensitivity down to 10^{-8} emu. This measurement precision is achieved through a reciprocating sample option (RSO). In this method, magnetometer moves the sample through detection coils in a sinusoidal way. A phase sensitive detection employed in this setup improves signal-to-noise ratio and helps to eliminate high-frequency noise and reduce $1/f$ noise. Additionally, the servo motor which moves the sample holder inside the chamber can acquire measurement data without movement interruption. This allows for multiple averaging during the measurements and results in above-mentioned measurement resolution. The magnetometer possesses convenient options which help to solve common experimental challenges. First, the MAGNET RESET option. Superconducting magnets are known to possess some remnant field, especially after a trip to high magnetic fields. In type II superconductors quantized field fluxes are penetrating superconducting medium. These trapped magnetic vortices called *fluxons*, are responsible for the remnant magnetic field in superconducting coils. By warming part of superconducting coil above its critical temperature, with some small amount of current inside, drives the coil into its normal state and thus removing fluxons from the system. SQUID detection coils form precisely equilibrated differential second order gradiometer. Such a coil directly measures the second derivative of magnetic field flux coming from the magnetic moment of an investigated specimen. This gradiometer has 3 cm length

and 1.94 cm in diameter. Such a configuration of pick-up coils is largely insensitive (down to 0.1 %) to a uniform magnetic field, which means that use of SQUID sensor should be possible even if the magnetic field changes in large steps. Flux transformer consists of 3 coils, however, the middle coil has twice as many threads, and it is wounded in the opposite direction, as compared to side detection coils. Then the pick-up coils' wires are connected at the helium bath close to the actual SQUID sensor.

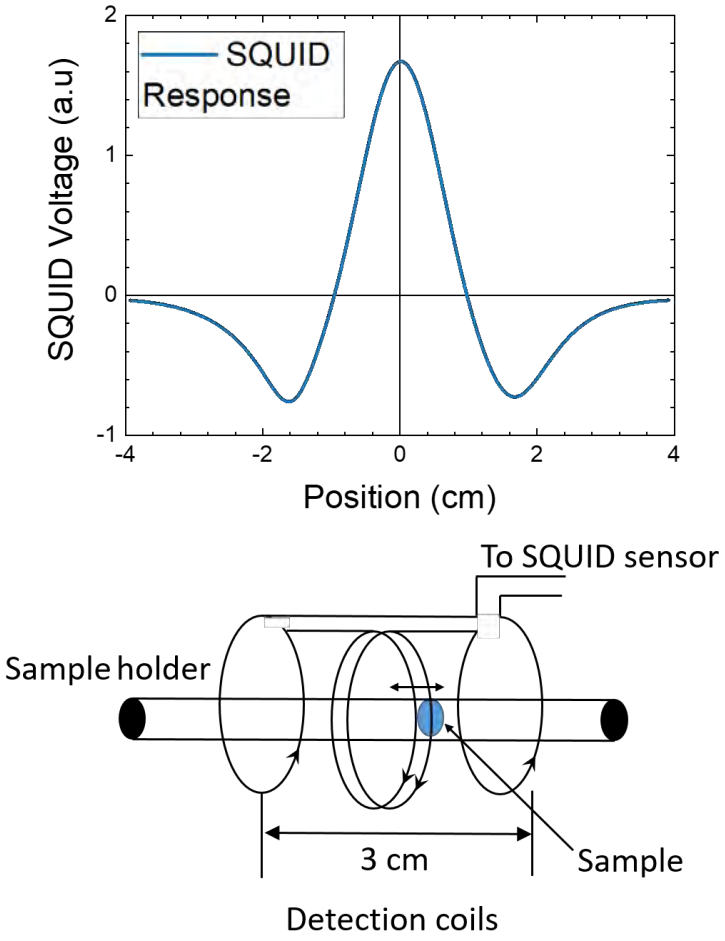

FIGURE 2.1: Schematic of signal detection system utilized in the SQUID magnetometer. Measurement is taken during sample movement. Amplitude of SQUID voltage is proportional to measured magnetic moment.

The voltage-position relation is used for estimation of samples' magnetic moment:

$$V(z) = R\left(\frac{2}{(\rho_0 + (z - z_0)^2)^{3/2}} - \frac{1}{(\rho_0 + (z - z_0 - \Lambda)^2)^{3/2}} - \frac{1}{(\rho_0 + (z - z_0 + \Lambda)^2)^{3/2}}\right)$$

where:

- R - calibration constant
- ρ - detection coil radius
- z_0 - center of the sample with respect to detection coils
- Λ - distance between detection coils

The graph of V(z) is presented in the Fig 2.1. Signal amplitude is directly proportional to the measured magnetic moment and its maximum corresponds to the central position of the sample inside the detection coils. The software provided by manufacturer fits V(z) using leasts square method and calculates corresponding magnetic moment of the sample.

2.2 Electron transport measurements

2.2.1 Point contact spectroscopy

Many measurement techniques used in experimental physics nowadays demands sophisticated apparatus which sometimes is limited to a few laboratories across the globe. Even the SQUID magnetometer described above relies on the synergy of quantum device, state of the art electronic controlling both the measurements and its conditions like temperature or magnetic field. It is almost unbelievable how many interesting information can be extracted from a simple junction of two metals. In 1974, USSR Kharkov, Yanson studied tunneling conductance in a NIS structure (Normal - insulator - Semicondcutor). To his surprise, he found non linear behavior of the junction in the normal state of Pb. He realized that Pb is shorted to a normal metal electrode, and what he sees is not a tunneling process. This is how point-contact spectroscopy was born. There are many ways of fabricating point contact, most common are gathered in the Fig 2.2.

Nowadays, the most used technique simply relays on the contacting electrode and the sample of interest through micromechanical apparatus. This measurements configuration is called a needle-anvil method (Fig 2.2(c)). One electrode is usually an electrochemically etched metallic tip whereas the second electrode is the sample of interest. The ending of the tip can reach a diameter of several micrometers however it does not define effective contact area. Instead, electronic transport occurs via multiple parallel channels much smaller in size. As there is always some amount of pressure exerted by the tip it typically deforms during the measurement process. Even though the

tip gets deformed, the sample is not usually damaged and multiple measurements can be performed in one cooling cycle. The resistance of the junction can be tuned by a micrometric screw which changes the tip position in the direction perpendicular to the sample plane. If any oxide layer is present on the surface layer, the tip will pierce through it and access the actual sample. The hard point contact method also has some drawbacks. Very often

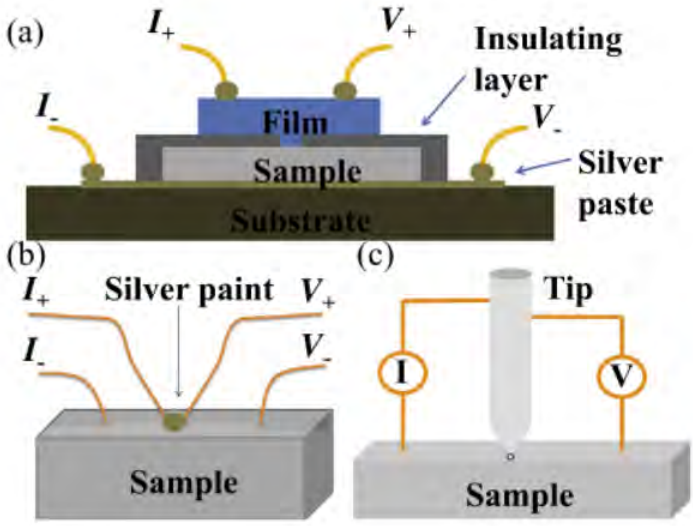

FIGURE 2.2: Experimental setups for point contact spectroscopy measurements.(a) Litographically defined point contact (b) "Soft" point contact configuration. where tiny drop of silver paint or flake of In is put on the sample surface. (c) Hard point contact technique involving metallic tip pressed against the sample surface. As appeared in the Ref.[23]

junctions formed by this technique are thermally and mechanically unstable which may call for multiple measurements to collect full data set for a single point contact. Also in the case of very small samples procedure becomes cumbersome. This situation happened when MgB_2, an exotic BCS superconductor which emerged in the early 2000s. People were fascinated by its unusually high critical temperature T_C=39 K and possible two-band superconductivity. Point contact measurements would have been an excellent tool to prove the complex nature of superconductivity, but the small size of single crystals made the entire procedure extremely difficult. Gonelli et al. [124] fabricated point contacts by putting a minuscule drop of silver paint against the sample surface. Although the Ag paint drop diameter falls between 10-50 μm, the actual contact is formed by individual Ag paint grains, so conceptually this technique is equivalent to the needle-anvil method, as it leads to multiple parallel transport channels. Surprisingly, there are some advantages

over standard hard-point contact as well. The first obvious advantage is that these contacts do not involve any external pressure. This can matter for a structurally soft materials, like IV-VI semiconductors. Second, these contacts are much more mechanically and thermally stable than the hard ones, and thus they are suitable for cryogen-free systems. In such a cryostat, low temperature is maintained by a cryocooler, which usually generates vibrations. These vibrations impact fragile junction formed by the tip and consequently complex damping mechanisms are necessary to implement this type of measurements in a dry system. As contacts made of Ag paint are very small, even minute facets of single crystals are accessible for point-contact measurements. Unfortunately, there are shortcomings to this technique as well, especially when it comes to changing contact area. Once soft point contact is made, the only way to modify its effective contact size is by a current or voltage impulses. This causes individual silver grains to create new junctions to the sample, while some of the previous ones vanish. Hard-point contact offers much higher level of control in this regard.

2.2.2 Transport through a point contact

As it was already shown by Yanson [125], the crucial parameter in the study of point contacts is its size a as compared to the mean free path l in the studied material. This determines if one is able to extract spectroscopic information from the measured spectrum. There are many excellent reviews in this topic, however this section is based on a review by Daghero and Gonelli [126], which puts some emphasis on soft-point contact technique.

Ballistic regime As there are no scattering events, the voltage V applied over the contact will grant electrons kinetic energy of eV. The gained kinetic energy directly reflects the energy difference between split Fermi surface(see Fig 2.3a). In this transport regime, both momentum and energy resolved measurements are possible, making point-contact spectroscopy simple and robust tool for studying local properties of Fermi surface. Sharvin was first to address the problem of ballistic transport through such a metallic constriction, and consequently, the corresponding point contact resistance is called *Sharvin resistance*:

$$R_S = \frac{4\rho l}{3\pi a^2} \tag{2.1}$$

Where ρ is the resistivity of the material. The same equation can be rewritten in terms of unversal constants:

$$R_S = \frac{4R_0}{(k_F a)^2} \tag{2.2}$$

where R_0= 12.9 kΩ is a resistance quantum. We can draw an important conclusion out of Sharvin's result, namely that resistance of a point contact in the ballistic regime depends solely on its size and geometry, as k_F is determined by the material under study.

If the contact size is larger than mean free path for elastic scattering but smaller than inelastic diffusion length, quasiparticles will lose momentum information but still can diffuse through the contact preserving the energy. In that case quasiparticles are isotropically redistributed over the Fermi surface as seen in the Fig 2.3b. Commonly we refer to this transport regime as diffusive regime.

Thermal regime On the opposite end, when the inelastic mean free path is much smaller than the contact size, contact falls into the thermal regime. In this regime, electrons lose all of the spectroscopic information through the scattering events within the contact(see Fig 2.3c). Maxwell calculated the resistance of a junction in such conditions and the corresponding formula reads:

$$R_M = \frac{\rho}{2a} \tag{2.3}$$

Also, because of the scattering events in the contact area, a finite voltage bias will result in a Joule heating under the contact. One can estimate the maximum temperature by using following formula [127]:

$$T_{max}^2 = T_{bath}^2 + V^2/4L \tag{2.4}$$

where L is the Lorenz number. Roughly, when $T_{Bath} << T_{PC}$, one can estimate the amount of heat generated during the measurement. Ref. [23] estimate it at the level of 3.2 K/mV.

Intermediate Regime Wexler noticed, that these extreme regimes can be linked by a simple interpolation. He derived a formula for a contact resistance with finite contribution coming from Sharvin and Maxwell resistances.

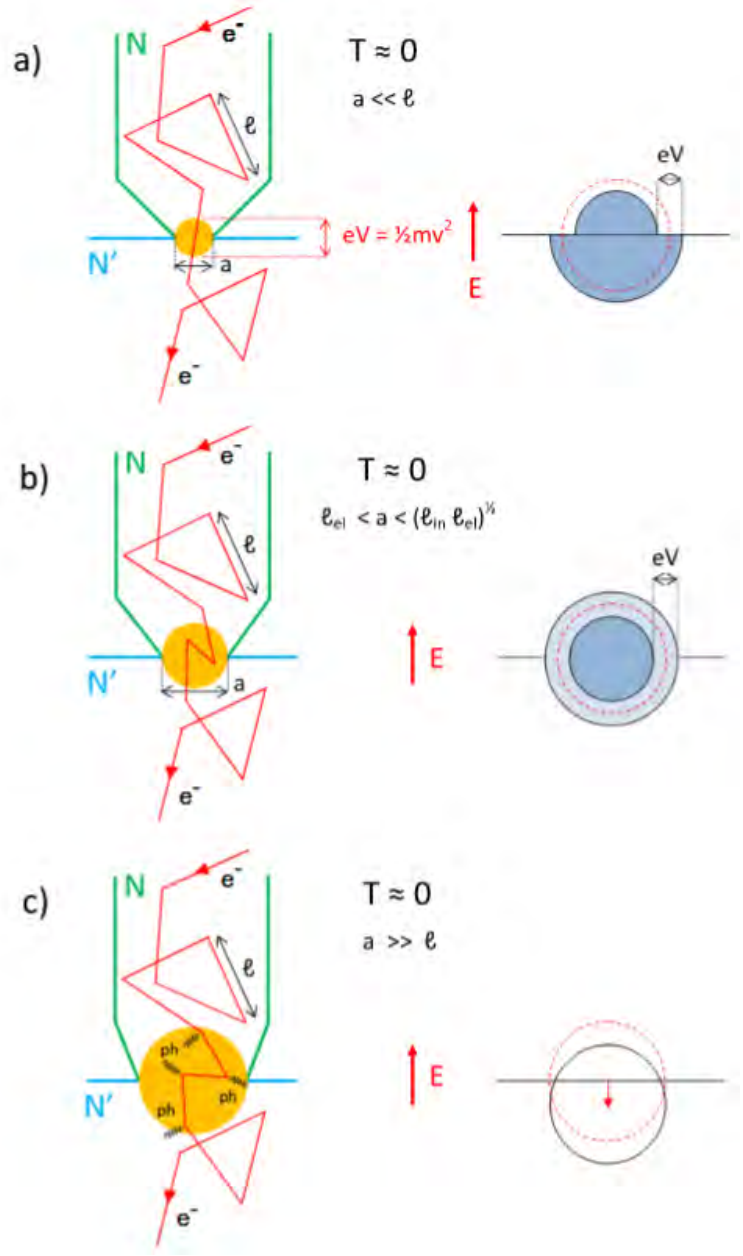

FIGURE 2.3: Transport regimes through a point contact. (a) Left panel In the ballistic regime electron is not subjected to any scattering processes. Right panel: A schematic illustration of the Fermi surface, in the ballistic regimes the surface is formed by two half-spheres which differ in radii by the factor of eV. Panel b) depicts transport in a diffusive regime. In this regime momentum information is lost. Panel c) corresponds to the thermal regime, where both elastic and inelastic scattering take place across the contact. Adapted from the Ref. [126].

For a contact between two metals of the same kind the resistance is given by:

$$R_{\mathrm{PC}} = \frac{4R_0}{(k_F a)^2} + \Gamma\left(\frac{a}{l}\right)\frac{\rho}{2a} \tag{2.5}$$

Where Γ is slowly varying function of the order of unity. In general, point contacts have non-zero contributions from both spectroscopic and thermal regimes that are weighted by the size of the contact only. Realistically a non-zero ballistic and thermal contribution are always present in the point contact spectra.

2.2.3 The estimation of point contact size

Naturally, point contact spectroscopy should be performed in the ballistic regime to obtain accurate energy and momentum information. It is straightforward to see from the above consideration that a critical parameter is the effective contact size compared to the mean free path. It was already shown by Baltz et al. [128] that a footprint of a tip used in hard point contact measurements is of the order of several microns, a thousand times more than a size of mean free path. This implies that several much smaller channels are in fact responsible for carrying a current. The same reasoning applies to the soft-point contact experiments. Figure 2.4 presents photographs of an actual point contacts made with the silver paint. It can be clearly seen, that a footprint of the contacts has diameter of several micrometers. Although, Wexlers formula can give an upper bound for the contact resistance, its actual size will remain unknown. This is because, conduction occurs via multiple parallel channels despite, the method we choose. This is because only information about the contact is its resistance, which results from coupled system of parallel resistors.

To confirm that our point-contact is indeed spectroscopic, or at least carry some spectroscopic information, one should carefully examine measured conductance spectra. Detailed description will be given in the discussion section of this thesis.

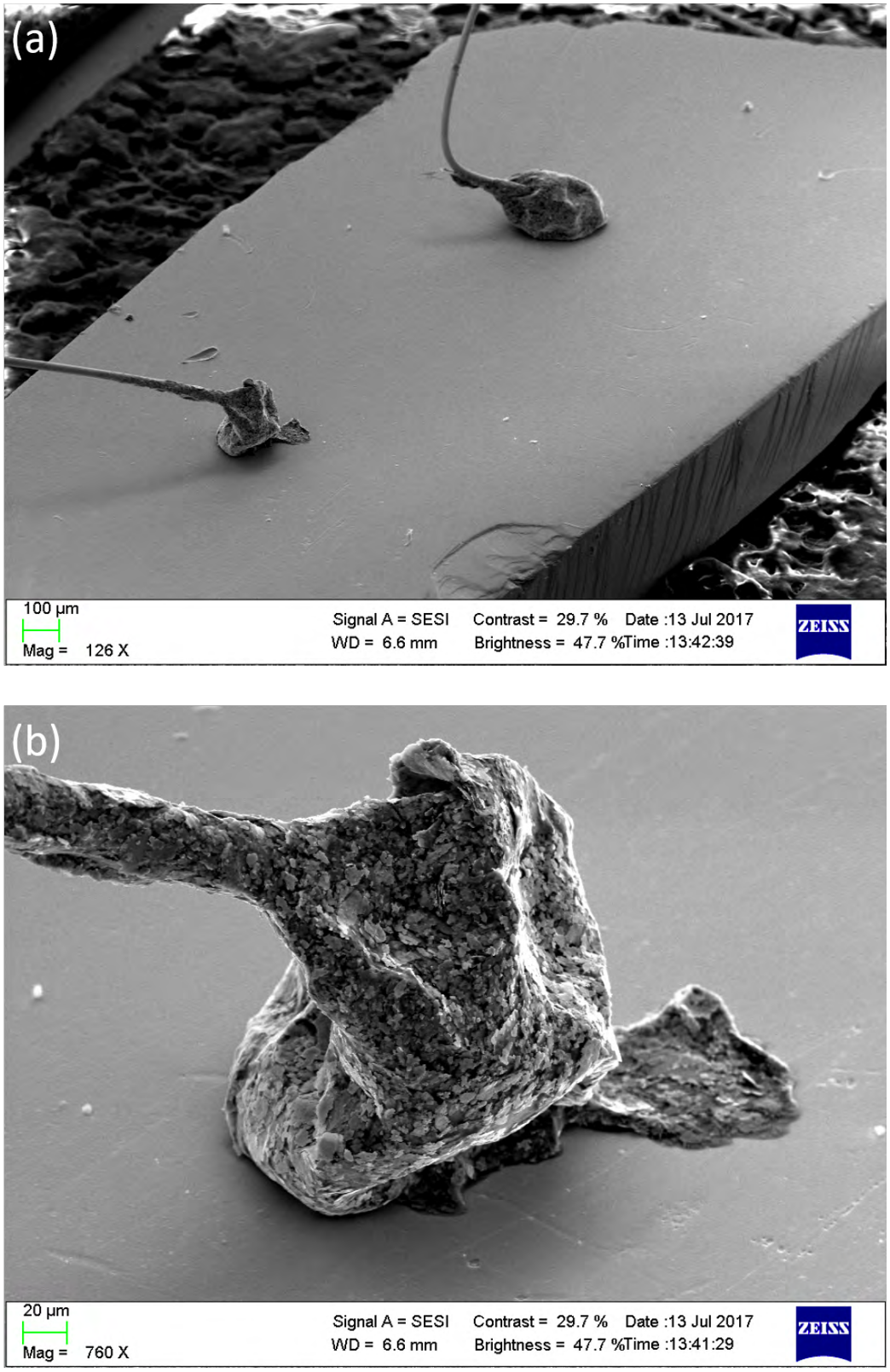

FIGURE 2.4: (a) Soft point contacts made on the surface of $Pb_{0.2}Sn_{0.8}Te$. (b) Zoomed contact area.

2.3 Cryogenic equipment

Transport measurements have been performed both in the pumped helium and dilution refrigerator systems. As the critical for the measurements was to achieve contact with sufficiently small size, it required aggressive fabrication of the samples with multiple point contacts. For that reason, I prepared a dedicated insert for the transport measurements to the SQUID Magnetometer. During my graduate course in the Laboratory of Cryogenic and Spintronic Research at IP PAS, I have fabricated two transport holders fitting the SQUID magnetometer.

Transport measurements in the QD MPMS have several advantages. First, it is straightforward to compare Curie temperature obtained by resistance and magnetization measurements. Second, QD MPMS offers unprecedented field and temperature stability. The cryostat was able to stabilize virtually any given temperature and achieve stability of ± 1 mK. A temperature sweep at a given rate is possible which is particularly helpful for fragile samples. The samples can be cooled down/warmed up in a steady way at the rate as low as 0.1 K/min. Among all the perks of this system, the only drawback is the lack of continuous magnetic field ramp. This has to be done exclusively in a discrete way, where the magnet power supply would increase the field in given steps. All in all, this is a minor disadvantage, when one take into account all the benefits. Another problem which had to be overcome before the measurements is interfacing QD MPMS with the data acquisition software. This is not straightforward as the manufacturer does not allow for an external control, or at least a readout of an actual system parameters via most common GPIB interface. In principle, QuantumDesign offers a way of communicating with the magnetometer, providing the libraries for Delphi language. However both the language and libraries are becoming obsolete, so we decided to pursue a different route. We communicate with all the necessary measurement electronics like Lock-in amplifiers or DC nanovoltmeters by standard VISA protocol using LabView or Python. The data from the SQUID (e.g. Temperature, Magnetic Field etc.) is being read on-line from the magnetometers log-file. User can specify how often log-file will be updated, typically we choose to update it every second. This results with a robust platform for the electron transport measurements.

The first holder was designed to fit the already existing system and was initially fabricated for gating of dilute magnetic semiconductors. In this configuration application of an in-plane magnetic field was straightforward, the current was applied parallel to the magnetic field direction. The setup was a convenient tool to study resistivity temperature dependence as well as in-plane magnetoresistance. However, Hall measurements and magnetoresistance in a perpendicular field couldn't be easily performed in this setup. The limiting factor is the small diameter of a sample space in the magnetometer which is about 9 mm. Although the insert and the sample holder had its limitations, we were able to use this platform also for the gating experiments. The results are described in the Ref. [129].

The convenience of using this platform was so appealing we decided to look for a solution which would allow measurements with magnetic field in an out-of-plane configuration. Such a solution was proposed by the researchers from Francis Bitter Magnet Lab at the Massachusetts Institute of Technology (MIT) and described in Review of Scientific Instruments [130]. QuantumDesign supplies a probe with 10 leads which can be used for gating or transport measurements. This probe however does not allow for convenient change of samples, and again it is designed for the in-plane magnetic field measurements. Another obstacle is that the probe wires are directly attached to the sample. Multiple resolderings can then lead to a malfunction of the wires. The MIT group attached a 10-pin circular transistor socket to the end of the probe. This allows for quick and convenient change of samples and permits measurements in the out-of plane configuration (see Figure 2.5). In addition to the design proposed in Ref. [130], we decided to additionally screen the cables coming out of the probe to reduce high-frequency noise.

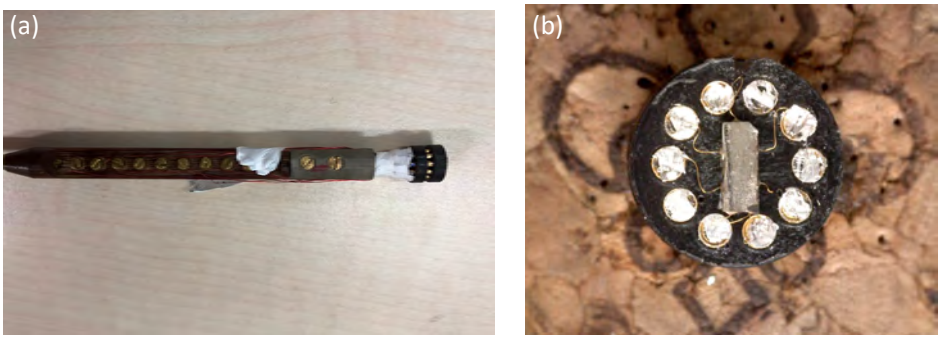

FIGURE 2.5: (a) Electrical transport probe compatible with QD MPMS XL magnetometer (b) Photo of a sample carrier with actual specimen in the Hall bar configuration.

2.3.1 Dilution refrigerator

Point contact spectroscopy is usually applied to study properties of superconductors. Some elemental superconductors, like Ti have a transition temperature below 1K. This is beyond capabilities of pumped helium cryostats, which usually provide temperature about 1.5 K. Only the most optimized systems with very efficient pumps can achieve 1 K which is a limit of this technique. Achieving temperatures below 1 K is usually being done by utilizing dilution refrigerator. Since dilution refrigerators are being used in condensed matter physics for over 50 years, I will only briefly outline the operating principle. The standard reference text on refrigeration techniques below 1 K was written by Lounasmaa [131]. All the milikelvin measurements done in this thesis were performed in the Oxford Insturments Triton Dilution refrigerator which allows measurements down to 10 mK. It was also equipped with a vector magnet with 6 T out of plane magnetic field, and 1 T for x and y components of the in-plane field. The enormous advantage of this system

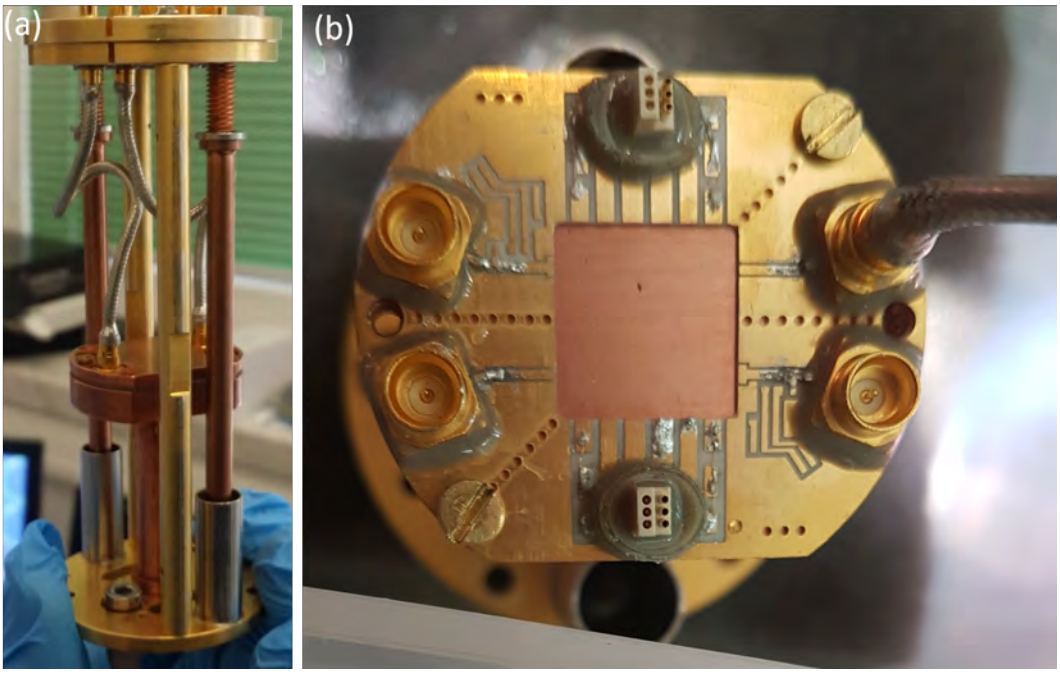

FIGURE 2.6: Sample puck used in Oxford Triton Dilution Refrigerator. Panel (a) depicts side view of the puck with the sample holder prepared for microwave measurements. (b) Top view of sample carrier with 12 DC lines and 4 SMA connectors for radio frequency measurements.

is its modern cryogenic design. Historically, the first stage of reaching temperatures close to the absolute zero was achieved using cryogenic liquids. First, the vacuum jacket and the magnet had to be pre-cooled with the liquid

nitrogen and then with liquid helium. Then the insert with the refrigerator is immersed in pumped helium bath with the temperature below 2 K. In the case of cryogen-free dilution refrigerator, instead of using low-temperature liquids a continuous cycle of compressions and expansions of helium is used to cool down the system to approximately 4K. Below 800 mK mixture of He^3 and He^4 separate into two phases. One phase contains both He^4 and He^3 with approximately 6 % of the latter, the second phase is composed of pure He^3. Obviously, the pure, lighter isotope comes on top of the mixture. He^4 is a superfluid below 2.16 K and consequently forms a Bose-Einstein condensate. The He^3 on the other hand, obeys Fermi-Dirac statistics. For that reason, there is no interaction between the helium isotopes in the mixture. As enthalpy of He^3 differs in two phases, diffusion from the dense to dilute phase cools the environment. This is analogous to the evaporative cooling of He^4 technique commonly used for achieving temperature below 4.2 K, where Helium particles in a gaseous phase are pumped away from the Helium bath. In the case of standard "wet" dilution refrigerator, gaseous He^3 is again compressed and returned to the mixing chamber. For the "dry" systems, however, the He^3 expands in the Joule-Thomson process and thus re-liquefies. Although we don't need liquid helium anymore, pulse tubes require a large amount of electrical energy to operate. Also, cooling down from the room temperature can take a considerable amount of time, 50 hours in the case of system, I worked with. However, the fridge was equipped with so-called bottom loader, which allows for a rather fast sample exchange. Before the transfer, He^3-He^4 mixture is collected to the tank, and the system is warmed up to approximately 15 K. Then the sample puck could be unscrewed from mixing chamber dock and thermalize in the load-lock. Once it reaches a temperature above 0^o C, it could be taken to the ambient conditions and exchange with the other sample puck. After re-loading cooldown to the base temperature takes approximately 8 hours. Oxford Instruments designed a sample puck fitting docking port which is thermally anchored at the mixing chamber. The sample mounting is left to the user. Our Dilution refrigerator was set-up by Dr. Maciej Zgirski shortly before, I started my graduate studies. He designed suitable PCB sample carriers which, I later fabricated and accustomed to suit my measurements. Example of the sample puck and sample carrier with the PCB is shown in the Fig 2.6. Thanks to relatively big sample space, multiple samples or devices can be measured in a single cooling cycle.

2.3.2 Contacting the samples

IV-VI semiconductors although known and studied for many years are not being contacted straightforwardly. Indium is most commonly used to make electrical contacts to many semiconducting materials. First, indium doesn't alloy with widely used golden wire contrary to tin which is known to alloy with gold. Second, indium is very mobile and easily diffuses into almost any material. Despite this advantages, using indium as a contacting material can source many experimental troubles. Grabecki et al. [132], shown that indium contacted PbTe exhibits unexpected superconductivity, which critical field and temperature do not match that of pure indium. Indium immediately

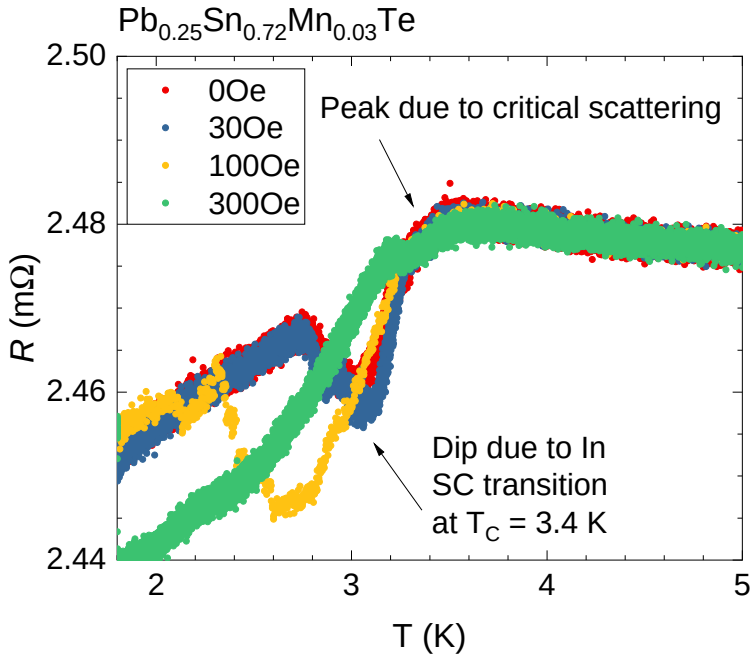

FIGURE 2.7: Four-probe measurements of low temperature resistance if In contacted $Pb_{0.25}Sn_{0.72}Mn_{0.03}Te$ showing low-field resistance anomalies.

alloys with PbTe and forms vairous type of indium-lead-tellurides which can be superconducting. Also, indium contacts will lead to unusual low-magnetic field magnetoresistance anomalies, which are not observed in the case of non-superconducting contacts. For that reason we decided to abandon indium completely in our studies to avoid any experimental artifacts. A various types of silver paint/paste are common alternative to Indium. Unfortunately, for the case of IV-VI semiconductors silver paint forms a contact which may exceed resistance of indium contact more than order of magnitude. We solved this problem by using a technique known as spot-welding. The resulting contact consists of a molten material and golden wire alloyed

to form low-resistance contact. The resistance of the contact is comparable to the contacts made of indium. However, these contacts tend to break when used in high magnetic fields and carrying high current. Typically, 10 mA and 3 T is sufficient to pull out the contact. For measurements in this conditions contacts should be strengthen by covering the contact area with silver epoxy.

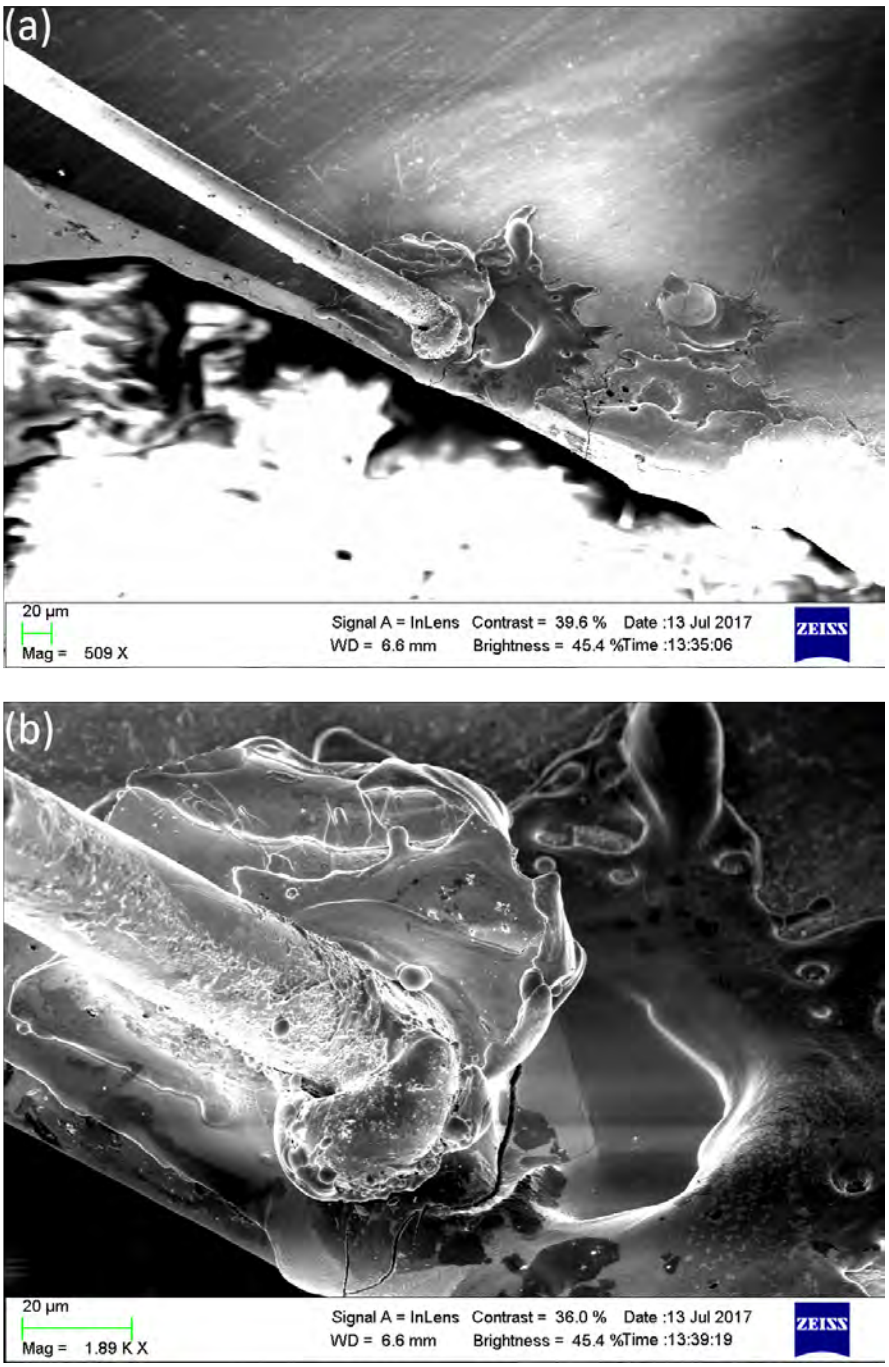

FIGURE 2.8: (a) SEM photograph (b) zoom of contacts welded to $Pb_{0.2}Sn_{0.8}Te$.

2.3.3 Differential resistance measurements protocol

Transport measurement performed throughout the thesis were performed through 4-probe technique. To avoid parasitic thermal voltages, we used either standard lock-in technique or alternating DC modulation depending on the needs. Very often, the first experimental problem is how to feed a sufficiently high current to low resistance sample? Modern lock-in amplifiers have high-quality digital voltage source, synchronized with the nanovoltmeter. It can be conveniently transformed to a current source by placing the in-series resistor. Most commonly, such built-in sources can generate voltages of the order of several volts (5 V on average), with output impedances of the order of several ohms. This means, that generating currents higher than 1 mA becomes less convenient. For that reason, we used an AC/DC current source (Keithley 6221) able to generate an arbitrary waveform, pulses and DC current with amplitude up to 105 mA (peak to peak). It can also provide a frequency and phase reference for the lock-in amplifier, being a handy tool for studying very-low resistance samples.

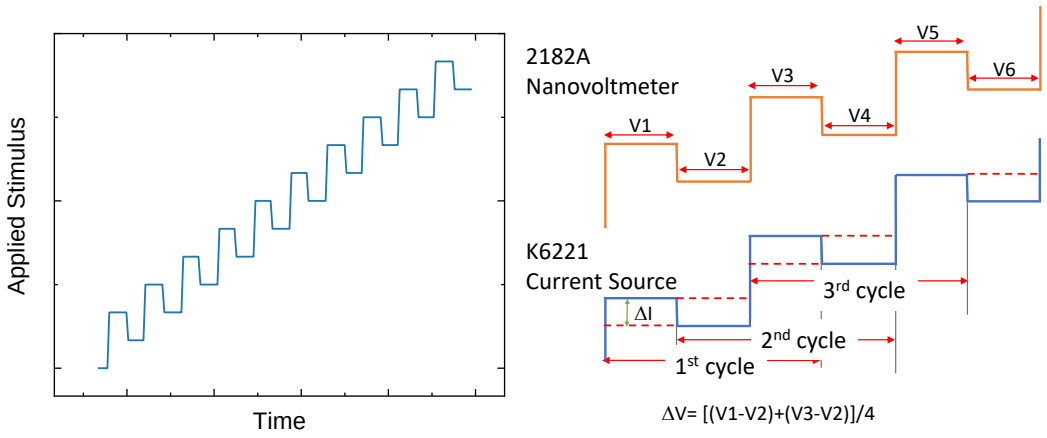

FIGURE 2.9: (a) Current waveform applied to the device using Keithley 6221 current source (b) Measurement details.

Studying differential resistance is usually more complex, as it requires coupling of DC bias and small modulating AC component. However, current source described above can be coupled to a nanovoltmeter (Keithley 2182A) which allows this type of measurements when the two are working in a common mode. The difference between using lock-in amplifier and the current source, is that instead of sine-wave imposed on the DC bias, it imposes a square-wave with amplitude defined by the user. The illustration of this is

presented in the Fig. 2.9. This way setup simultaneously measures I-V and dV/dI. Direct measurement of differential resistance, significantly reduces time necessary for the measurements. Naturally, the I-V curves can be further differentiated numerically, however, for the case of small signals, usually a series of measurements is necessary to reduce the noise (which scales as $\sqrt{N}$ where N is a number of measurements). The differential voltage obtained in this method is calculated by

$$dV_1 = \frac{(V1 - V2) + (V3 - V2)}{4} \times (-1)^0 \tag{2.6}$$

$$dV_2 = \frac{(V2 - V3) + (V4 - V3)}{4} \times (-1)^1 \tag{2.7}$$

$$dV_3 = \frac{(V4 - V3) + (V5 - V4)}{4} \times (-1)^2 ... \tag{2.8}$$

As the modulation current amplitude dI is set constant during entire measurement, it is quite straightforward to calculate differential resistance ($dR = dV/dI$) and conductance ($dG = dI/dV$). Thus measurements of the derivative help to save time and increase signal to noise ratio. Additionally the setup is also capable of generating current pulses as short as 50 μs. As it will be discussed in Chapter 4, the current pulses can be used to modify point contact resistance [126].

Chapter 3

Characterization of the samples

3.1 Synthesis of $Pb_{1-y}Sn_yTe$ crystals

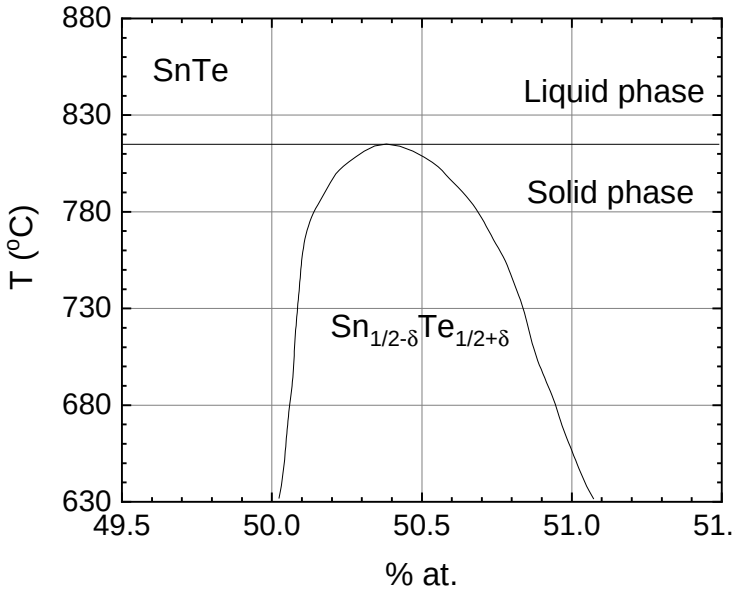

FIGURE 3.1: Temperature vs composition phase diagram of SnTe. Reproduced from the data published in Ref.[133]

Synthesizing high-quality monocrystals of ternary semiconductors can be extremely difficult. Several methods have been developed over the years to achieve this goal. Szczerbakow and Durose [134] proposed a method called *self-selecting vapour growth* (SSVG), which distinct feature is utilizing a polycrystalline source the seed. It can be applied to materials with substantial vapor pressure, making it an ideal choice for IV-VI alloys, though it was also used to obtain group II chalcogenides as well. Transport inside the ampoule is driven by the small temperature gradient (usually smaller than 10 K, however it can be as small as 2 K). Once the polycrystalline source is put inside the gradient, material from its hotter part recrystallizes at the cooler end of

the seed. During the growth, material favors the fastest growing orientations, leading to selective development of many highly oriented grains. Their size increases with time and finally lead to the formation of a single crystal. As pointed out by the authors of this method, the growth is "free from the walls", so crystal is free from mechanical stress to a large extent. Because the growth takes place in very small temperature gradient, crystals obtained via this method show remarkable compositional uniformity, as high temperature gradient usually drives distillation-like separation. The principle of growth and furnace temperature profile is shown in the Fig 3.3. Interestingly for $Pb_{1-y}Sn_ySe$ alloys, this method also allows controlling deviations from stoichiometry and consequently leads to n-type conductivity. This method of crystal growth allowed for deep exploration of topological phase diagram of TCI states in $Pb_{1-y}Sn_ySe$.

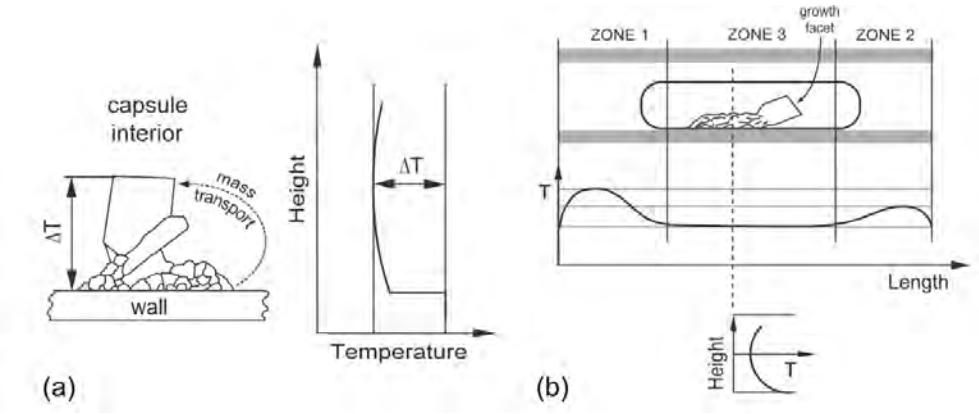

FIGURE 3.2: An illustration of the self selective vapor growth method. (a) Schematic depiction of the growth process and temperature profile. (b) Realistic depiction of the growth conditions. Reprinted with permission from the Ref. [134]

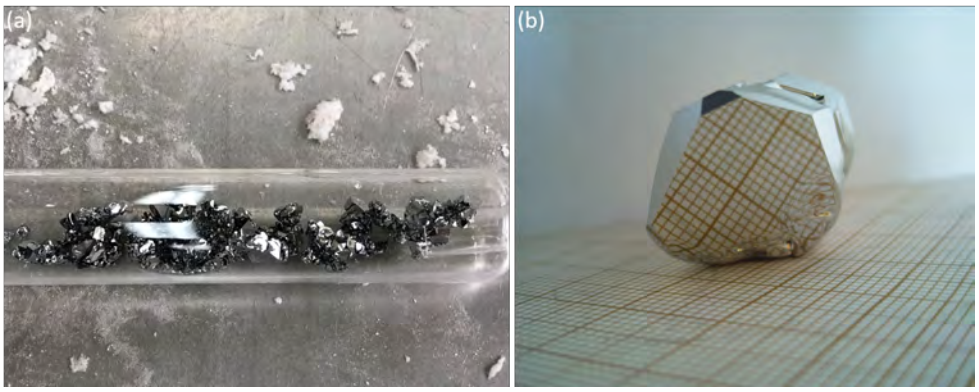

FIGURE 3.3: (a) Photograph of polycrystalline seed before SSVG inside the quartz ampule. (b) As-grown SnTe crystal with (100) and (111) facets.

3.2 Synthesis of $Pb_{1-y}Sn_yMn_xTe$ crystals

Neither the exact phase diagram for $Pb_{1-y}Sn_yMn_xTe$ nor for $Sn_{1-x}Mn_xTe$ was reported so far. Thus, the growing conditions for these crystals have to be estimated from the phase diagram for SnTe, shown in the Fig 3.1. Despite some reports of very high Mn doping level such as single crystals containing up to 19% Mn [135], or polycrystalline samples with 40% Mn [136], the results have not been reproduced. Instead the solubility limit was found to be ∼15 % [97]. Due to low vapor pressure of Mn the growth of magnetic crystals requires the application of the Bridgman method. Polycrystals of PbTe, SnTe and MnTe were pre-weighted in the desired ratio, and loaded into a quartz ampoule. The pumped ampoule was then placed in a hot area of the furnace. Growth temperature was necessarily higher than melting temperature of substrate compounds and obviously lower than quartz melting temperature T_m= 1180 ^oC. All the crystals investigated in this thesis were grown by dr hab. Andrzej Szczerbakow and MSc. Eng. Jędrzej Korczak of IP PAS.

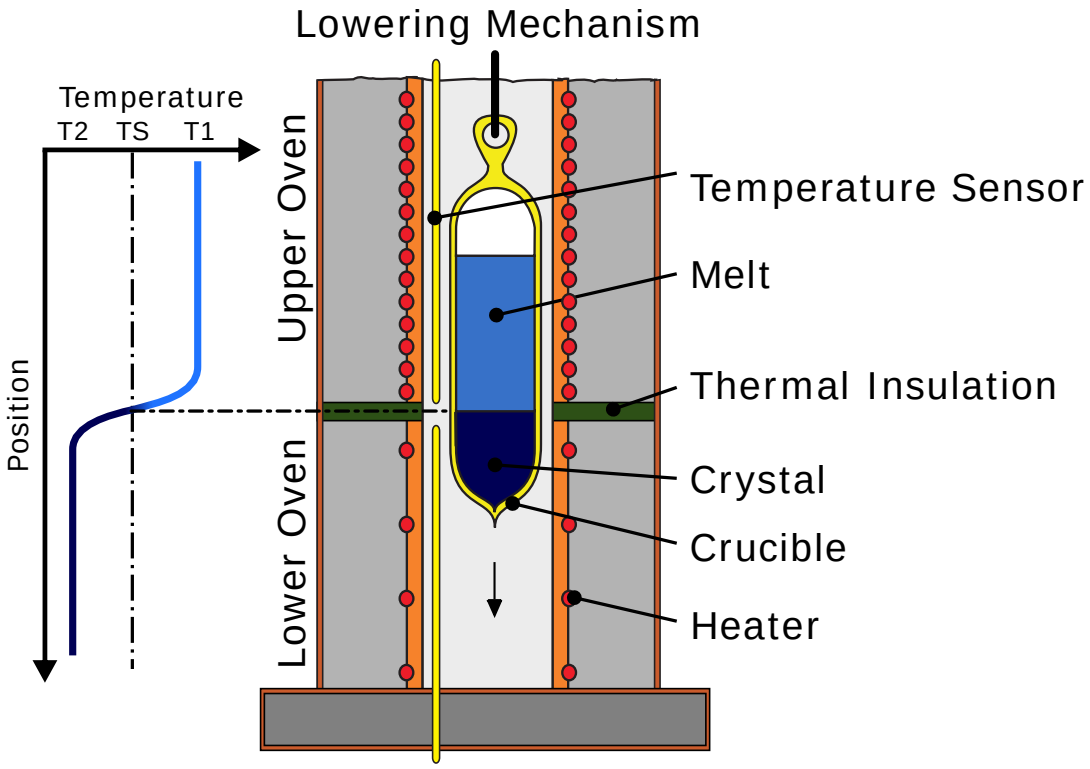

FIGURE 3.4: Schematic illustration of Bridgeman growing technique. Source: https://commons.wikimedia.org/wiki/File:Bridgman-Stockbarger-Verfahren.svg

3.3 Structural characterization

Crystallographic quality of the samples has been assessed by high-resolution X-ray diffraction (HR-XRD) and powder diffraction. The ω, $2\theta/\omega$ scans and reciprocal space maps (RSM) have been collected for reflection 444 (SnTe and $Pb_{0.16}Sn_{0.74}Mn_{0.10}Te$) and 006 ($Pb_{0.20}Sn_{0.80}Te$). The high-resolution X-ray diffraction measurements were performed by Dr J. Domagala. The powder diffraction and Rietveld analysis is a courtesy of Dr. R. Minikayev.

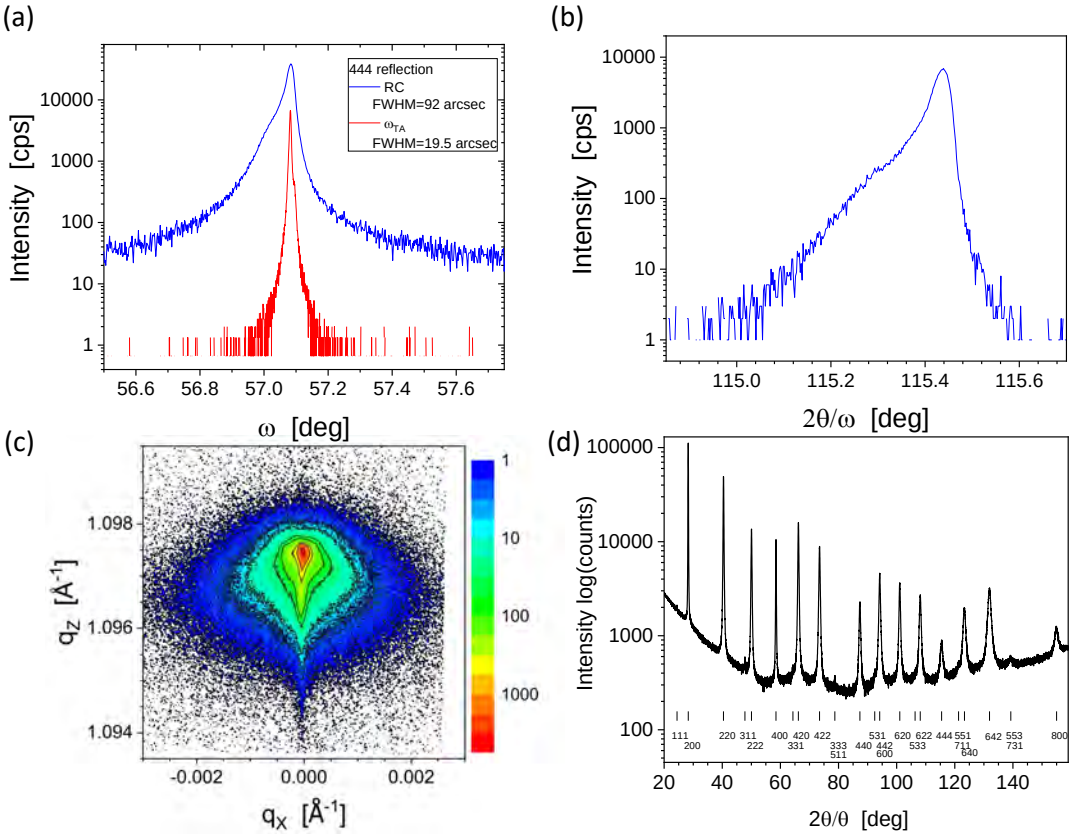

FIGURE 3.5: SnTe, reflection 444; 1x1 mm^2 - sample reflected X–ray beam size. (a) High Resolution X–ray diffraction ω -scan measurements. Upper curve - RC, lower - ω_{TA} -scan. (b) High Resolution $2\theta/\omega$ scan. (c) Reciprocal Space Map (RSM). The logarithmic scale was used, intensity is shown in counts per second [cps]. (d) Powder diffraction patterns of SnTe. The vertical bars indicate positions of Bragg peaks.

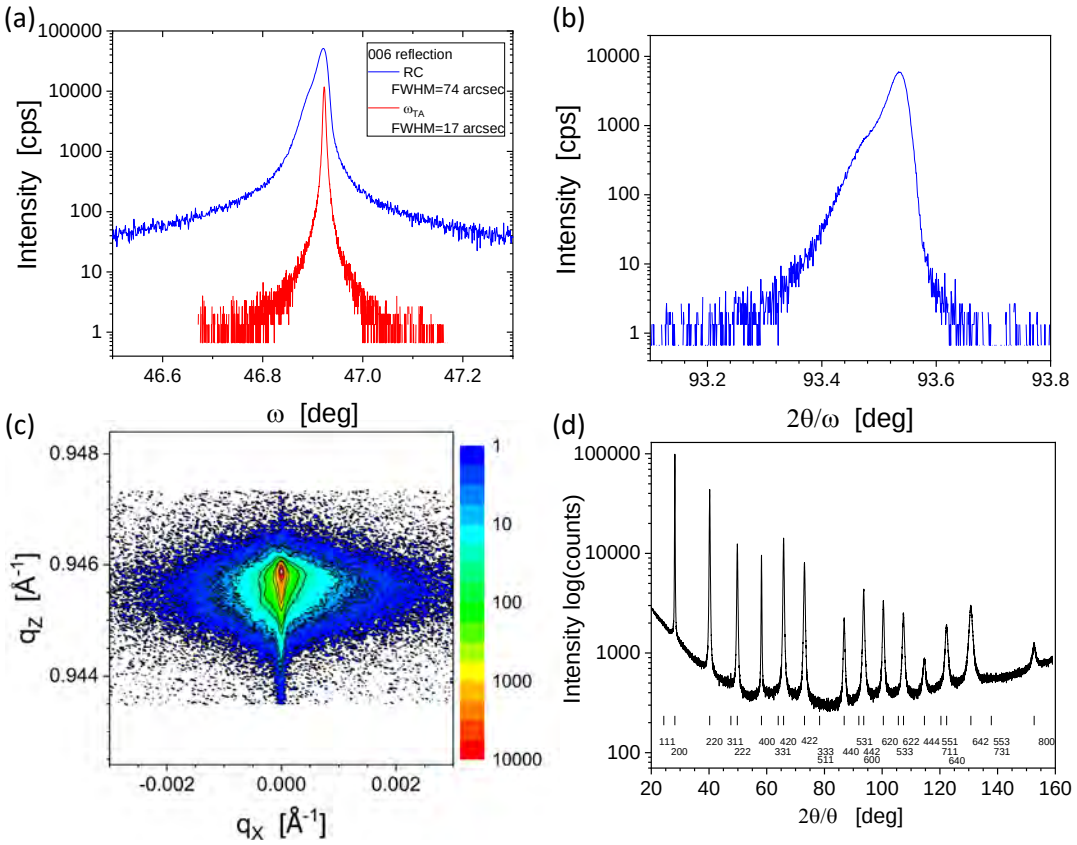

FIGURE 3.6: $Pb_{0.2}Sn_{0.8}Te$, reflection 006; 1x1 mm^2 – sample reflected X–ray beam size. (a) High Resolution X-ray diffraction ω -scan measurements. Upper curve - RC, lower - ω_{TA} -scan. (b) High Resolution $2\theta/\omega$ scan. (c) Reciprocal Space Map (RSM). The logarithmic scale was used, intensity is shown in counts per second [cps]. (d) Powder diffraction patterns of $Pb_{0.2}Sn_{0.8}Te$. The vertical bars indicate positions of Bragg peaks.

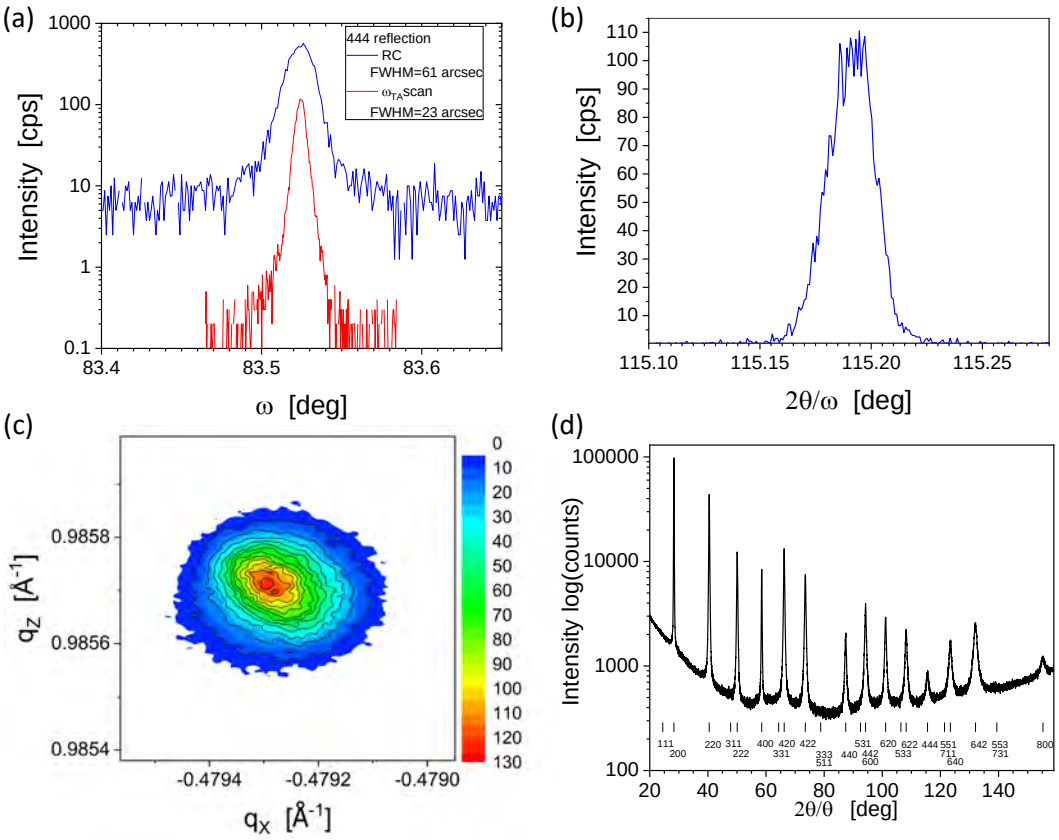

FIGURE 3.7: $Pb_{0.16}Sn_{0.74}Mn_{0.10}Te$, reflection 444; 0.5x0.1 mm^2 - sample reflected X–ray beam size. (a) High Resolution X-ray diffraction ω -scan measurements. Upper curve - RC, lower - ω_{TA} -scan. (b) High Resolution $2\theta/\omega$ scan. (c) Reciprocal Space Map (RSM). Intensity is shown in counts per second [cps]. (d) Powder diffraction patterns of $Pb_{0.16}Sn_{0.74}Mn_{0.10}Te$. The vertical bars indicate positions of Bragg peaks.

Sample	a (Å)
$Pb_{0.20}Sn_{0.80}Te$	6.3426(3)
SnTe	6.3129(3)
$Pb_{0.16}Sn_{0.74}Mn_{0.10}Te$	6.3098(5)

TABLE 3.1: Lattice parameters of investigated samples.

The results of the state-of-the art HR-XRD examination of the crystal structure of SnTe, $Pb_{0.2}Sn_{0.8}Te$ and $Pb_{0.16}Sn_{0.74}Mn_{0.10}Te$ are summarized in Figs. 3.5, 3.6 and 3.7, respectively. For the crystals of SnTe and $Pb_{0.2}Sn_{0.8}Te$ grown by the SSVG method one finds very sharp diffraction peaks fully accounted for by a single-rock salt crystal phase. The application of various XRD geometries (as indicated in Figs. 3.5,3.6) permitted the determination of the RC width parameters of 92 and 74 arcsec for SnTe and $Pb_{0.2}Sn_{0.8}Te$, respectively. After correcting for diffraction peaks asymmetry and background contribution due to diffusive scattering by native defects (vacancies) present in the crystals we could also evaluate the crystal perfection of (111) and (001) planes as given by the RC width parameter 17-19.5 arcsec. One may notice that these are the XRD parameters comparable to standard GaAs (001) crystals. In the case of $Pb_{0.16}Sn_{0.74}Mn_{0.10}Te$ - the planes (111) were inclined at the angle of 25° to the surface, so that 444 was asymmetrical (the X–ray beam geometry at a high angle to the sample was used). The $Pb_{0.16}Sn_{0.74}Mn_{0.10}Te$ sample consists of misoriented $0.5 \times 0.1\,mm^2$ single crystalline grains. The mean grain deviation angle is estimated to be $0.06^o \pm 0.02^o$. For an X–ray beam limited by a mask and slit of such dimensions, a diffraction pattern was obtained as for a single crystal (Fig. 3.7).

Phase identification was carried out on the basis of patterns shown at the Figs. 3.5(d), 3.6(d), 3.7(d). Excellent statistics, peak-to-background ratio is 74, and broad angular range of measurement ($2\theta^o$ to 159^o) and all visible peaks identified as structural for rock salt crystals (Fm3-m). There is no indication of secondary phase present in investigated crystals. The measured lattice parameters are given in the Table 2.

3.4 Electrical Characterization

Before performing an actual conductance spectroscopy, the electrical properties of the samples were carefully examined. The main samples investigated in the point contact spectroscopy are listed in the table below. It consists of single crystals of rock salt $Pb_{1-y}Sn_yTe$ and $Pb_{1-y-x}Sn_yMn_xTe$ obtained via

the self-selecting vapour growth method and the Bridgman technique, respectively, as described in the beginning of this chapter. Since the TCI phase occurs for a sufficiently high Sn content, $y \gtrsim 0.30$ (ref. [66]), the studied samples of $Pb_{1-y}Sn_yTe$ cover both the topologically trivial and non-trivial cases (see Table 3.2). Room temperature charge densities and Hall mobilities are given in the table below.

Sample	$p\,(\mathrm{cm}^{-3})$	$\mu\,(\mathrm{cm}^2/\mathrm{Vs})$
PbTe	5×10^{18}	970
$Pb_{0.80}Sn_{0.20}Te$	4.9×10^{19}	280
$Pb_{0.20}Sn_{0.80}Te$	7.5×10^{20}	80
SnTe	3×10^{20}	350
$Pb_{0.30}Sn_{0.67}Mn_{0.03}Te$	2.6×10^{20}	110
$Pb_{0.16}Sn_{0.74}Mn_{0.10}Te$	1.4×10^{21}	180

TABLE 3.2: Chemical composition, hole concentration and mobility from room temperature Hall measurements of the investigated samples.

As expected for tellurium based IV-IV compounds all the specimens are strongly p-doped, with relatively low mobility. Hall measurements were performed using the standard 4-probe AC technique in the Hall-bar configuration (see Fig 1.1). In the case of diamagnetic crystals grown by the SSVG method, samples with approximate dimensions of $0.5 \times 1 \times 4\,\mathrm{mm}^3$ were cleaved from the single crystals. The Mn-doped samples are oriented by using an X-ray diffractometer equipped with a goniometer and cut by a wire saw to the form of rectangular parallelepiped with dimensions similar to the diamagnetic specimens. As expected for IV-VI semiconductors resistance of all investigated samples exhibits metallic behaviour as a function of temperature. An example of such behavior is shown in the Fig 3.8(a,b) for $Pb_{0.20}Sn_{0.80}Te$ and $Pb_{0.30}Sn_{0.67}Mn_{0.03}Te$. For Mn-doped samples a increase of resistivity close to the Curie temperature is seen, which is a common feature for every conducting magnet [104]. Interesitngly $Pb_{0.16}Sn_{0.74}Mn_{0.10}Te$ exhibits sharp peak of the resistance precisely at the Curie temperature. This feature was observed before by Escorne and Mauger [137] for $Sn_{1-x}Mn_xTe$ and was interpreted in terms of a resonant scattering on a virtual bound level. A better developed peak was observed by the authors for moderate Mn doping i.e. x=0.054 and hole density $5.4\times 10^{20}\,\mathrm{cm}^{-3}$ at temperatures slightly below T_{Curie}. Thanks to the experimental setup described in the previous chapter, I was able to perform magnetic and transport measurement using the

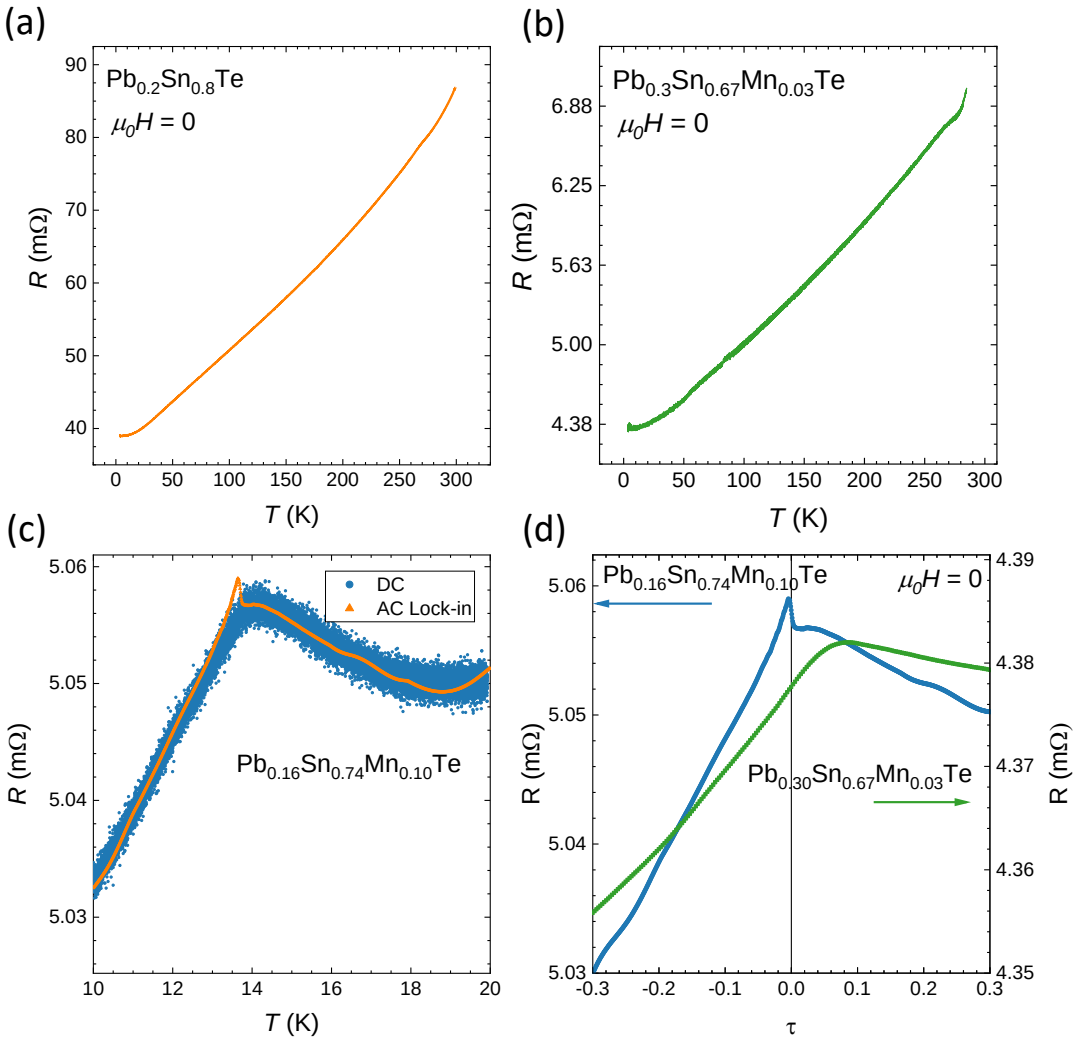

FIGURE 3.8: Metallic behavior of resistivity measured for $Pb_{0.20}Sn_{0.80}Te$ (a) and $Pb_{0.30}Sn_{0.67}Mn_{0.03}Te$ (b). (c) Comparison between AC and DC resistance measurements for $Pb_{0.16}Sn_{0.74}Mn_{0.10}Te$ in the vicinity of the Curie point. (d) Low temperature resistance of ferromagnetic samples as a function of reduced temperature $\tau = 1 - T/T_{\text{Curie}}$.

same cryostat, which guarantees nearly-perfect accuracy in terms of estimating transition both from magnetic and resistance measurements. Interestingly, these combined measurements shown that the peak occurs exactly at the Curie temperature, its intensity scales with current applied to the sample and vanishes for magnetic field smaller than 1 mT. Indeed, peak got considerably broader and moved below T_{Curie} for currents higher than 5 mA. Although resistance of the sample counts only few miliohms, contact resistance is typically twenty times higher, which leads to considerable Joule heating at high current excitations. Surprisingly this peak reveals itself only in AC

measurements with the use of a lock-in amplifier, and its completely absent for the DC counterpart. This suggests that the peak may originate due to non-linear phenomena, like strong scattering on magnetic domains. Similarly to the first report on this regard [137] we do not observe such a peak for x=0.03 sample. To shed more light on this interesting result the collaboration with Prof. Joachim Kusz from University of Silesia was established. Thanks to this collaboration temperature dependence of a lattice parameter down to 10 K was measured.

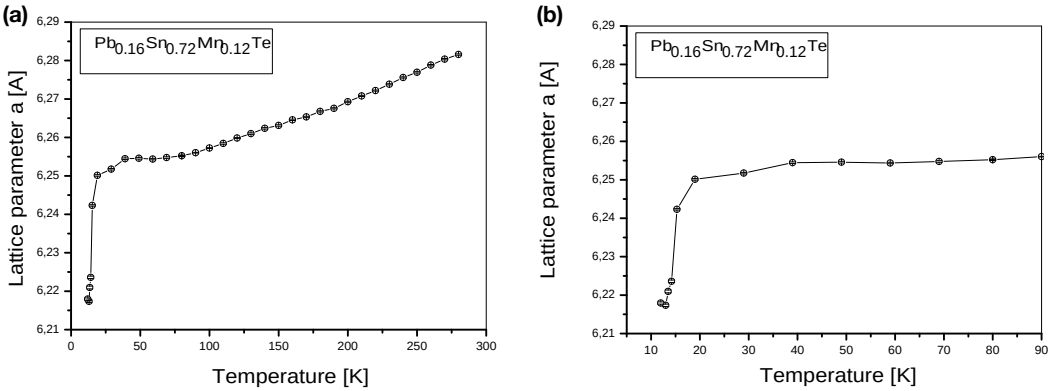

FIGURE 3.9: (a) Dependence of a lattice parameter measured for $Pb_{0.16}Sn_{0.72}Mn_{0.12}Te$ in the broad temperature range. (b) Zoom on the low-temperature region, a clear reduction of lattice constant is seen in the vicinity of T_{Curie}.

This measurements revealed that in the vicinity of ferromagnetic phase transition lattice parameter changes by approximately 0.5 %. Hypothetically such a big change of lattice parameter could be a result of first order phase transition [138]. First order phase transitions are accompanied by latent heat which consequently leads to a hysteretic behavior in the transitions vicinity. A series of measurements with different experimental technique (AC and DC magnetization, resistivity) didn't reveal any measurable hysteretic behavior. A better understanding could be achieved by further examination of samples with different material parameters. However, for specimens with smaller hole density and manganese concentration, transition to the ferromagnetic phase occurs below 10 K which is the base temperature of the XRD setup used in this measurements. Alternatively one could measure thermal expansion coefficient by using capacitive dilatometers. These devices are becoming increasingly popular and may operate even at temperatures below 1 K [139]. A systematic analysis of lattice parameter change as a function of hole concentration and Mn doping is necessary to understand what drives this peculiar feature. We may speculate that the non-linearity at T_{Curie} detected in

the transport measurements may originate from a rapid change of the lattice parameter. Perhaps, direct imaging of magnetic domains in the presence of current together with the thermal expansion measurements could reveal physical mechanism behind observed behaviour. These findings point to a new and interesting direction in further investigations of Mn-doped IV-VI semiconductors.

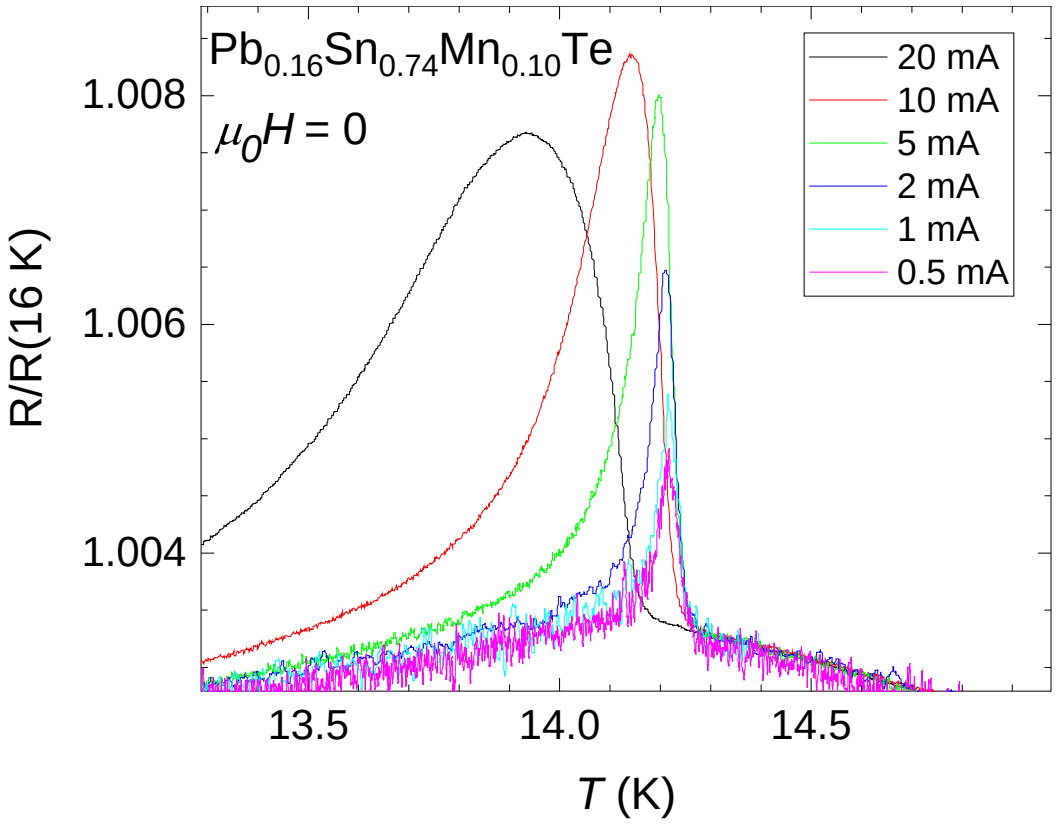

FIGURE 3.10: Dependence of the non-linearity at the Curie temperature measured as a function of the applied current.

3.5 Magnetic Characterization

Impact of stress on the investigated samples As IV-VI semiconductors are known to be structurally soft [140], first we address the problem of mounting the sample inside the magnetometer. Usually investigated specimens are glued with GE Varnish to 2 mm thick silicon strip as described in the Ref. [141]. Alternatively the sample may be placed between two plastic straws with no glue involved. As it can be seen in the Fig 3.11, the difference in measured magnetic moment is biggest in small magnetic fields, when sample is not fully magnetized (3.11(a)). However as the magnetic field increases Fig 3.11(b),(c), the difference between the two is smaller than 1% and does

not seem critical for further investigations. Importantly, origin of this difference does not necessarily need to come from stress, as the intrinsic responses of sample holder can differ.

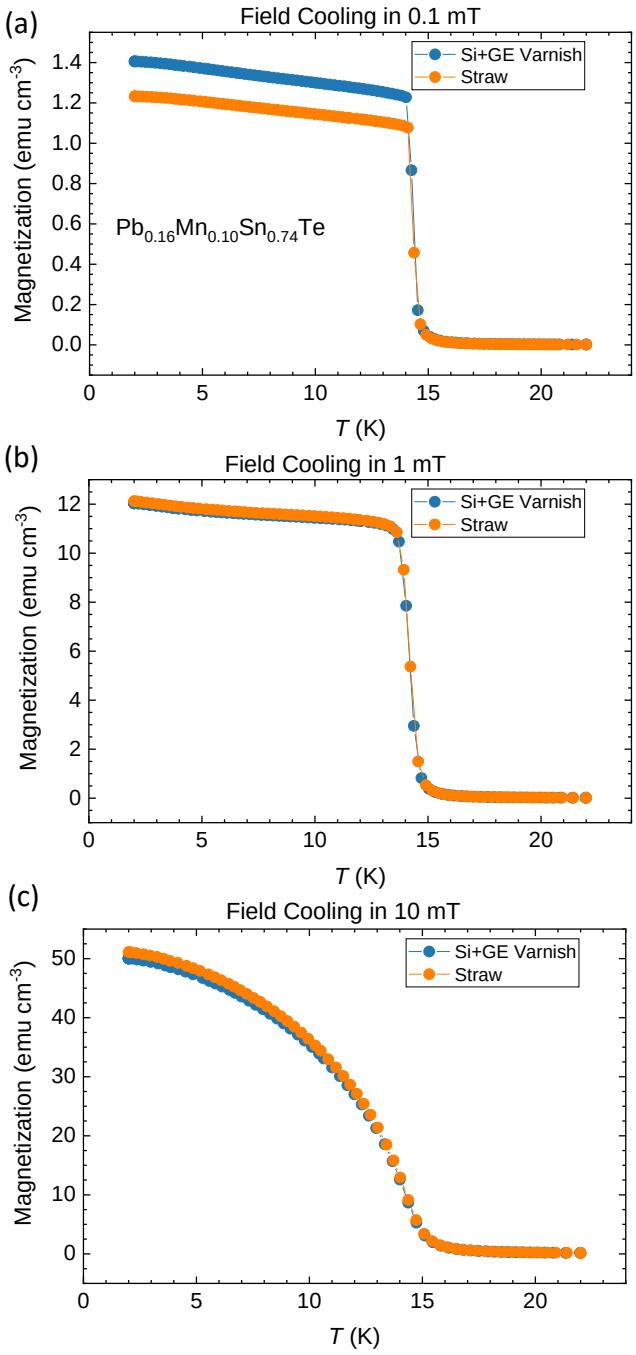

FIGURE 3.11: Impact of stress on the magnetic moment measured at 0.1(a),1(b),10(c) mT for $Pb_{0.16}Sn_{0.74}Mn_{0.10}Te$.

Curie-Weiss characterization The Curie-Weiss law can be used, to estimate the effective concentration of magnetic ions, once temperature dependence of susceptibility is known. It is given by the well known formula:

$$\chi(T) = \chi_d + \frac{C}{T-\theta}, \tag{3.1}$$

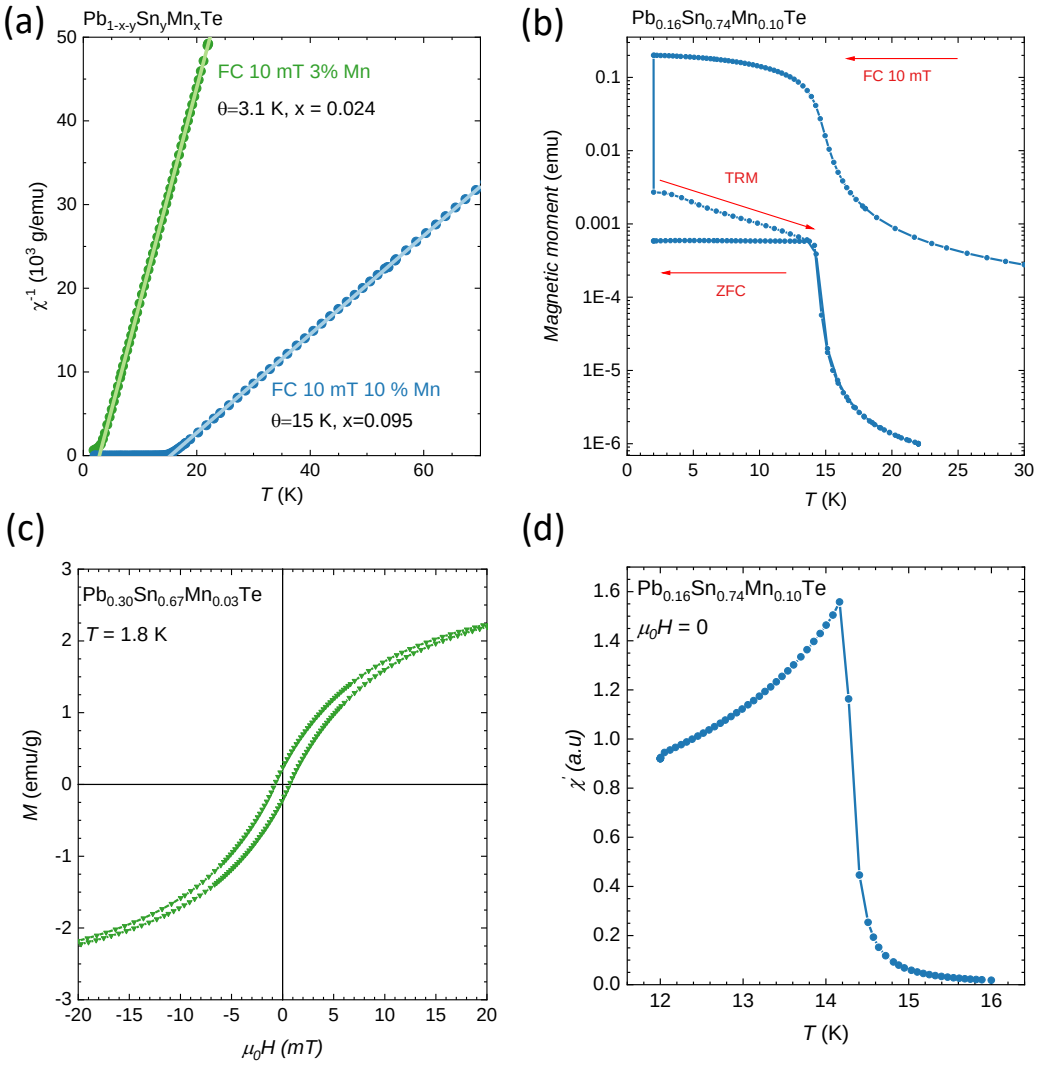

FIGURE 3.12: (a) Determination of the Curie-Weiss temperature for two ferromagnetic samples used in the further spectroscopic studies. Circles correspond to experimental data, pale lines are fit of the Curie-Weiss formula. Estimation of the Curie Temperature from magnetic measurements exemplified on the sample $Pb_{0.16}Sn_{0.74}Mn_{0.10}Te$. (c) Low-field M(H) characteristics of $Pb_{0.30}Sn_{0.67}Mn_{0.03}Te$. (d) $Pb_{0.16}Sn_{0.74}Mn_{0.10}Te$ example of differential susceptibility measurement used to confirm T_{Curie} evaluated from magnetization data.

where C=N_0S(S+1)g^2_{Mn} μ^2_B is a Curie constant, θ is a Curie-Weiss temperature, N_0 is the cation concentration, S equals to the spin of Mn ions (5/2) and g is Lande g factor, μ_B is Bohr magneton. χ_d equals to the magnetic susceptibility of $Pb_{1-x}Sn_yTe$ which weakly depends on temperature. Following previous report on this regard [122], the value of $\chi_d = -2.7 \times 10^{-7}$ g/emu was used. The values of $x_{eff} = 0.024$ and 0.095 are determined from the Curie constant obtained from our magnetic susceptibility measurements between 100 K and T_{Curie}. Nevertheless, throughout this thesis, I will be referring to the ferromagnetic samples using their technological Mn concentration, namely $x = 0.03$ and $x = 0.10$. According to the results of magnetization measurements collected in Fig. 3.13, non-magnetic compounds show field-independent diamagnetic susceptibility, enhanced by strong interband polarization in the inverted band structure case.

Determination of Curie Temperature The Mn-doped samples contain Sn concentration corresponding to the TCI phase and the hole density high enough to populate twelve Σ valleys (see Table 3.2). A large density of states (DOS) associated with these valleys makes hole-mediated exchange coupling between Mn ions sufficiently strong to drive the ferromagnetic ordering [118, 119]. The Curie temperature T_{Curie} which separates the paramagnetic and ferromagnetic phase, can be determined using variety of different methods. For example, it can be obtained from resistance measurements. For the case of $Ga_{1-x}Mn_xAs$, singularity in the temperature derivative of resistivity was used to accurately estimate the transition point as shown by Novak et. al [142]. Naturally, methods of magnetometry can be used for accurately determine T_{Curie} as well. One can use an AC magnetometer to look for the maximum of differential susceptibility in the vicinity of the transition, as seen in the Fig. 3.12(d). Alternatively Curie point can be estimated from spontaneous magnetization formation in a ferromagnet. Most frequently, a thermoremnant magnetization temperature dependence is utilized for this estimations. It is a remnant magnetic moment appearing after quenching magnetic field to zero after saturating the sample well below T_C[141]. This is best seen in the Fig 3.12. Initially the sample is cooled in the constant magnetic field of 10 mT. Below 2 K the field is quenched to zero, and thermoremanent moment is measured. In the case of IV-VI bases DMSs', the remanent magnetic moment is almost two order of magnitude smaller than saturation magnetization (Fig 3.12(b)), probably due to the formation of magnetic domains and weak cubic anisotropy. Indeed, $Pb_{1-x-y}Sn_yMn_xTe$ belongs to the family of so

called magnetically soft materials. These ferromagnets have very small coercivity(Fig 3.12(c)) and consequently material can be easily demagnetized. Similarly, once the sample is cooled again below T_{Curie}, a spontaneous magentic moment is formed, however its magnitude is even smaller as compared to its theromoremnant counterpart. Finally, an excellent agreement is observed between the T_{Curie} estimated from thermoremnant moment, differential susceptibility and resistivity for both ferromagnetic specimens. As shown in Fig. 3.13, the Curie temperature, is 2.7 K and 14 K for the Mn concentration $x = 0.03$ and 0.10, and the Sn content $y = 0.67$ and 0.74, respectively. According to the mean-field $p - d$ Zener model [104, 113]

$$T_{\mathrm{Curie}} = x_{\mathrm{eff}} N_0 S(S+1)\beta_{\mathrm{eff}}^2 \rho_{\mathrm{F}} / 12 k_{\mathrm{B}} - T_{\mathrm{AF}}, \tag{3.2}$$

where $x_{\mathrm{eff}} < x$ and $T_{\mathrm{AF}} > 0$ take into account the presence of short-range antiferromagnetic interactions, and N_0 is the cation concentration. Important effects of spin-orbit interactions, carrier-carrier correlation, and mixing between anion and cation wave functions are incorporated into an effective $p - d$ exchange integral β_{eff}. In order to evaluate its magnitude Mn spin $S = 5/2$ and DOS of holes at the Fermi level ρ_{F} from specific heat measurements for $Sn_{1-z}In_zTe$ with comparable hole densities [17] are assumed. $T_{\mathrm{AF}} = 8xS(S+1)\mathcal{J}$, where $\mathcal{J} \simeq 1$ K (ref. [143]). For the experimental magnitudes of T_{Curie} $N_0|\beta_{\mathrm{eff}}| = 0.25 \pm 0.02$ eV is obtained, a value at the upper bound of those determined for Mn-doped lead chalcogenides [144].

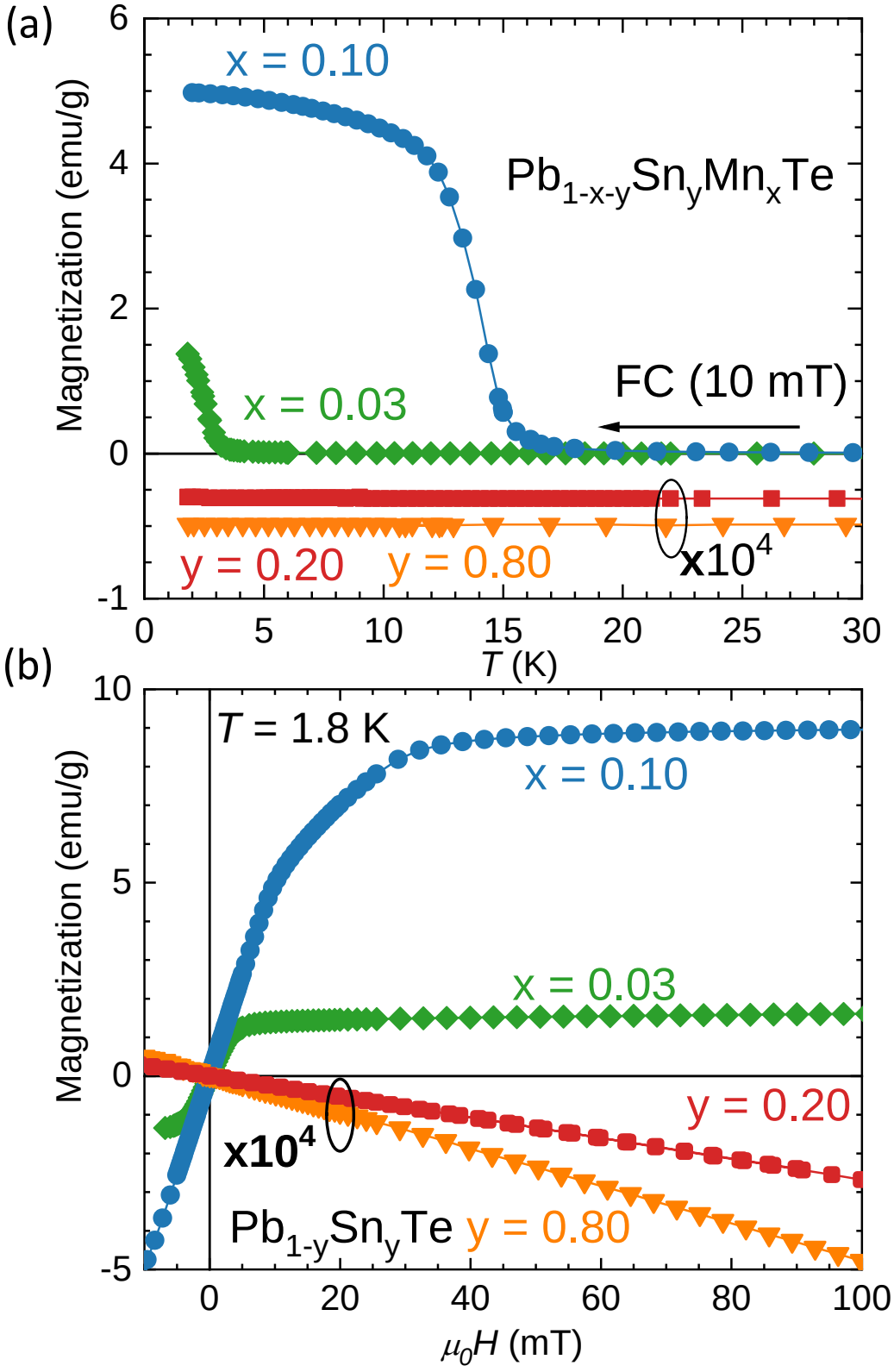

FIGURE 3.13: Magnetization as a function of temperature (a) and the magnetic field (b) of $Pb_{1-y-x}Sn_yMn_xTe$ with various Mn concentrations x and the Sn content y. The data show the presence of ferromagnetism at low temperatures in Mn-doped samples with the Curie temperature increasing with x. Without Mn doping the samples are diamagnetic – in order to visualize the diamagnetism magnitude, the magnetization values are multiplied by a factor of 10^4.

Chapter 4

Point contact spectroscopy on the TCI surface

This chapter is based on the preprint: G.P. Mazur, K Dybko, A Szczerbakow, M Zgirski, E Lusakowska, S Kret, J Korczak, T Story, M Sawicki, T Dietl. Experimental search for the origin of zero-energy modes in topological materials arXiv:1709.04000v2

As it was outlined in the introductory paragraph of this dissertation, a series of point-contact experiments has revealed the existence of superconducting point contacts at junctions of metal tips with topological semiconductors and semimetals [19–23, 25, 26, 29, 145]. Surprisingly, despite the absence of global superconductivity in these systems, the features in $\mathrm{d}I/\mathrm{d}V$ decay critically with temperature and the magnetic field as expected for a superconductor. It has, therefore, been concluded that the superconductivity results from tip-induced strain or from a dimensional confinement in the junction area. In the case of Cd_3As_2 this interpretation appears to be supported by the featureless spectrum in the case of a soft point-contact obtained using the silver paint [21, 23]. Surprisingly, however, the Andreev reflection-type spectra were recently reported for Au/Cd_3As_2 junctions without observation of the Meissner effect or 4 probe zero-resistance state [145]. Simultaneously soft-point contacts shown superconducting-like features for topological semimetals WC, $MoTe_2$ and WTe_2[25, 26, 29]. Now, as topological phase diagram for IV-VI based topological crystalline insulators (TCI) [61, 63–66] is one of the better explored and understood among all the topological materials, point-contact experiments can be performed for the same material class, however without topological surface states. Of course, as Fermi level position depends on the amount of tin concentration, the carrier density is much lower for Pb-rich specimens as compared to pure SnTe. The first observation of superconducting point contacts in IV-VI semiconductors have been performed for $Pb_{0.60}Sn_{0.40}Te$ by Das. et al. [19].In this study, hard point-contact

characteristics reveals zero-bias conductance peaks (ZBCP) [19]. Apparently, the authors could not explore spectroscopic regimes of transport through the contact due to intrinsic disorder in the sample.

4.1 Experimental results

4.1.1 Point contact spectroscopy on diamagnetic TCIs

Using high-quality single crystals, which characterization details were described in the previous chapter, I employ the soft point-contact method[12, 16, 124, 126], in which a 15 μm Au wire is fixed by a silver paint to a freshly etched (011) or cleaved surfaces (001) (see Fig 2.4). To reduce level of surface oxidation to minimum, prior to point-contact preparation the samples are etched in 3 % Bromide solution in HBr for 15 sec. As shown in Fig. 4.1, in the case of the diamagnetic TCI $Pb_{0.20}Sn_{0.80}Te$ at low temperatures and magnetic fields symmetric differential conductance characteristics consists of a broad maximum centered at $V = 0$ and two minima at higher biases. The magnitude of ZBCP varies from sample to sample but is typically about $50e^2/h$. This form and magnitude of $dI/dV(V)$ is virtually identical to that discovered in other unconventional superconductors like Sr_2RuO_4[8] and hyperdoped, superconducting topological insulators $Cu_xBi_2Se_3$[12] and $Sn_{1-z}In_zTe$[16] and assigned to MBS, as discussed in the introductory paragraphs. However, in the present case neither magnetic nor ultra-low current resistance measurements (see Figs. 3.13 and 4.1d, respectively) point to the presence of a macroscopic bulk or surface superconductivity. As presented in the Fig. 4.1a, $dI/dV(V)$ is featureless in the case of the topologically trivial materials PbTe and $Pb_{0.80}Sn_{0.20}Te$ (in the notation adapted here y = 0 and y=0.20). These findings are far reaching, as PbTe and $Pb_{0.80}Sn_{0.20}Te$ are topologically trivial systems[63, 64, 66], whereas SnTe and related compounds are archetypical topological crystalline insulators (TCI), in which mirror symmetry protects gapless Dirac cones at (100), (110), and (111) crystal surfaces[63–66]. Importantly, according to both angle-resolved photoemission[65, 146] and magnetotransport studies[84], these cones coexist with bulk states even for high bulk carrier densities specific to these systems. The energetic position of the surface-cone neutrality-points in respect to the Fermi level depends on the character of surface states and the degree of surface oxidation, the question under investigations now[147].

At the same time, there is a striking similarity of differential conductance

spectra for samples in the TCI phase presented here to those found in topological materials collected in the Table 1.1, in which also no global superconductivity has been found. It is, therefore, tempting to conclude that point contact spectra signalize the existence a new universal phenomenon, specific to topological matter. As for the shape of the spectrum it is important to discuss, in which transport regime point contact actually falls.

For the case of IV-VI crystals investigated here, most commonly observed spectrum has a shape of the zero-bias peak as shown in the Fig. 4.1(c). In the superconducting point contact phenomenology such spectra classify to the so called as a thermal regime[126]. In that case features from the Andreev reflection are thermally blurred and the dips symmetric about V=0 come from the critical current as first systematically shown by Sheet et al. [148]. As discussed in the chapter 2, all spectroscopic information is lost in this regime. At the opposite end, where the mean-free path is smaller than the area of the contact, the contact is in ballistic regime and momentum and energy information can be obtained from the measurement. As by definition energy dissipation is not expected in this regime, dips associated with heating effects should vanish for ballistic transport. Such spectra are depicted in the Figs.4.1(a) (y=0.8, orange trace) and 4.1(b). In this spectra, side maxima in $\mathrm{d}I/\mathrm{d}V$ correspond the DOS enlargement at the gap edges, and the zero-bias conductance peak *may* indicate presence of zero-energy states residing inside the conductance gap. The zero-bias conductance peak smoothly vanishes with temperature and magnetic field leaving a clear gap structure to vanish at higher fields/temperatures. It is important to mention that exploring different regimes of point contact transport is absolutely crucial for identifying absolute value of the gap and its anisotropy, however in the present case it is somewhat a second order effect. In the case of all spectra gathered here, it is not clear, why the junction between normal metal and topological material resembles features routinely observed for metal/superconductor junction. Furthermore, as detailed in the next section, by employing high-resolution SQUID measurements I have undertaken search for superconductivity, either intrinsic or caused by, for instance, Pb or Sn precipitates. No evidence for the Meissner effect is found in the case of samples of interest here, i.e., $Pb_{1-y}Sn_yTe$ with $y = 0.20$, 0.80, and 1. This means, taking our experimental resolution into account, that the relative content of precipitations that could produce a response specific to superconducting Pb or Sn is below 0.1 ppm.

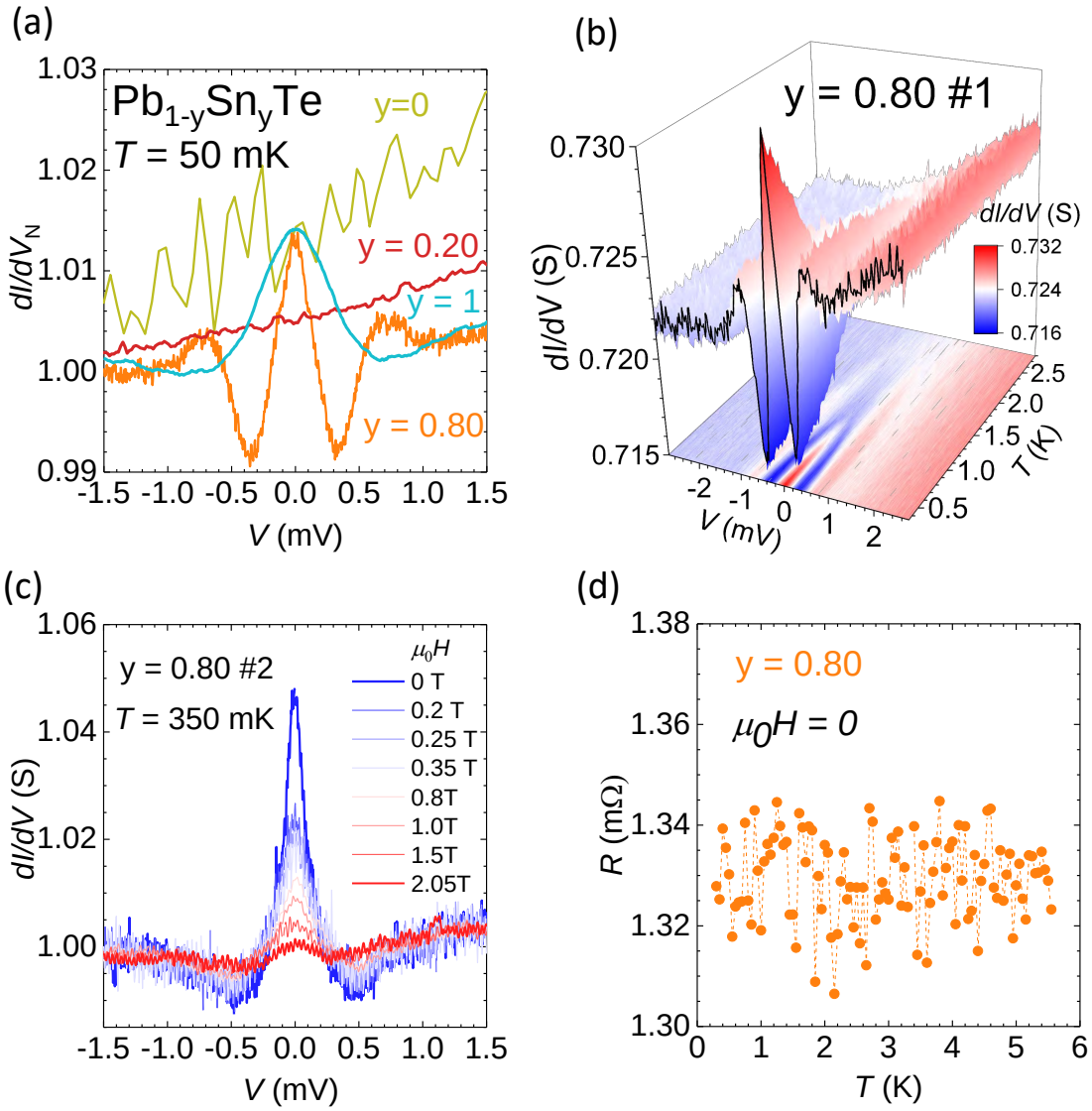

FIGURE 4.1: Differential conductance spectra of soft point-contacts to diamagnetic samples. (a) Differential conductance $\mathrm{d}I/\mathrm{d}V$ at 50 mK normalized to its value at the normal state for (001)$Pb_{1-y}Sn_yTe$ with $y = 0, 0.20, 0.80$, and 1. The spectrum is featureless for $y = 0$ (PbTe) and $y = 0.20$ but shows zero-energy mode characteristics for Sn content ($y = 0.80$ and 1, i.e., SnTe) corresponding to topological crystalline insulator phase. Evolution of the spectrum with temperature (b) and the magnetic field (c) for $y = 0.80$ and two locations of the point contact on the sample surface, respectively. Magnetic field is applied perpendicularly to the (001) plane. (d) Resistance of this sample measured by a four contact method with current density as low as $2.5{\cdot}10^{-3}$ A/cm^2. No global superconductivity is detected.

4.1.2 Magnetically doped $Pb_{1-y}Sn_yTe$

It is increasingly clear that doping with magnetic impurities is the key method for altering topological properties and functionalities. For instance, scattering by Mn ions closes the electron-hole gap in Bi_2Se_3 deposited on superconducting $NbSe_2$ (ref. [11]). Interestingly, Hall resistance of edge channels in ferromagnetic $(Cr_{0.12}Bi_{0.26}Sb_{0.62})_2Te_3$ shows an additional quantized plateau if coupled with superconducting Nb, the effect attributed to the presence of chiral Majorana excitations[149], even though competing explanations have been put forward, too[150]. Usually magnetism is detrimental to the superconducting order, and proximitizing a superconductor with a ferromagnet makes the superconducting state weaker. As shown in Fig. 4.3, Mn doping of $Pb_{1-y}Sn_yTe$ does not destroy zero-bias anomaly but rather enhances the temperature and magnetic field ranges in which they appear. As presented in the Fig. 4.3, dI/dV clear spectroscopic features in the magnetic crystals. The spectrum for $Pb_{0.3}Sn_{0.67}Mn_{0.03}Te$ [Fig. 4.3(a)] exhibits a gap with a small zero-bias peak vanishing smoothly with increasing temperature. For a cleaved (100) surface of $Pb_{0.16}Sn_{0.74}Mn_{0.10}Te$, a splitting of ZBCP, resembling Andreev reflection characteristics in the spectroscopic regime and for a non-zero barrier transparency [126] has been detected [Fig. 4.2(c)]. Detection of the gap feature together with zero-bias conductance peak suggests that, if observed features are indeed coming from the superconductivity its order parameter should be unconventional.

To further investigate ZBCP properties at the lower temperatures, I have performed set of measurements in the dilution refrigerator. Judging from the shape of the spectra, contacts were located closer to the thermal regime of transport. Nevertheless zero-bias field dependence, and conductance spectra evolution as a function of temperature and field are depicted in all the panels of Fig 4.3. Indeed to obtain contacts which shown spectroscopic features (as seen in the Fig 4.3), I have fabricated several tens of specimens. It was only possible using home made transport probe (Described in chapter 2) which fits QD MPMS magnetometer. Using its cryogenic properties, I was able to test up to 3 separate samples (each with 3 point contacts) per day, at the lowest temperature of 1.8 K. Such fast characterization would not be possible using dilution refrigerator. On the other hand, it is not surprising that a semiconducting crystal containing almost 10 % of Mn has greatly reduced mean free path and achieving fully ballistic contacts to this sample seems elusive.

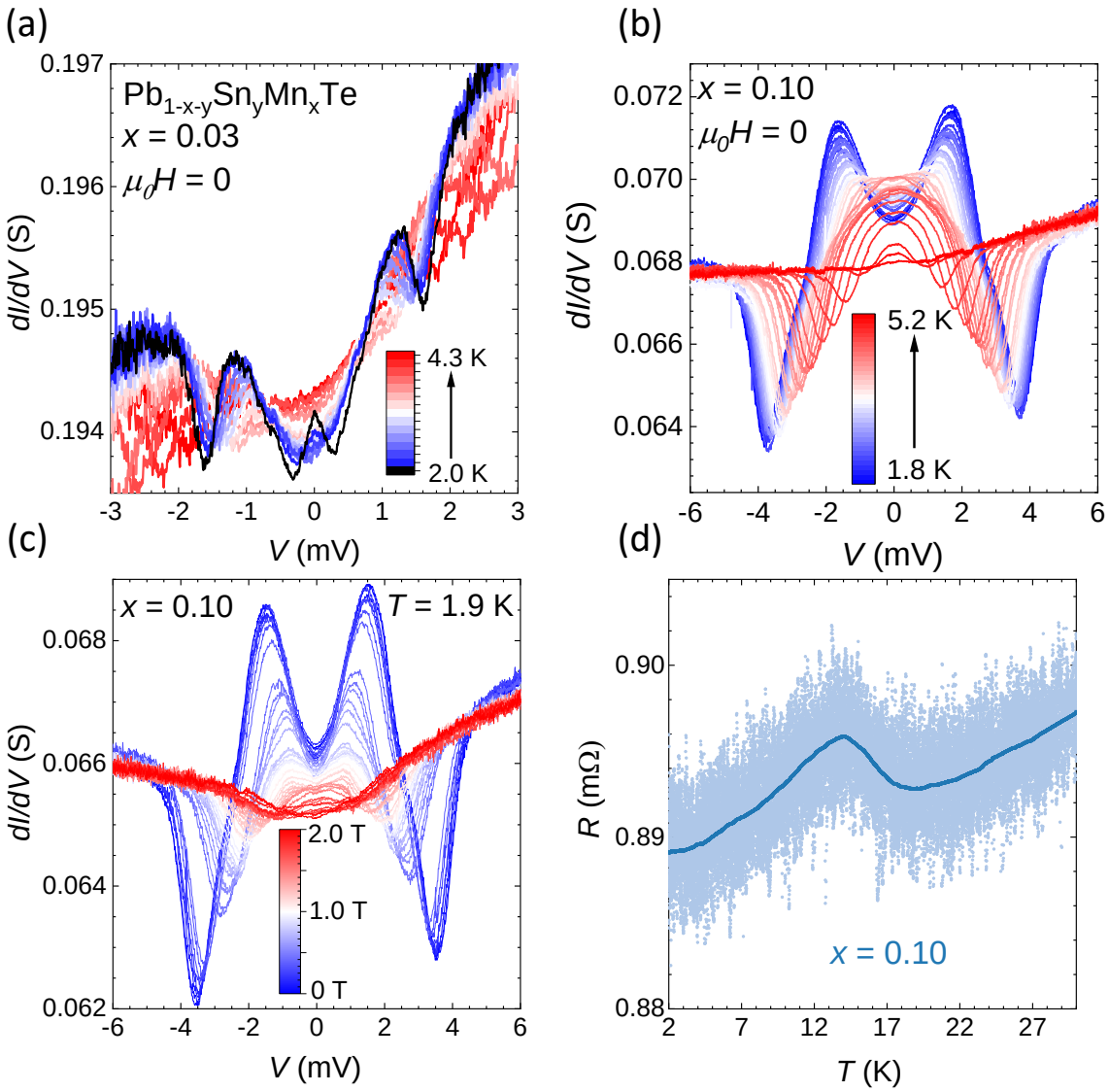

FIGURE 4.2: (a) Temperature dependence of differential conductance spectra for the etched (011) $Pb_{0.30}Sn_{0.67}Mn_{0.03}Te$. (b,c) Evolution of the spectrum with the temperature and magnetic field for the cleaved (001) $Pb_{0.16}Sn_{0.74}Mn_{0.10}Te$. Magnetic field is applied perpendicularly to the sample plane. (d) Resistance of $Pb_{0.16}Sn_{0.74}Mn_{0.10}Te$ measured by a four contact method with current density $2.5 \cdot 10^{-5}$ A/cm^2 (noisy trace), the solid line represents a numerical average over 40 temperature scans. Critical scattering at the Curie temperature $T_{\mathrm{Curie}} = 14$ K is observed but no global superconductivity is detected.

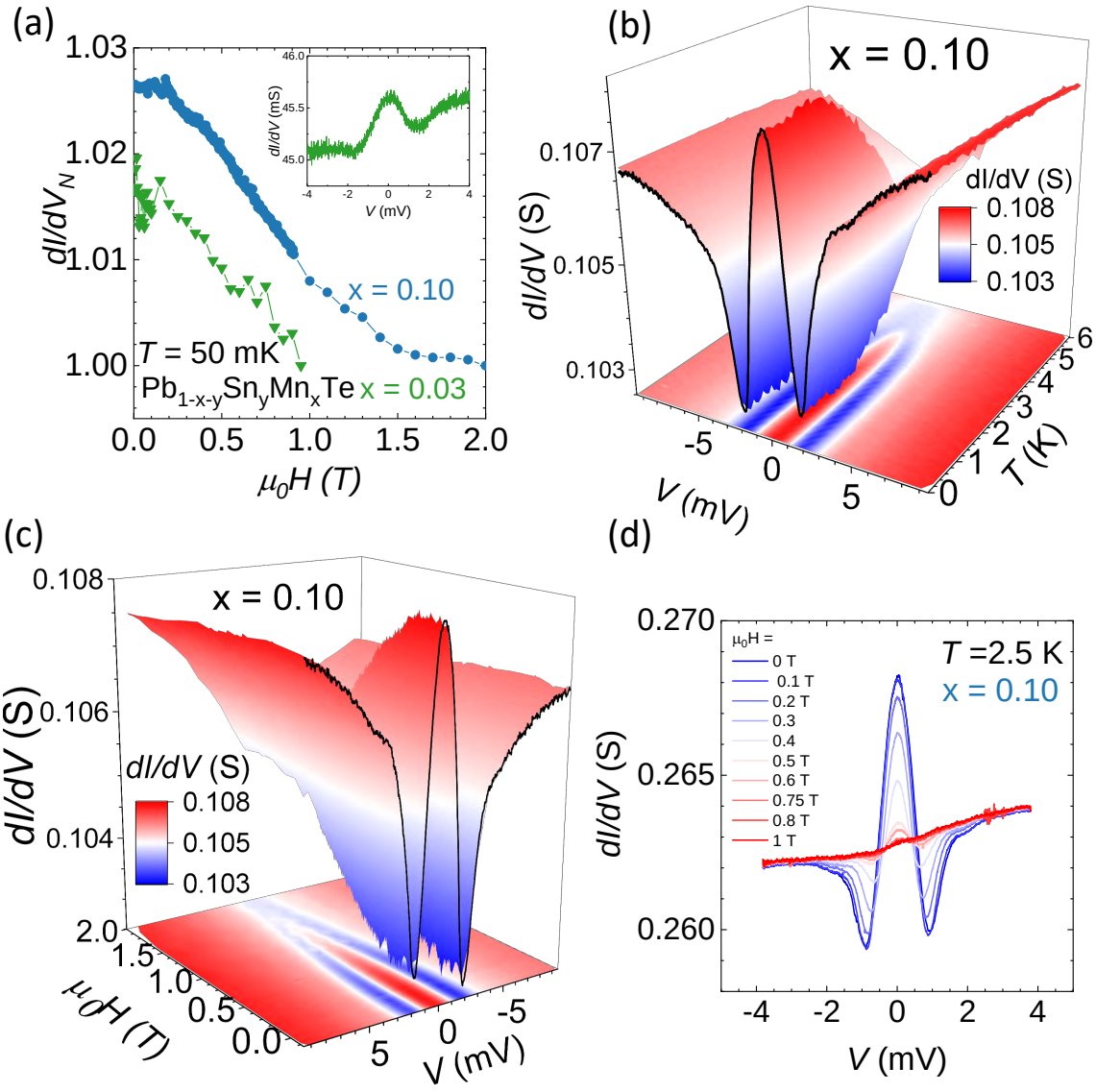

FIGURE 4.3: Differential conductance spectra of soft point-contacts to paramagnetic and ferromagnetic samples showing zero-energy modes without global superconductivity. (a) Normalized peak height field dependence for (011)$Pb_{0.30}Sn_{0.67}Mn_{0.03}Te$ and (011)$Pb_{0.16}Sn_{0.74}Mn_{0.10}Te$. Inset: conductance spectrum for (011)$Pb_{0.30}Sn_{0.67}Mn_{0.03}Te$ at 50 mK. Evolution of the spectrum with temperature (b) and the magnetic field at 50 mK (c) for (011)$Pb_{0.16}Sn_{0.74}Mn_{0.10}Te$. Magnetic field is applied perpendicularly to the (011) plane. (d) Collection of spectra for a less resistive junction at higher temperature, the zero-bias feature is quenched by much smaller magnetic field as compared to the data presented in the panel (c)

The enhancement of superconductive features in ferromagnetic samples is best seen in Fig. 4.4 that depicts the temperature dependence of the contact resistance and a half of the energy distance between conductance maxima(b) and minima(d), Δ, as a function of temperature and the magnetic field for all studied samples with high Sn content. As seen, $\Delta(T,H) > 0$ up to T_c of 4.5 K and $\mu_0 H_c$ of 1.9 T. Furthermore, according to Fig. 4.4, $\Delta(T)$ is quite well described by an interpolation formula of the BCS expression, $\Delta(T) = Ck_BT_c[1-(T/T_c)^{3.3}]^{0.5}$, where C in our case is more than twofold greater than the weak coupling value $C = 1.76$. Similarly, a reasonable account of $\Delta(H)$ data is obtained by using another interpolation formula suitable for type II superconductors, $\Delta(T,H) = \Delta(T,H=0)(1-H/H_c)^{1/2}$. This description of $\Delta(T,H)$ holds for the diamagnetic $Pb_{0.2}Sn_{0.80}Te$, ferromagnetic $Pb_{0.16}Sn_{0.74}Mn_{0.10}Te$, and across the paramagnetic–ferromagnetic phase boundary, the case of $Pb_{0.30}Sn_{0.67}Mn_{0.03}Te$, in which $T_c > T_{\text{Curie}}$. The existence of a transition to a new phase is also documented by a kink in the temperature dependence of the differential resistance for $V \to 0$ at T_c, as shown in Fig. 4.4a. Fig. 4.4d presents data collected for the spectra in thermal regime, as commonly accepted for the case of superconducting point contact phenomenology. As expected for the spectra in this regime, position of the conductance dips (identified as Δ in this regime), may vary upon every cooling cycle. This behavior is observed and documented for the sample with $x = 0.10$ (blue curves). Nevertheless this can as well be expected by network of 1D channels residing at the samples' surface. The collected results demonstrate, therefore, the appearance in diamagnetic, paramagnetic, and ferromagnetic IV-VI TCIs of a new phase below T_c and H_c, which is characterized by an energy gap and excitations residing in its center. This new phase is not accompanied by a global superconductivity and its parameters T_c and H_c vary from junction to junction. The magnitude of ZBCP, about 50 to $500e^2/h$, is consistent with fact that several Ag crystallites participate in the charge transport process. One should bear in mind however, that for the case of point-contact spectroscopy, spin-polarization and finite transmission coefficients across the junction will determine the magnitude of observed spectral characteristics.

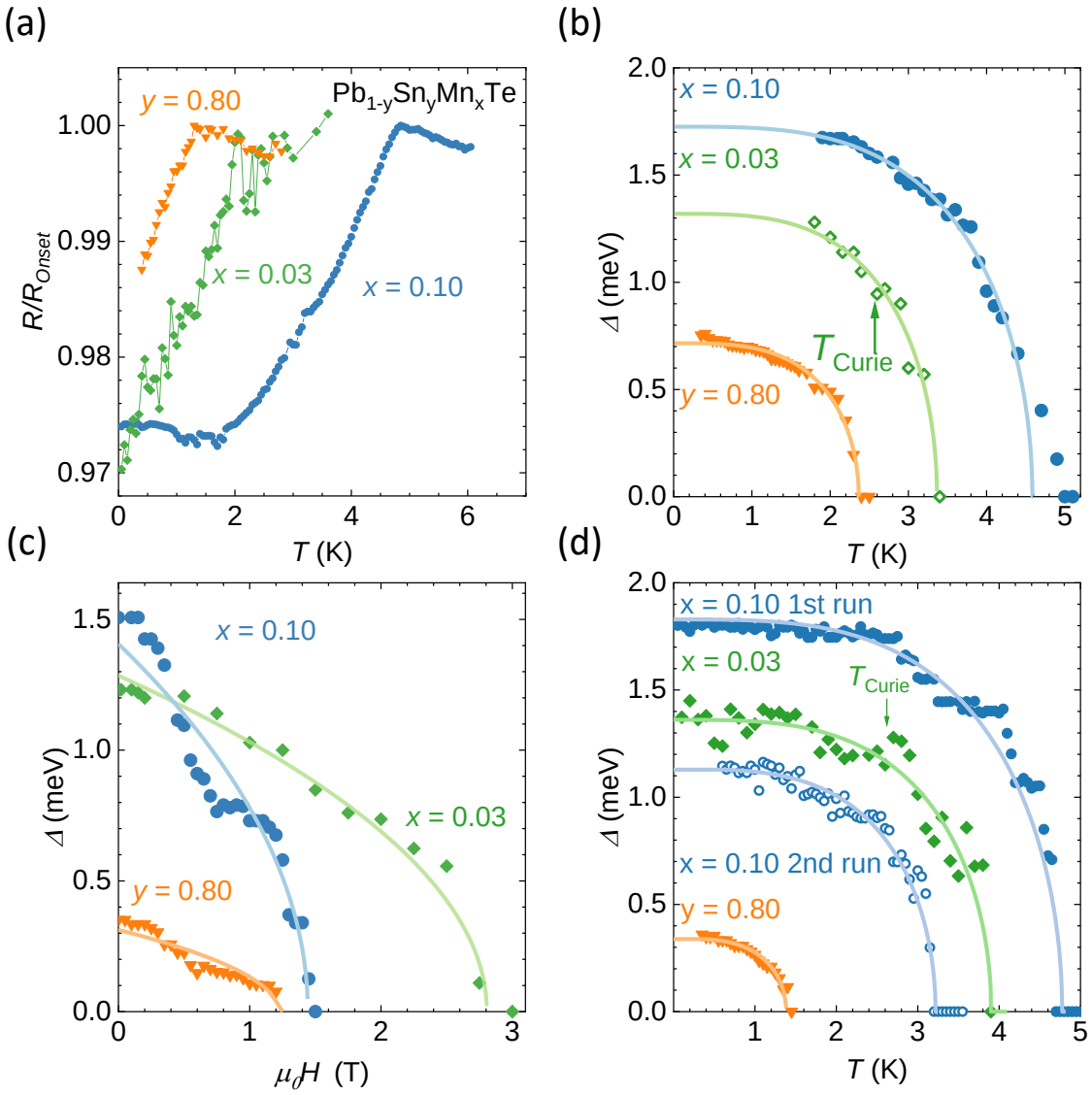

FIGURE 4.4: (a) Temperature dependence of the point-contact resistance at the limit of zero bias pointing to a phase transition. (b,c) Conductance gap Δ evaluated from the differential conductance spectra for samples presented in Figs. 4.1,4.3 and 4.2 for $Pb_{1-y-x}Sn_yMn_xTe$ corresponding to the topological crystalline insulator phase vs. magnetic field perpendicular to the surface plane and temperature, respectively. (d) Field dependence of a gap estimated as a minimum in a conductance spectra which only show ZBCP. Solid lines in (c) are fits to $\Delta(T,H) = \Delta(T,H=0)(1-H/H_c)^{1/2}$. Solid lines in (b,d) are fits of the BCS formula for $\Delta(T)$ to the experimental points treating T_c and C as adjustable parameters ($C = 4.35$, 4.53, and 3.49 from top to bottom respectively; $C = 1.76$ in the BCS theory).

How to estimate the energy gap? Some of the features observed in our spectra, are resembling characteristics which are usually associated with Andreev reflection in normal metal/superconductor junctions. Especially dI/dV measurements presented in the Fig 4.2(b),(c) show double-peak structure, which is predicted by BTK (Blonder, Tinkham, Klapwijk) theory for a finite transmission coefficients. I will briefly discuss origin of this spectral shape for the N/S junctions. The existence of a superconducting gap has a consequence, for electronic transport across interface between a metal and semiconductor. A single electron cannot tunnel to a superconducting gap, as there are no quasiparticle states available in the superconductor. There is one process, however, which electrons can use to "sneak" inside a superconductor, this process is called Andreev reflection. In this process two electrons with the opposite spins and quasi-momenta can tunnel inside the superconductor and form a Cooper pair. In other words, instead of extra electron injected from a normal metal, the incident electron is retroreflected as a hole with opposite quasi-momentum. As two electrons are injected below the energy of a superconducting gap, the value of the conductance increases. For the perfect interface, the conductance below the gap can be doubled as compared to the normal state.

Realistically, the physical picture is of course, much more complicated. The interface, almost in all point-contact spectroscopy experiments is not perfect. Usually this happens due to formation of native oxides both on the normal and superconducting electrodes. Blonder, Tinkham and Klapwijk[151] tackled this problem theoretically and provided elegant theoretical model which is broadly recognized and appreciated by the community. All the considerations have been done for 1D system. The interface degradation is incorporated within the model as an additional δ-function potential located at the interface. Additionally introducing a step potential across the N/S boundary (similar to the Heavyside θ function) the authors taken into account the Fermi velocity mismatch. Thus, quality of the interface is modelled by a phenomenological parameter Z. The quasiparticle transmission probability $\mathcal{T}$ in this model is given by:

$$\mathcal{T} = \frac{1}{1+Z^2} \; \Delta \to 0. \tag{4.1}$$

The probability of Andreev reflection at the Fermi energy reads:

$$\mathcal{A} = \left(\frac{1}{1+2Z^2}\right)^2 \tag{4.2}$$

As expected for the two-particle process, the Andreev reflection probability of the order of $\mathcal{T}^2$. The calculations of $I-V$ and dI/dV characteristics were performed withing Bogolubov-De Gennes framework, which is analogous to the Schroedinger equation for electron and hole quasi-particles in a superconductor. Of course, the BTK model was extended to account many different physical processes happening at the interface, such as finite quasiparticle lifetime [152] or spin polarization [153]. By fitting the BTK model, one can obtain a superconducting energy gap or spin polarization if a junction between a superconductor and a ferromagnet is made, which bring us to the measurements presented here. In fact, nowadays, using BTK model is somewhat standard way of obtaining before mentioned parameters. In our case, however, most of the spectra, additionally to the gap feature which may originate from Andreev reflection, show enhanced conduction at zero bias, which suggests that if any superconductivity is present, it is probably unconventional. Moreover, despite the great experimental effort, we are not able to find any signature of superconductivity besides spectra presented above. That's why we decided to take another route and identify the energy associated with the gap differently. For the spectra presented in the Figs. 4.1(c),4.3(b,c) we take the energy gap Δ as half of the energy distance between conductance minima. Having in mind, these dips are often interpreted as a result of non-ideal conduction through the contact, they often appear at the energies close to the energy of the gap [8, 126]. The dips shift to lower bias value as a field and temperature and indicate the qualitative behavior of the gap. Quite often the dips are ignored when a BTK model is fitted to the conductance spectra [20, 22]. This introduces only a small error into estimation of the gap, provided that magnitude of the dips is small. On the contrary, if magnitude of conductance dips is high, the gap overestimation can be very significant [148]. It is important to stress, that in the case of the presented measurements it is not critical to precisely estimate the value of the gap, as the microscopic mechanism driving observed spectra is not yet understood.

A class of the spectra where the gap feature can be undoubtedly identified are depicted in the Figs 4.1(b) and 4.3(a-c). In this case the maximum in the dI/dV is attributed to Δ. It should be noted that spectrum presented in the Fig 4.1(b) is completely free from any heating effects despite its low resistance. Fig 4.5(b) illustrates how magnetic field quenches the zero-bias peak and leaves a gaped spectrum. From the experimental point of view, one needs to address one more issue. As the sample temperature or magnetic

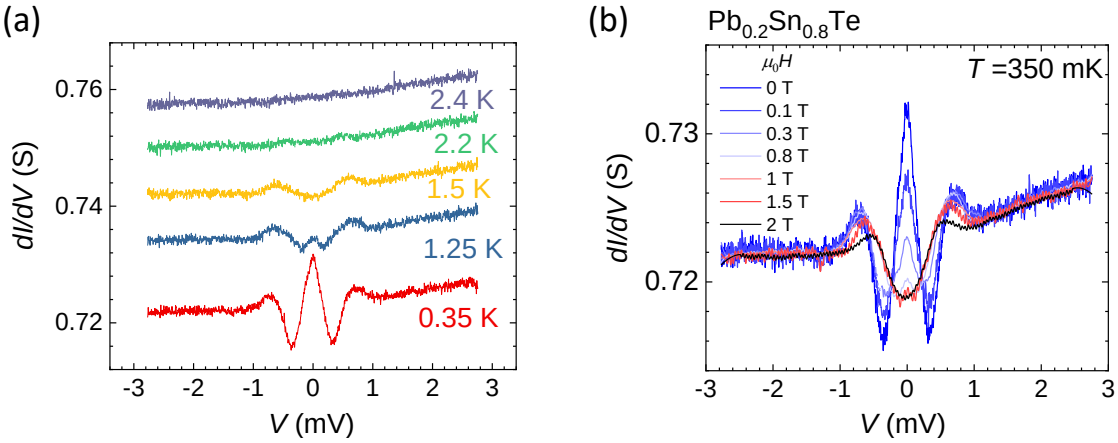

FIGURE 4.5: Panel (a) illustrates slices of Fig 4.1(b). It shows how ZBCP vanish as a function of temperature leaving clear gap structure. For clarity an offset has been put between the traces. At 2.4 K spectrum is featureless. Panel (b) illustrates how the zero-bias feature is suppressed by the magnetic field.

field approaches T_C or H_C, it is more challenging to estimate the energy of the gap. Fig 4.5 shows dI/dV traces selected from the Fig 4.1(b). Gap structure is clearly visible for temperatures up to 1.5 K. It is still visible at higher temperatures, however it's magnitude is greatly reduced.

Contact Fritting Despite the ease of fabrication and stability against vibrations soft-point contacts, once made, cannot be modified as easily as the contacts made using metallic tips. It was already mentioned in the section devoted to point-contact spectroscopy, Gonelli et al.[124] found that short current/voltage pulses can be used to modify contact area of soft point-contacts. The method is known otherwise as "contact fritting" and is commonly used in electronics as a convenient tool to modify resistance of metallic junctions[126]. In the case of our samples, freshly prepared silver paint contacts reveal behavior characteristic for superconducting point contact in topologically non-trivial samples. However, some of the contacts stopped working after temperature sweeps or showed no structure during initial measurements. By application of the contact fritting method characteristics of differential conductance spectra in topological samples can be modified. This is best seen in Fig. 4.6(a). A typical pulse sequence consists of 1 ms pulses with amplitude 100 mA, with the repetition rate of 10 Hz. Such a sequence does not awake any structure in conductance of non-topological $Pb_{0.80}Sn_{0.20}Te$ [Fig. 4.6(b)]. Application of the current pulses can also be used to effectively change area of the contact. Usually, for bulk superconductors resistance of the N/S junction scales with the contact area. In a recent paper, Zhigadlo et

al. [154] perform soft-point contact studies on the non-centrosymmetric superconductor Mo_3Al_2C. Mean-free path in this material is as short as 3 nm so achieving contacts in ballistic regime is extremely difficult. However, the authors were able to show, that application of short current pulses progressively reduces resistance of the junction and two peaks from Andreev reflection merge to a single,zero bias peak for highly conductive contact. Moreover, the authors convincingly shown that the conductance dips originating from heating effects move towards lower biases as the junction resistance decreases. This behavior denies that such dips have any relation with the superconducting energy gap or with any intrinsic energy scale of studied material. On the contrary, for the Ag/TCI junctions, we do not find any systematic relation between the junction resistance and the position of the dips or other spectral features. The Figure 4.7 presents conductance spectra obtained for the same junction whose resistance is changed by the current pulses. All of the spectra show clear conductance minima, which appear around average bias voltage of 1.8 mV. Importantly position of the dips does not show any systematic dependence on the contact resistance,as in the case of previous studies on point contacts made to topological materials [20]. It is even more interesting as 1.8 meV is almost exactly the value identified as a gap for both thermal and intermediate regime as shown in the Fig 4.4(b,d) for the $x = 0.10$. Similarly a comparison between the mean-field fitting prefactors is given in the Table 4.1. It seems that the error introduced by heating beneath

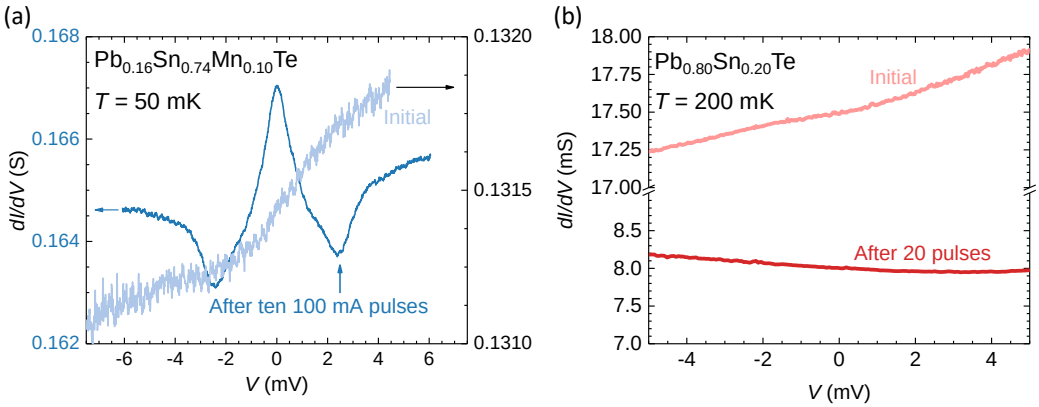

FIGURE 4.6: Effect of current pulses on differential conductance characteristics in topological and non-topological samples. (a) In topological samples pulses can restore a peak structure in the case of contacts that have been initially featureless. (b) Differential conductance remains featureless in non-topological samples.

the contact is not bigger than 10 % for all investigated samples. This observation may be a hint that the conductance dips are indeed associated with some intrinsic energy scale of the system under study. A more surprising

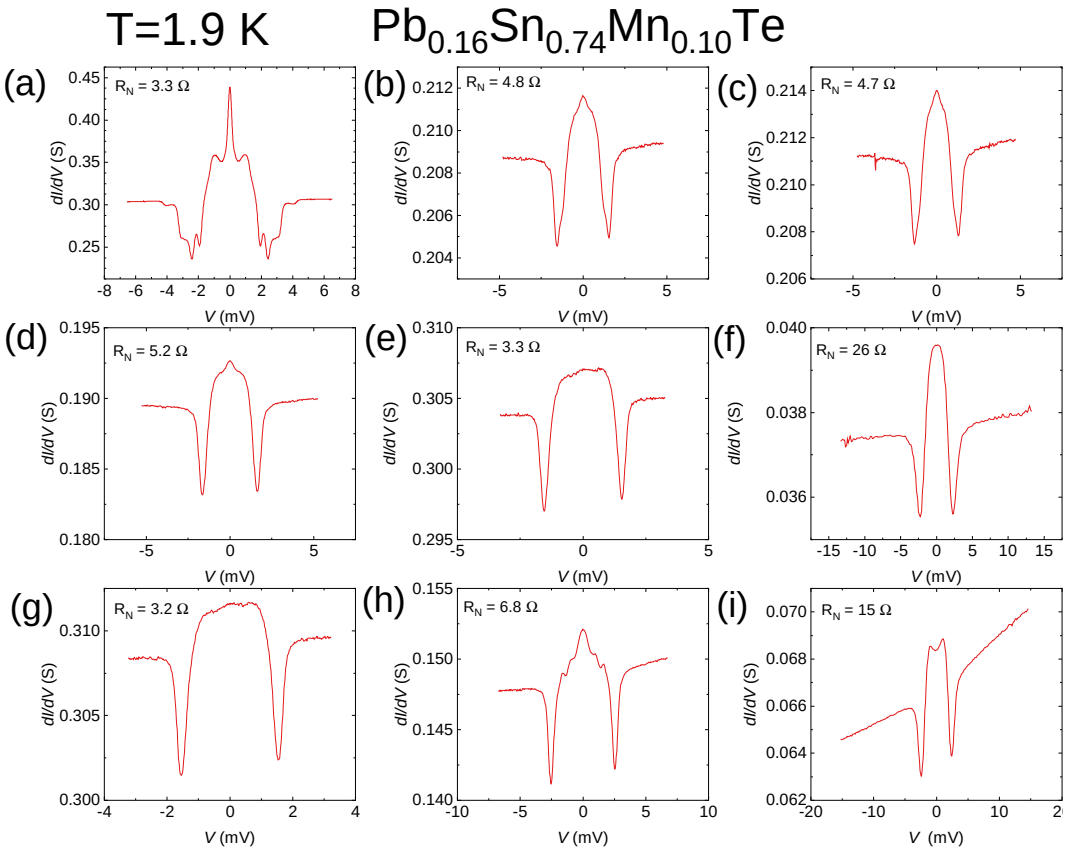

FIGURE 4.7: A collection of point contact spectra obtained by applying small 1 ms current pulses across the contacts for $Pb_{0.16}Sn_{0.74}Mn_{0.10}Te$. The pulse height varied from 10 mA to 50 mA depending on the contact resistance.

is the fact that spectral features observed in the collected measurements do not seem to depend on the contact resistance as well. This is at odds with the superconducting point contact phenomenology, which predicts spectral gap feature (i.e. closer to ballistic regime) to appear as the junction area is reduced. For example, the spectrum with conductance about 0.065 S (Fig 4.7(i)) resembles two peaks characteristic for Andreev reflection, whereas for the twice more resistive junction (0.037 S)(Fig 4.7(f)), a single, zero-bias feature is seen instead. One can explain this, by invoking the fact, that multiple parallel channels are formed across the junction and their total resistance does not accurately reflect size of each separate channel. Alternatively, such a behavior could also be seen if the observed phenomenology were connected with the presence of 1D objects on the sample surface. This kind of object could be a low-dimensional superconductor. In this case only a part of the junction

Sample	$C_{Thermal}$	$C_{Ballistic/Intermediate}$
$Pb_{0.20}Sn_{0.80}Te$	3.3	3.6
$Pb_{0.30}Sn_{0.67}Mn_{0.03}Te$	4.1	4.5
$Pb_{0.16}Sn_{0.74}Mn_{0.10}Te$	4.4	4.4

TABLE 4.1: Collection of fitted BCS C prefactor in different transport regimes. The data for each sample was obtained in a separate cooling cycle.

touches actual the superconductor and the other part probes topological material in its normal state. It is instructive to discuss whether we can apply formulae given by Sharvin and Maxwell (introduced in Chapter 2), to describe results of the point contact studies of the topological materials. Usually, the parameters (e.g. k_F) are estimated basing on the data available/measured for the bulk. Topological Crystalline Insulators, on the other hand, are known to possess not only the non-trivial surface states, but topological states bound to the edges of atomic terraces. Thus the actual physical properties under the contact must be different from that of the bulk. The mean-free path for topological surface states can be obtained from the parameters extracted, for example, from quantum oscillations of the resistance. For SnTe [84] the mean surface free path is of the order of 40 nm, whereas the bulk one is below 10 nm. For such a complex system it is not clear, what value of k_F should be taken into the actual calculations.

Looking at all the data gathered above, we can conclude that either point-contacts form low dimensional TCI/Ag interface, or some low dimensional object on the crystal surface resembles superconducting point contact phenomenology when probed with silver electrode.

4.1.3 Magnetic anisotropy of differential conductance

Some information on the dimensionality of the system under investigation can be achieved by magnetic field rotation. It is especially challenging in point-contact spectroscopy as point contacts are prone to mechanical perturbations. Rotation of the sample stage can even destroy the contact and it is not a proffered method for studying the anisotropy of differential conductance. However, many modern cryostats are be equipped with vector magnets, able to produce **H** vector pointing at any direction. Our dilution refrigerator system is equipped with such a vector magnet, capable of generating magnetic field of the order of 6 T along Z-axis, and 1 T along X and Y axes. In order to probe magnetic anisotropy of the point-contact spectra, differen-

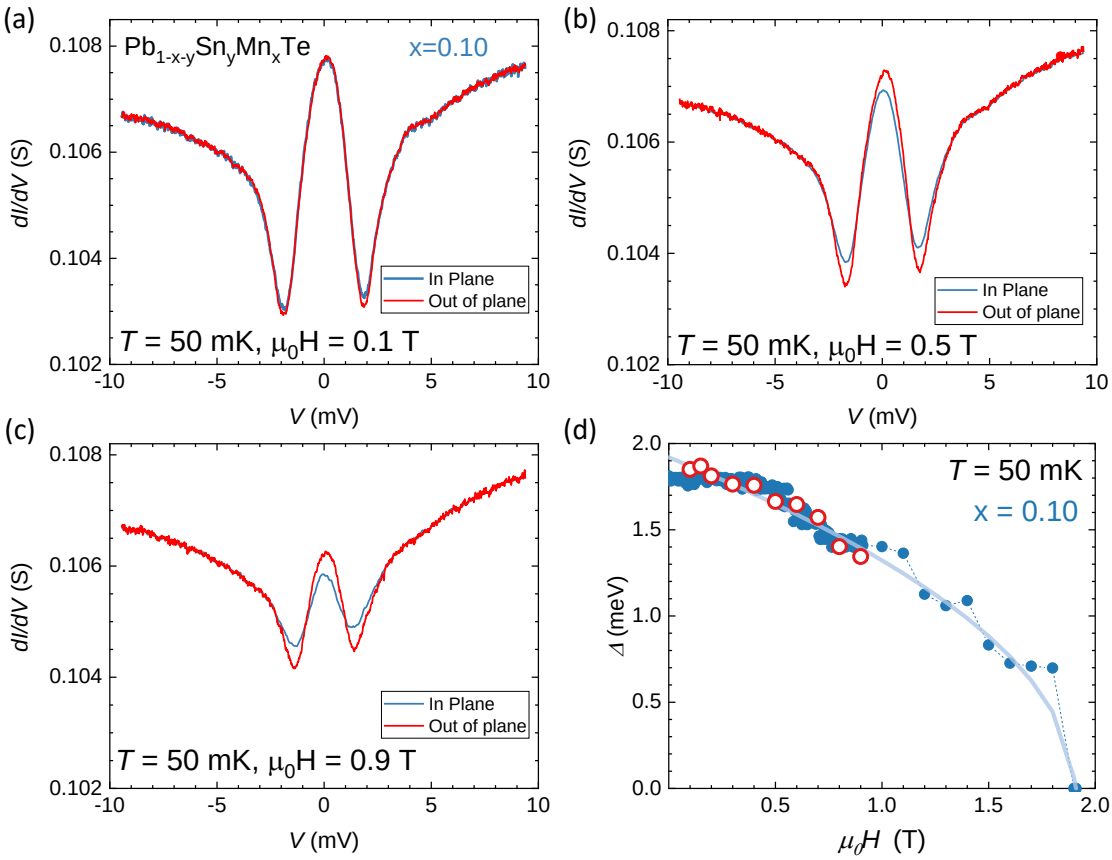

FIGURE 4.8: (a-c) Differential conductance spectra at various perpendicular and in-plane magnetic fields at 50 mK for $Pb_{0.16}Sn_{0.74}Mn_{0.10}Te$ sample. (d) Conductance gap evaluated from the differential conductance spectra presented in the panels (a-c) vs.magnetic field perpendicular and parallel to the surface (full and empty symbols, respectively).

tial conductance of the $Pb_{0.16}Sn_{0.74}Mn_{0.10}Te$ sample has been measured as a function of **H** applied perpendicular and parallel to the sample surface. As seen in Fig. 4.8 there is some anisotropy in the peak heights but no noticeable differences in the width of the spectra can be found. Actually, this indicates that the observed transition has no 2D character. As for the literature data, so far, only one report investigated the issue of anisotropy of differential conductance[22], shown in the Fig 4.9. The authors attributed obtained results to the dimensionality of the contact. In this picture current is flowing through a 1D constriction with effective diameter comparable to the superconducting coherence length.

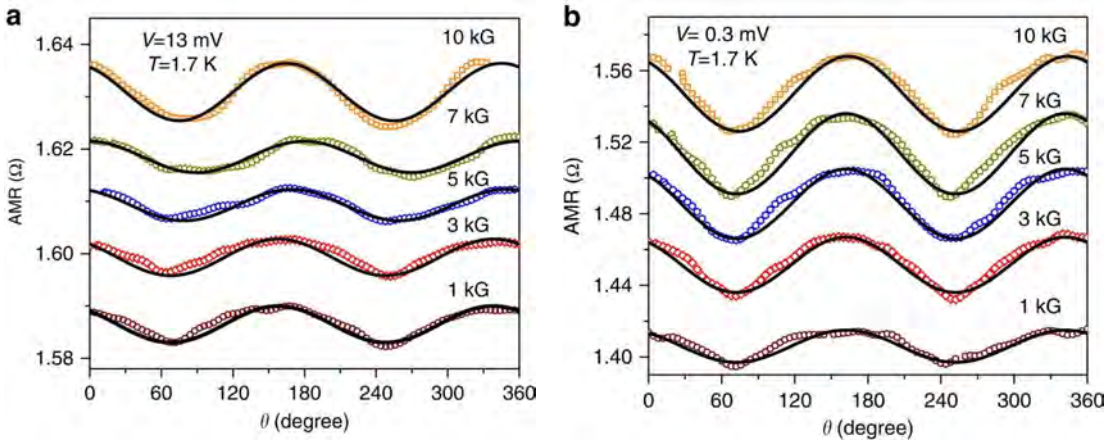

FIGURE 4.9: Aniostropic differential resistance of a Ag/TaAs junction. Panel (a) corresponds to the high bias (V=13 mV), panel (b) corresponds to the low bias (V=0.3 mV). Solid lines are $\cos^2\theta$ fits. As appeared in the Ref. [22].

4.1.4 The interface effect

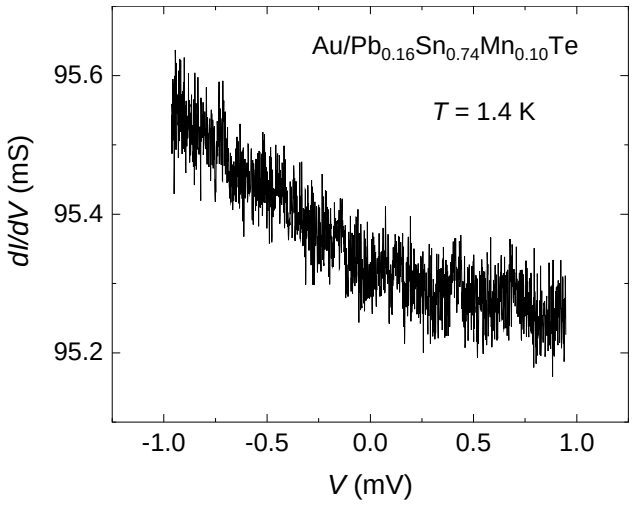

FIGURE 4.10: Differential conductance of Au welded contacts to TCI. Spectrum does not show any signatures of zero-bias anomaly or a gap.

From the measurements of magnetoconductance and exploration of transport regimes through the contact, the experimental results suggest that observed features might come from one dimensional object. This section is devoted to investigations of the interface between Ag and the TCI. Our point-contact spectroscopy experiments have been performed by using silver paint,the

remaining contacts are spot-welded into the sample to ensure a good electrical connection. A sanity check spectroscopy experiment is performed using spot-welded contacts, which also does not show any superconductive features (Fig. 4.10).

We have carried out resistance measurements employing a Corbino geometry with silver paint contacts, as shown in Fig. 4.11(a). No change of resistivity starting at T_c is detected on cooling, which confirms the absence of global superconductivity of TCI samples.

To check properties of the Ag/TCI interface further on, we have deposited a 50 nm layer of Ag using UHV e-beam evaporator onto a ferromagnetic $Pb_{0.16}Sn_{0.74}Mn_{0.10}Te$ sample. Prior Ag deposition, the sample is prepared in the same way as the samples used for point contact spectroscopy. Results of four probe measurements and point-contact spectroscopy on Ag/TCI interface do not exhibit any noticeable superconductivity, as shown in Fig. 4.11(b,c). However, if a standard spectroscopic measurement is performed on across the interface, a features characteristic for Andreev reflection appear Fig. 4.11(d). This is not surprising, as the experiment is very similar to point contact spectroscopy on the TCI surface alone, where Ag/TCI interface is formed by the paint instead of a film. However the lack of a phase transition signatures in resistance measurements across the interface both in 4 probe and Corbino geometry is puzzling. Yet again it suggests that the investigated phenomenon takes place at the spatially confined region under the contact or the silver film.

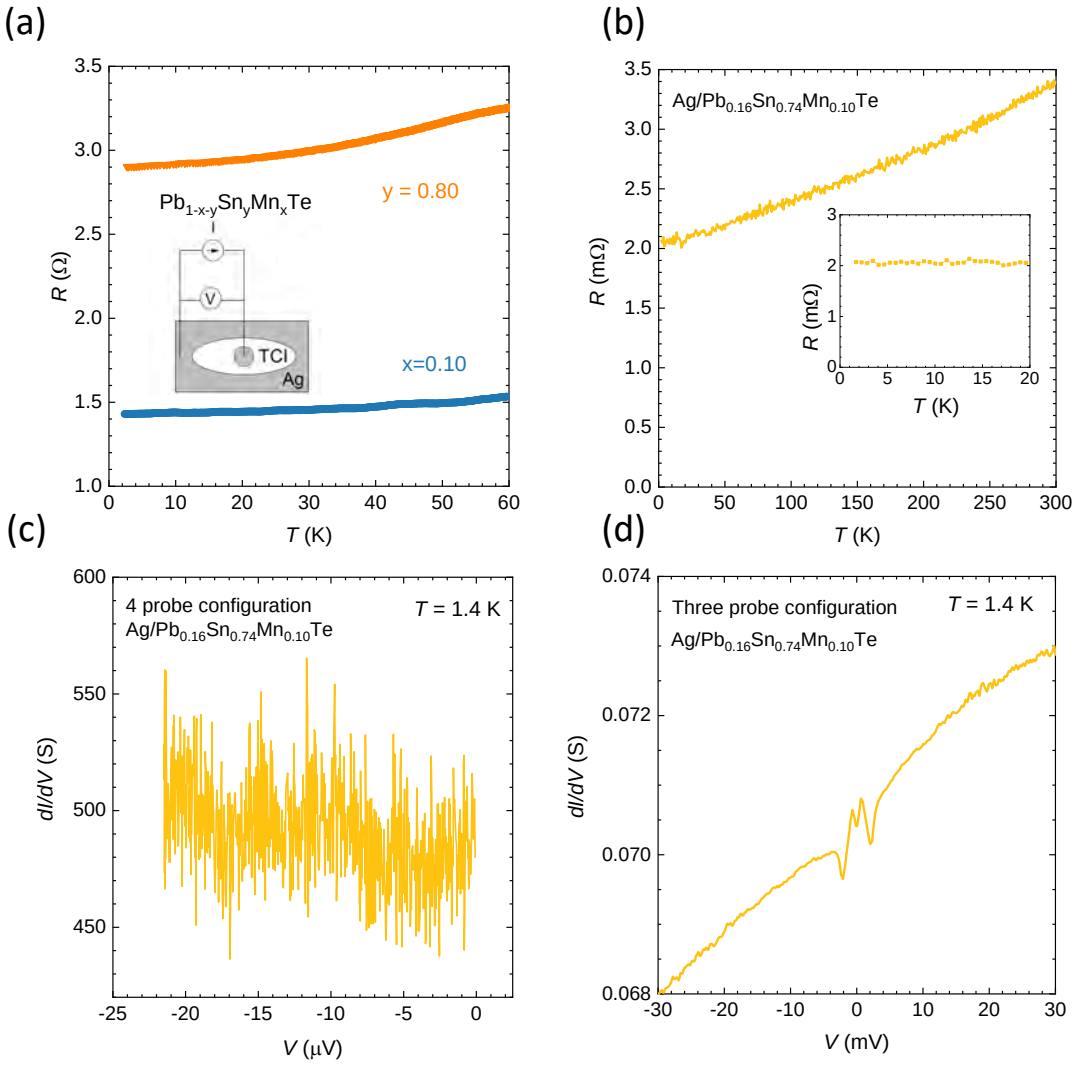

FIGURE 4.11: Search for superconductivity at Ag/TCI interface. (a) Temperature dependence of two terminal resistance in Corbino geometry. Data collected for diamagnetic $Pb_{0.20}Sn_{0.80}Te$ and ferromagnetic $Pb_{0.16}Sn_{0.74}Mn_{0.10}Te$ do not show a resistance decrease at T_c. Inset illustrates measurement configuration. (b) Resistance against temperature for an Ag film deposited onto $Pb_{0.16}Sn_{0.74}Mn_{0.10}Te$ measured by a four probe method. Inset presents the low-temperature range of the $R(T)$ dependence. No superconductivity is detected down 1.4 K. (c) Featureless 4 probe differential conductance measured across deposited Ag film. (d) Soft-point contact measurement across the Ag/TCI interface showing Andreev reflection characteristics.

4.2 Discussion

I will now discuss mechanisms that might account for the observations considering first phenomena that do not involve superconductivity and subsequently phenomena for which the superconductivity is essential but have to exist only locally, as neither magnetization nor resistance measurements point to the presence of a global superconductivity in our samples, as shown in Fig. 3.13 and Figs 4.1d and 4.3d, respectively.

4.2.1 Search for superconducting precipitates by SQUID magnetometry

The starting point here is a previous detection by SQUID magnetometry, in a certain class of PbTe samples, of a diamagnetic response specific to a superconductor with critical temperature of Pb, $T_c = 7.2\,\mathrm{K}$ (ref. [155]). The description of magnetization $M(T, H)$ pointed to superconductivity brought about by Pb nanoprecipitates with a typical diameter evaluated to be of the order of 100 nm (ref. [155]). We assess the presence of superconducting Pb, Sn, and related precipitates in samples of topological $Pb_{0.20}Sn_{0.80}Te$ and non-topological $Pb_{0.80}Sn_{0.20}Te$ by SQUID magnetometry. We start by discussing results of magnetization measurements for a reference sample $Pb_{0.63}Sn_{0.37}Se$. As shown in Fig. 4.12, two clear diamagnetic steps in the temperature and magnetic field dependencies of magnetization are recorded, quite accurately corresponding to Pb and Sn superconducting transition temperatures 7.2 and 3.7 K as well as critical magnetic fields at 2 K, 70 and 25 mT, respectively. The presence of magnetic hystereses points to some pinning. Assuming a spherical shape of precipitates, the field derivative of the magnetic moment m assumes the form,

$$dm_i/dH = -3\mathcal{M}_i/8\pi\rho_i, \tag{4.3}$$

where $\mathcal{M}_i$, ρ_i, and dm_i/dH are mass, density, and the experimentally established slopes corresponding to $i =$ Pb or β-Sn. From the experimental slopes $d\mathrm{m}_i/dH$, depicted in Fig. 4.12(b), we obtain precipitation masses of $\mathcal{M}_{\mathrm{Pb}} = 1.7\,\mu\mathrm{g}$ and $\mathcal{M}_{\mathrm{Sn}} = 14\,\mu\mathrm{g}$, which lead to the weight fraction of precipitates $f = 0.04\%$, as the sample weight is 38 mg.

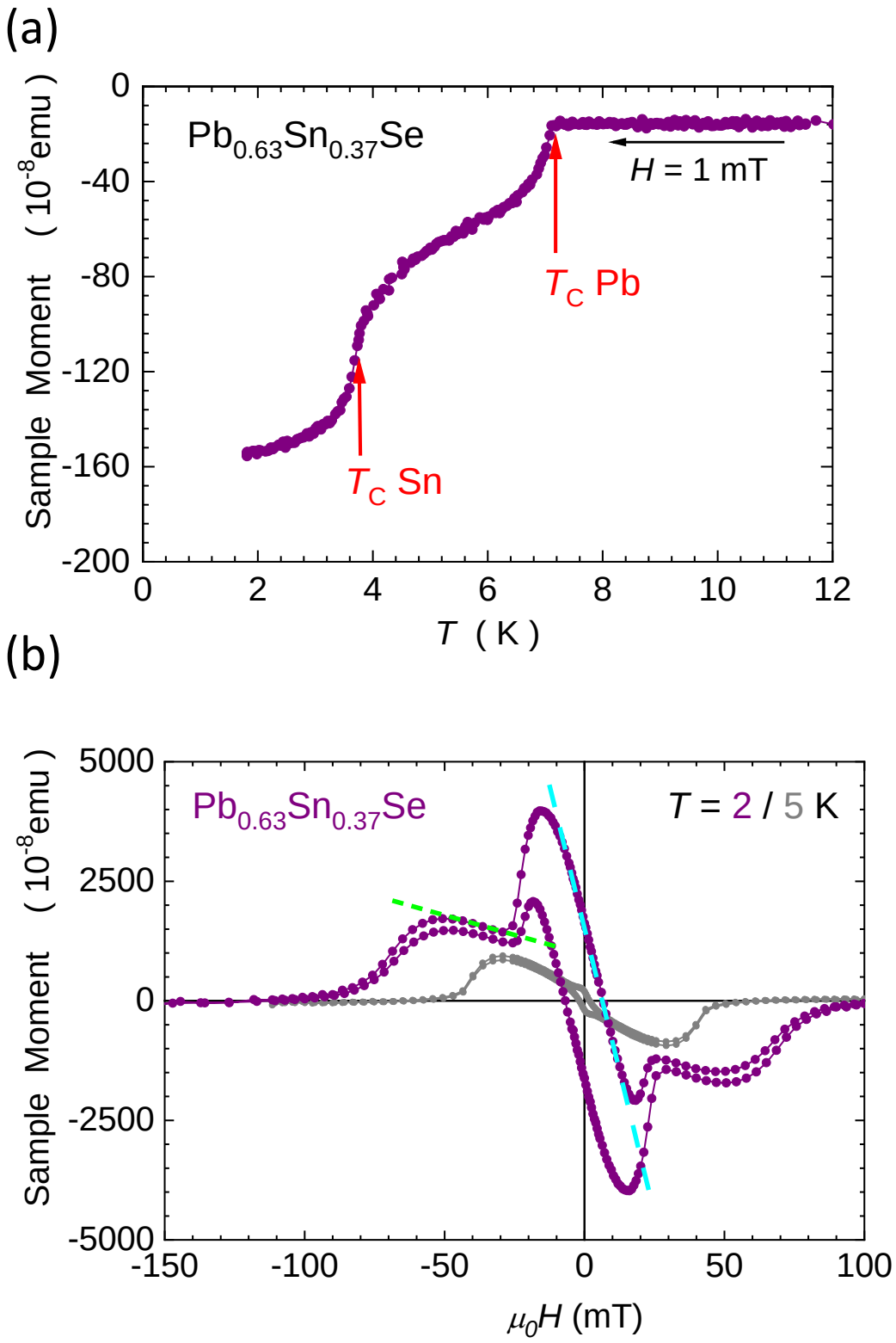

FIGURE 4.12: (a) Magnetic moment of a reference sample $Pb_{0.63}Sn_{0.37}Se$ measured on cooling in 1 mT. Lead and tin superconducting transitions are marked by arrows. (b) Magnetization loops for the same sample after subtracting the diamagnetic component linear in the magnetic field. Dashed lines show slopes taken for evaluation of Pb and Sn masses. The evaluated weight fraction of superconducting precipitates is 0.04%.

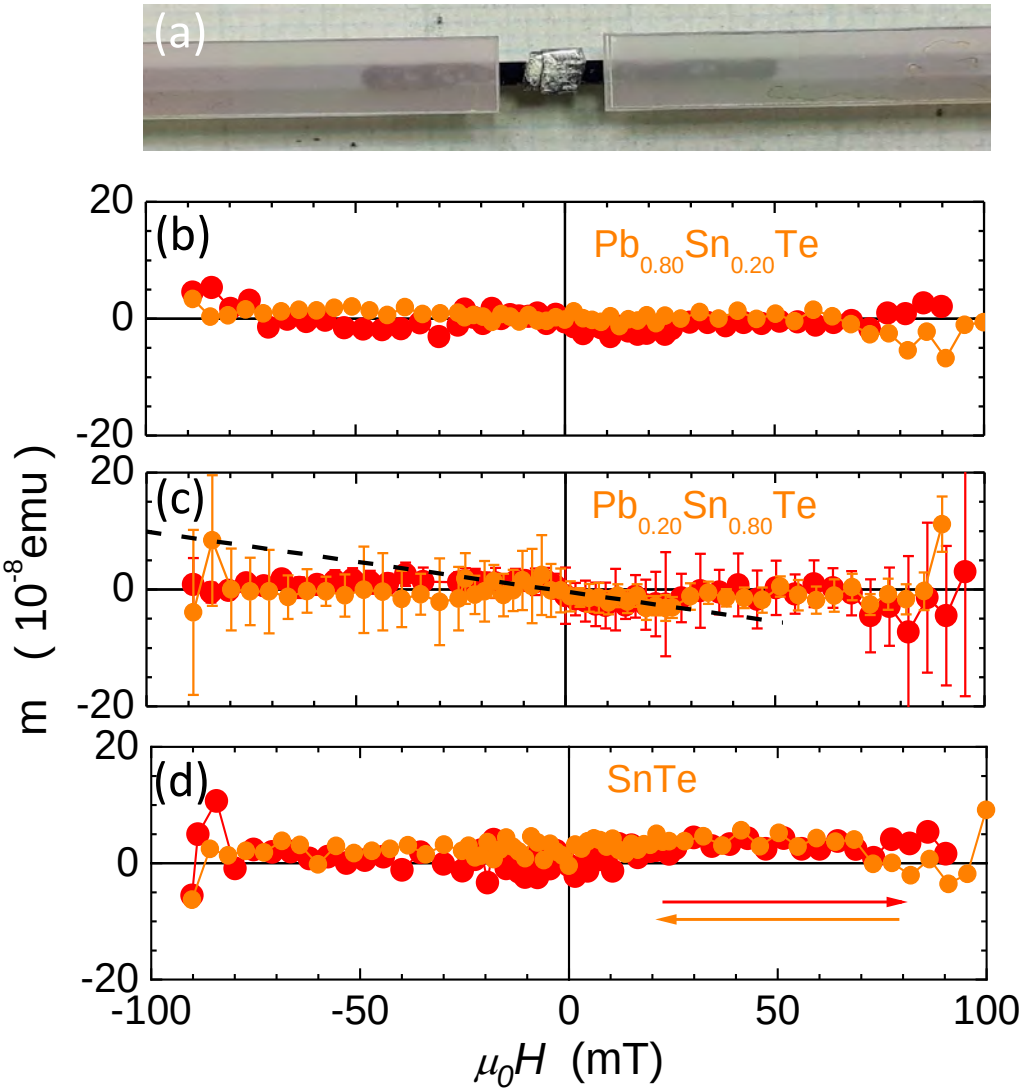

FIGURE 4.13: Search for superconducting precipitates at 2 K. (a) SQUID sample holder. (b–d) Magnetic moment of $Pb_{1-y}Sn_yTe$ samples after compensating the diamagnetic signal linear in the magnetic field, $y = 0.20, 0.80$, and 1, respectively. Brighter and darker experimental points correspond to measurements for two sweeping directions of the magnetic field. The evaluated upper limit of the weight fraction of superconducting precipitates is 0.1 ppm [dashed line in (c)].

Neither $Pb_{0.20}Sn_{0.80}Te$ nor $Pb_{0.80}Sn_{0.20}Te$ shows such a signal. We assign a large concentration of Sn and Pb precipitates in $Pb_{0.63}Sn_{0.37}Se$ to the fact that Sn content $y = 0.37$ is close the solubility limit $y \simeq 0.40$. In order to test our telluride samples $Pb_{1-y}Sn_yTe$ with even higher sensitivity and, in particular, to compensate a relatively large bulk diamagnetic signal, a dedicated sample holder has been prepared. As illustrated in Fig. 4.13(a), 20–40 mm long and 5 mm wide strips of sapphire are glued to the silicon sample holder[156]

forming in the holder center a gap of the length of about 5 mm, to which studied samples are inserted [Fig. 4.13(a)]. I inherited this method from the advisor of this thesis Prof. Maciej Sawicki and Dr. Katarzyna Gas, who describe it thoroughly in a recent article [156]. As these sapphire strips extend from the gap for about 8 cm each way, by adjusting the mass of measured samples to be inserted into the gap, the total signal can be made field independent (typically down to 2% of the initial slope), provided that both the sample and the sapphire stripe do not contain any magnetic or superconducting inclusions. We use a pure GaAs sample to determine a background signal of the sample holder. By adjusting masses of $Pb_{1-y}Sn_yTe$ samples of interest here, and after correcting for sapphire response[156], we obtain SQUID signals presented in Fig. 4.13(b–d). The magnitude of noise indicates that for a mean mass of our samples, i.e., 60 mg, the upper limit of the weight fraction of precipitates that could give a response of the type presented in Fig. 4.13 is 0.1 ppm.

Superconducting contaminants in a silver paint

It can be hypothesized that silver paint employed for point contact spectroscopy contains superconducting contaminants which might account for the observed features. This scenario is excluded by magnetization measurements of silver paint deposited on a Si sample presented in Fig. 4.14. A signal from residual paramagnetic impurities superimposed on a temperature independent diamagnetic response is found. Furthermore, considering a possible diffusion of Sn or Pb towards the Ag electrode or the dislocation formation by the temperature stress, the magnetic response of the SnTe sample with the topological surface covered entirely by the same silver paint has been measured. As shown in Fig. 4.15, no superconductive features are detected down to the lowest accessible temperature of 2 K.

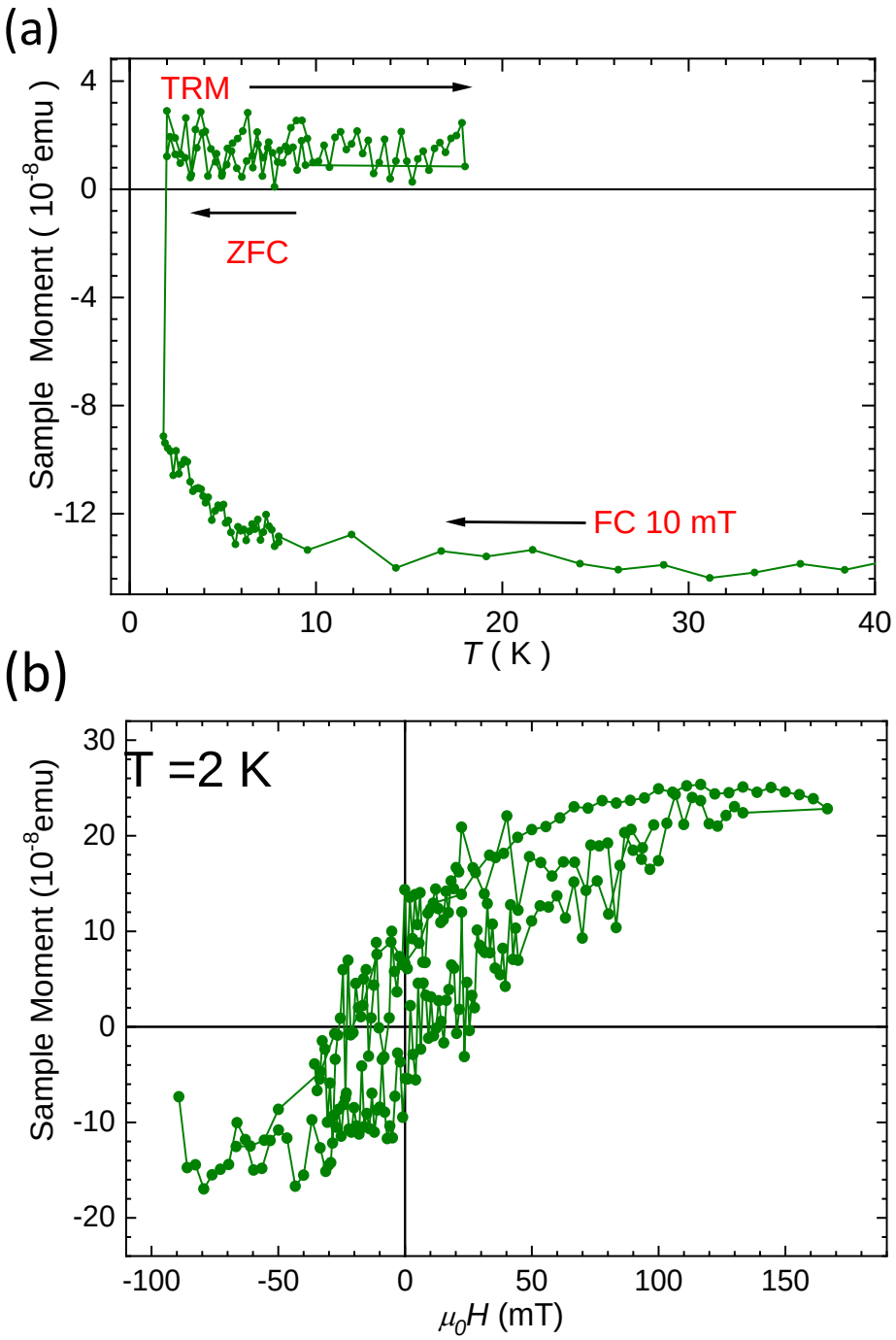

FIGURE 4.14: Search for superconducting contaminants in silver paint employed for soft point contact spectroscopy deposited on Si. (a) Magnetic moment as a function of on temperature. (b) Magnetization vs. magnetic field at 2 K. Data are corrected for substrate diamagnetism.

4.2.2 Dislocations-induced superconductivity.

It was recently proposed theoretically that arrays of misfit dislocations lead to a flat band of the topological surface states in TCI, which – due to a large magnitude of the resulting DOS and its spin structure – may show unconventional interfacial superconductivity[157]. Within this 2D model, ZBCPs would result from the Andreev reflection with conductance dips being modified by critical current heating[148]. The theory[157] was discussed in the context of superconductivity of IV-VI superlattices and heterostructures, whose interfaces host misfit dislocations that could then account for a global 2D superconductivity. Experimentally, however, the superconductivity appears in layered structures either comprising topological materials, e.g., PbTe/SnTe (ref. [158]) or not, e.g., PbSe/PbS (ref. [159]).

An array of dislocations can be mechanically generated during fixation of hard point-contacts. Also, owing to a difference in thermal expansion coefficients of silver paint and IV-VI crystals, a dislocation array could form underneath of the junction on cooling. However, the transport study presented in the Fig 4.11 do not show that, hypothetically, this takes place.

As already mentioned and detailed in the previous section, no indication of the Meissner effect is found in the case of samples of interest here, i.e., $Pb_{1-y}Sn_yTe$ with $y = 0.20$, 0.80, and 1. This means, taking our experimental resolution into account, that the relative weight of precipitations that could produce a response specific to superconducting Pb or Sn is below 0.1 ppm, apparently too low to show up in differential conductance spectra. This is consistent with the fact that the magnitudes of T_c and H_c we find for our samples (Fig. 4.4) do not match the values specific to Pb or Sn.

However, by SQUID magnetometry we cannot disprove entirely the presence of Pb- or Sn-related aggregates of a median diameter below 10 nm, in which dimensional quantization of electronic states diminishes T_c but enhances H_c and Δ (ref. [160, 161]). This would elucidate the origin of the observed larger values of the prefactor C than expected within the BCS theory in the weak coupling limit (Fig. 4.4b). Because of T_c dispersion and large H_c values, metallic quantum dots, even if numerous, might not show up in magnetic measurements. In contrast, they can affect point-contact conductance, as a large magnitude of DOS in metals and the virtual absence of Schottky barriers in paraelectric IV-VI compounds can result in an Andreev-type of spectra observed previously for In/PbTe junctions and assigned to (Pb,In)

alloy formation[132]. The nano-precipitation model would explain also instabilities of the differential conductance, as current paths may switch between metal grains differing in superconducting characteristics. Within this scenario, the conductance maximum around $V = 0$ is caused by Andreev reflection modified by confinement and local heating by the critical current and consequently form a pair of dips symmetric about V = 0, which may lead to an additional apparent enlargement of the prefactor C (ref. [148]). This model is also consistent with the disappearance of ZBCP in the case of the ferromagnetic Co or Ni tips employed as hard point contacts to $Pb_{0.6}Sn_{0.4}Te$ (ref. [19]). On the other hand, this work presents entirely new experimental evidence, that superconducting point contacts can be observed between the junctions of normal metal and a topological ferromagnet, which weakens the precipitates hypothesis considerably.

The scenario involving nanometer-size metal precipitates has further worthwhile implications. It may indicate that precipitates which often decorate dislocations account for conspicuous 2D global superconductivity with T_c up to 6.5 K in epitaxial superlattices and heterostructures of IV-VI compounds[158, 159]. A question also arises about the role of metallic precipitations in the case of superconductivity of $Pb_{1-x}Tl_xTe$ and $Sn_{1-x}In_xTe$, particularly considering that T_c of Pb is 7.2 K and of (In,Sn) may reach 6.6 K[162].

However, in our samples, neither high-resolution SQUID magnetometry (carried out for non-magnetic samples) nor high-resolution transmission electron microscopy (carried out for magnetic $Pb_{0.16}Sn_{0.74}Mn_{0.10}Te$, also in the vicinity of dislocations, as it will be shown in the next section) reveal superconducting metal precipitates. Similarly, no superconducting precipitates are detected by SQUID magnetometry of silver paint. Remarkably, the differential conductivity spectra reported here for TCI are virtually identical to those found for topological semimetals Cd_3As_2 and TaAs (ref. [20–23]), in which local T_c, as in our case, varies from junction to junction but reaches 13 K and, therefore, cannot be assigned to precipitates, as $T_c = 0.52$ and 4.48 K, for Cd and Ta, respectively.

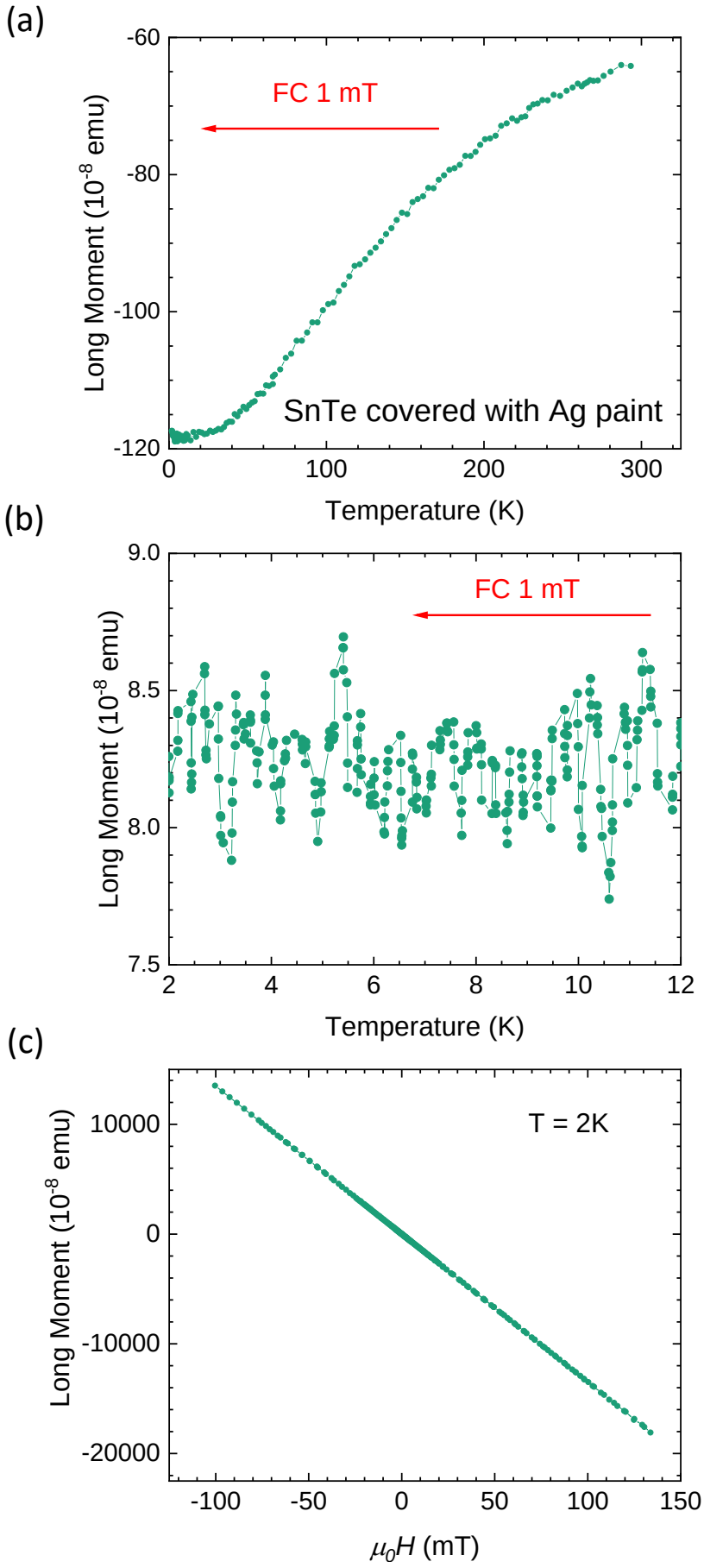

FIGURE 4.15: Search for superconducting precipitates in SnTe sample covered entirely by silver paint in an in-plane magnetic field. (a,b) Magnetic moment vs. temperature measured on cooling in a magnetic field of 1 mT. (c) Magnetization vs. magnetic field at 2 K showing diamagnetism of SnTe.

4.2.3 Search for precipitates by electron microscopy

Transmission electron microscope (TEM) investigations, whose results are presented in this section, are performed in a FEI Titan cube 80-300 aberration corrected microscope operating at 300 kV in TEM and scanning TEM modes at different camera lengths and with high-angle annular dark-field (HAADF) detector. The microscope operates at IP PAS in the Laboratory of x-ray and electron microscopy, the TEM characterization was carried out by Prof. Sawomir Kret. The lamellas for TEM investigations are prepared using dual beam FEI Helios Nanolab 600 system equipped with Omiprobe manipulator and platinum gas injection system. Selected area of the nanocrystal is capped first with 0.2 μm and later with 1 μm thick platinum layers deposited under 5 kV acceleration voltage and 2.7 pA current, and under 30 kV and 280 pA, using electron and Ga ion guns, respectively. The final thinning of the lamella is carried out with Ga ions at 2 kV and 28 pA resulting in the thickness of the specimen ranging between 50 to 150 nm. Figure 4.16(a) shows scanning electron microscopy (SEM) image of a lamella prepared of $Pb_{0.16}Sn_{0.74}Mn_{0:10}Te$ for transmission electron microscopy (TEM) studies. A $5 \times 2.5\,\mu$m defect-free area is presented in Fig. 4.16(b). The dark wavy features are due to lamella bending. The sharp feature seen at the bottom right corner is caused by mechanical deformation that occurred during the thinning process or by processing of the crystal during previous investigations. Structural defects (mainly small dislocation loops) can be found in some regions near the surface of the crystal - no deeper than 2 μm from the surface. No fluctuations of elemental composition or precipitations of other phases are detected. It appears that Pb and Mn atoms substitute the Sn atoms without ordering or segregation that could be detected within our sensitivity. The high-resolution TEM (HRTEM) image (Fig. 4.17) indicates a perfect cubic lattice visible in [110] zone axis. A quantitative profile of the crystal region containing structural defects (dislocations) near the surface zone obtained by energy dispersive x-ray spectroscopy (EDS) is presented in Fig. 4.18. No aggregation of particular constituents is detected, as composition fluctuations are within the error bar of the method. The determined atomic concentrations of the constituting elements are in good agreement with results of our SQUID measurements and specifications found in the previous characterization study[97]. In the next section I consider therefore two models of the local, collective low-temperature phase that could account for features observed in conductance spectroscopy in TCI, and possibly in other classes of topological materials.

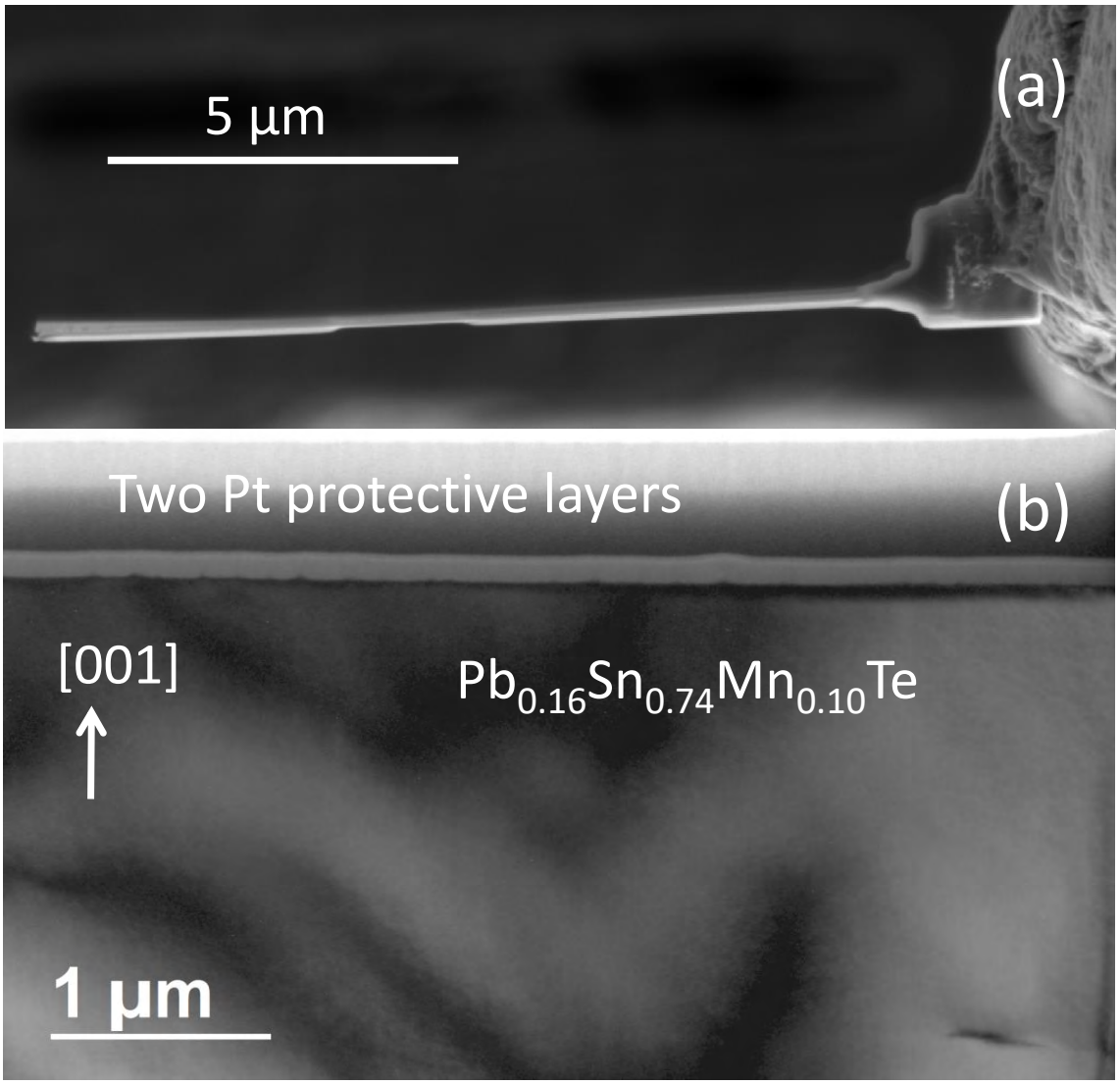

FIGURE 4.16: (a) Scanning electron microscope image of the edge of the lamella attached to the transmission electron microscope (TEM) copper support; (b) TEM bright field image of a defect-free 5×2.5 μm area of the specimen.

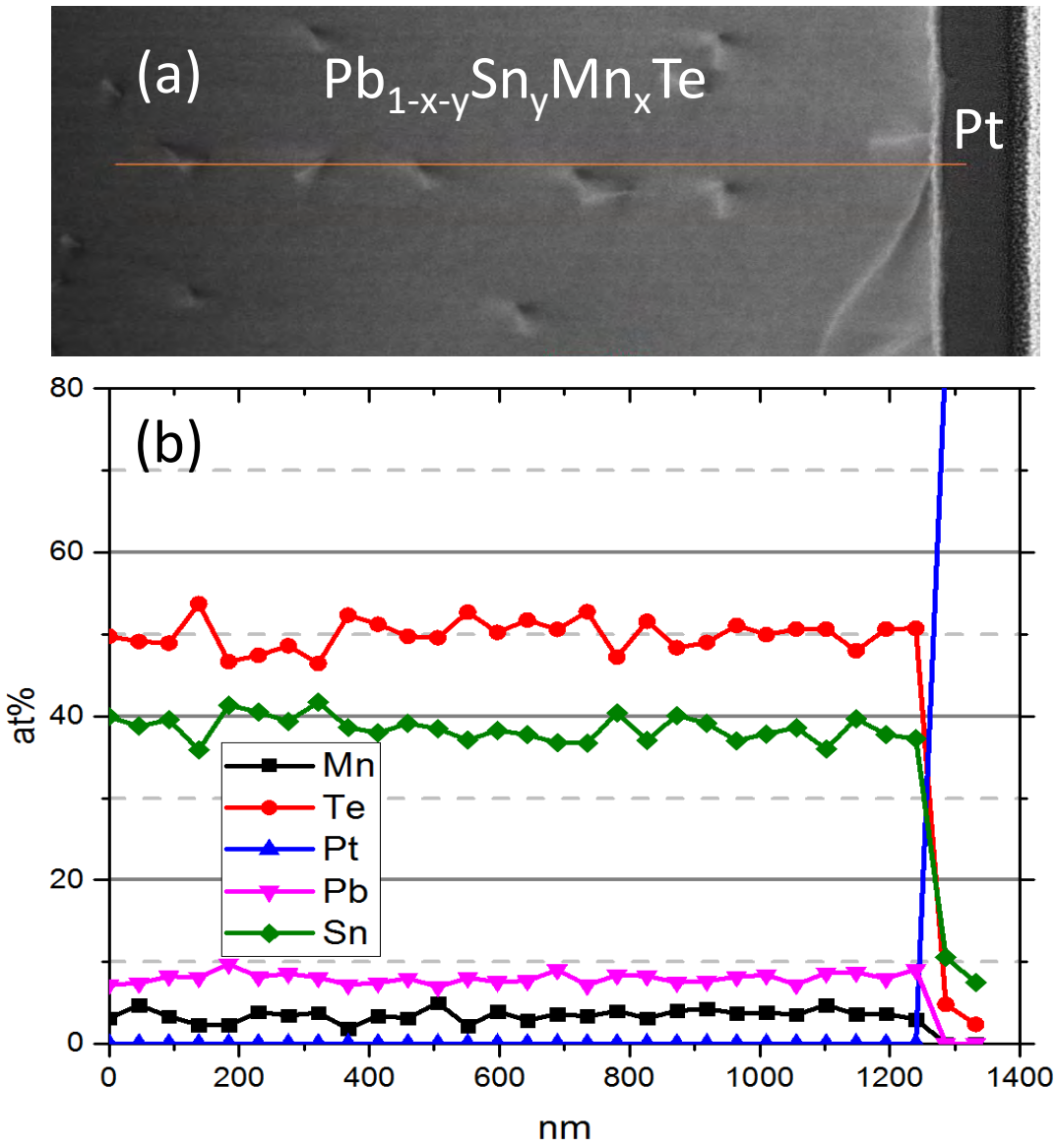

FIGURE 4.17: High-resolution transmission electron microscope image of zone axis (110) of $Pb_{0.16}Sn_{0.74}Mn_{0.10}Te$ crystal.

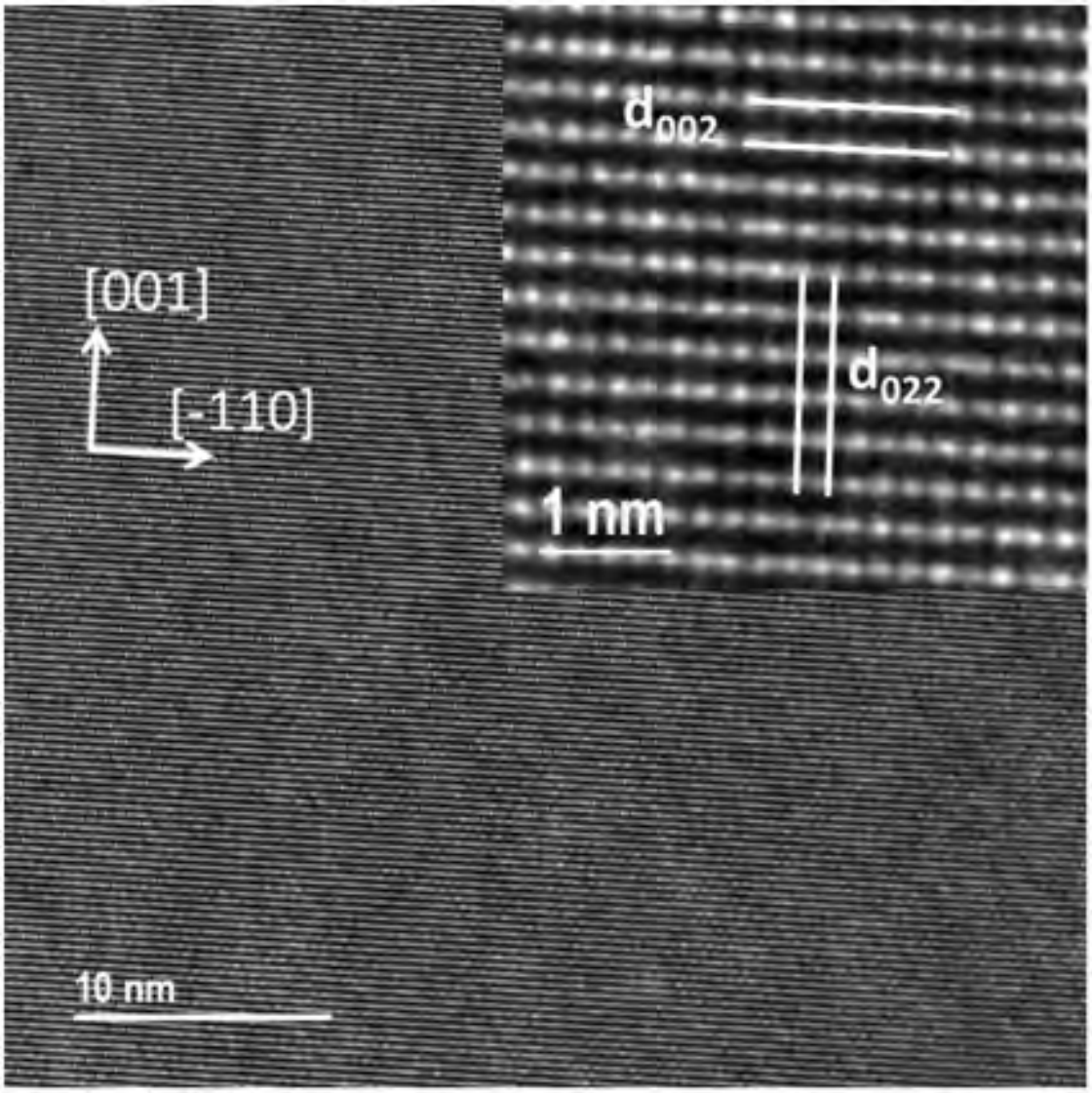

FIGURE 4.18: (a) STEM-HAADF (out of zone axis). (b) EDS elemental concentration profile of Sn, Pb, Te, Mn, Pt of the area with near-surface dislocations. Note that atomic, not cation, concentrations are shown.

4.2.4 Superconductivity at atomic surface steps

Recent scanning tunneling spectroscopy study revealed the presence of 1D topological states adjacent to odd atomic steps at (001) topological surfaces of (Pb,Sn)Se cleaved under high vacuum conditions[163]. Within one-electron picture, these 1D states form a rather flat helical band, connecting two surface Dirac cones in TCIs [163, 164]. Figure 4.20 presents surface morphol-

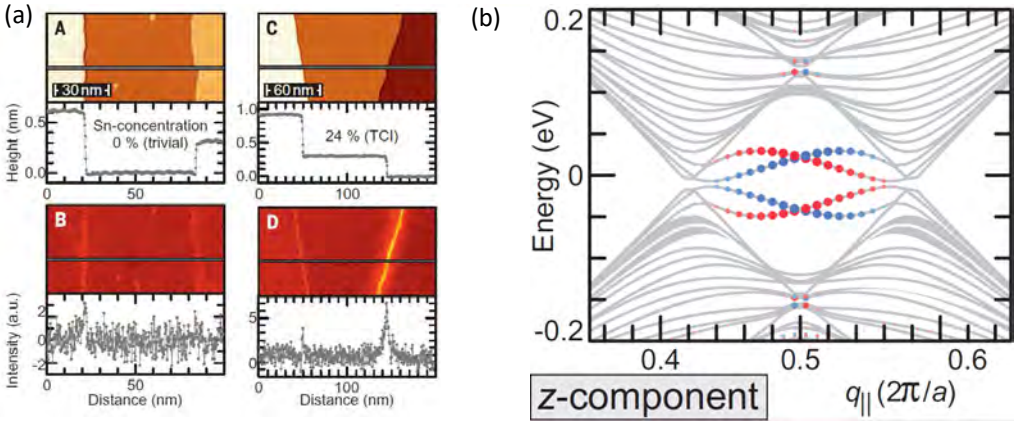

FIGURE 4.19: Enhanced density of states at the surface atomic step edges. Panel (a) illustrates morphology and density of states for crystals being in topologically trivial (A,B) and TCI phase (C,D). Panel (b) depicts dispersion relation of the states at the step edges. As appeared in the Ref [163].

ogy of our single crystals under ambient conditions, determined by atomic force microscopy (AFM). As seen in Figs. 4.20(a,b), (001) facets of as grown $Pb_{0.20}Sn_{0.80}Te$ contain atomically flat 0.5 μm wide terraces, terminated by monoatomic steps. Similarly, Figs. 4.20(c,d) visualize a (001) surface of cleaved $Pb_{0.16}Sn_{0.74}Mn_{0.10}Te$ showing larger roughness and multilayer steps. Results in Figs. 4.1(b,c) and 4.3(c) were actually taken for these two surfaces, respectively. The experimental evidence presented in this thesis suggests, that all the observed phenomenology comes from the 1D system. In such a system many types of long-range order may appear, provided that the states at the step edges are indeed occupied. Now possible scenarios related to this physical picture will be discussed.

The above interpretation requires the Fermi level of investigated p-type samples to reside within the 1D band, whereas tight-binding computations place the 1D band in the gap[163, 164]. There are, however, three effects that can affect considerably the position of 1D bands in respect to the Fermi energy. First, a considerable role is played by hybridization of states adjacent to

neighbouring steps[164]. Second, space charge effects associated with surface defect states and surface oxidation shift the position of topological surface states in respect to the Fermi level in TCI in question[65, 147, 165]. Moreover, in the case of 1D systems particularly relevant are correlation effects that might be crucial in accounting for the degree of the occupation of the 1D band and for the ground state of carriers residing in it.

Additionally, the experimental method employed here, implies the formation of Schottky's metal-semiconductor junction, which leads usually to the Fermi level pinning in the band gap region at the semiconductor surface [166]. The depletion in the bulk carrier density implies also that Mn spins adjacent to the surface will be rather coupled by antiferromagnetic superexchange [143] than by the hole-mediated ferromagnetic interactions dominating in the bulk [118]. This is also supported by the experimental evidence, as crossing the Curie point does not affect features observed in the point contact at all 4.4(b,c).

A competition between various ground states of carriers occupying 2D topological bands at surfaces of TCI has recently been examined theoretically. It has been concluded that a chiral p-wave superconducting order ($S_z = 0$) is favoured among other competing electronic instabilities[167]. This p-wave state is robust against moderately strong magnetization and in fact should be observed in magnetically doped IV-VI TCI compounds[168]. Such effects are expected to show up at even higher temperatures in the 1D case, for which Majorana quasiparticles are expected. Actually, chiral Majorana states that respect the particle-hole symmetry while break both the spin-rotational and time-reversal symmetries were predicted[169] and then observed at 1D edge states of ferromagnetic topological insulators proximitized by an s-type superconductor[149].

Since any bulk superconductivity is not observed, a pairing energy should originate from electron-phonon coupling and/or interactions within the 1D band[170]. In order to interpret the experimentally observed insensitivity of the local superconductivity to global ferromagnetism we note that carrier correlation may lead to a spontaneous breaking of spin-rotation symmetry by forming a ferromagnetic ground state, as already discussed theoretically in the context of one-mode IV-VI quantum wires[171], though the presence of spin-locking may affect the magnitude of the corresponding carrier Curie temperature. Moreover, in the 1D case, the exchange coupling to

Mn spins may stabilize the ferromagnetic order of carriers or spin-density waves formed by Peierls's instability at temperatures much higher than bulk T_{Curie} (ref. [172]),

$$T^{1\mathrm{D}}_{\mathrm{Curie}}/T_{\mathrm{Curie}} = \rho^{1\mathrm{D}}_{F}/\rho_{\mathrm{F}}A, \tag{4.4}$$

where $T^{1\mathrm{D}}_{\mathrm{Curie}}$ is much enhanced over T_{Curie} by both the Van Hove singularities in 1D DOS $\rho^{1\mathrm{D}}_{F}$ and spatial confinement, described by an effective cross-section area of the 1D channels, A, i.e., the inverse participation number. Hence, the ferromagnetism, along with the spin-orbit interaction, may result in triplet pairing and MBSs with lifted Kramers degeneracy, the interpretation explaining the increase of the local T_c with T_{Curie}, as seen in Fig. 4.4. Furthermore, within this model, differential conductance characteristics depend on the step heights and lengths as well as on the surface contamination, as observed. Actually, a distribution in T_c values, along with enlargement of C coming from the expected strong coupling effects, may enhance the prefactor C in the BCS formula (Fig. 4.4). At the same time, the lack of global superconductivity is understood, as a network of 1D channels is not expected to percolate. While having no control over interfacial transmission coefficients we cannot quantify a relative contribution of zero-energy states to ZBCPs from Andreev reflection or excitations like Majorana bound states. Also, insensitivity to the bulk ferromagnetism makes the superconducting step edges one of the possible explanations.

However, for a class of electronic instabilities, such as superconductivity and charge/spin density waves, the BCS relation between the gap 2Δ and the critical temperature T_c remains valid within the mean-field approximation. Still, because of the dominating role played by thermal and quantum fluctuations of the order parameter, the apparent magnitude of T_c becomes much reduced in the 1D case [170, 173]. This explains the enhanced magnitude of C over the BCS value (Fig. 4.4) but indicates also that 1D step edge states may not support superconductivity with T_c as high as 5 K.

4.2.5 Zero-bias anomalies without superconductivity.

Anomalies in differential conductance $\mathrm{d}I/\mathrm{d}V$ have been persistently observed near zero bias in tunneling junctions of two normal metals. These anomalies were initially interpreted in terms of the Appelbaum-Anderson theory, within which the presence of localized spins in the barrier or interfaces is postulated, and the anomalies explained by generalizing the Kondo theory

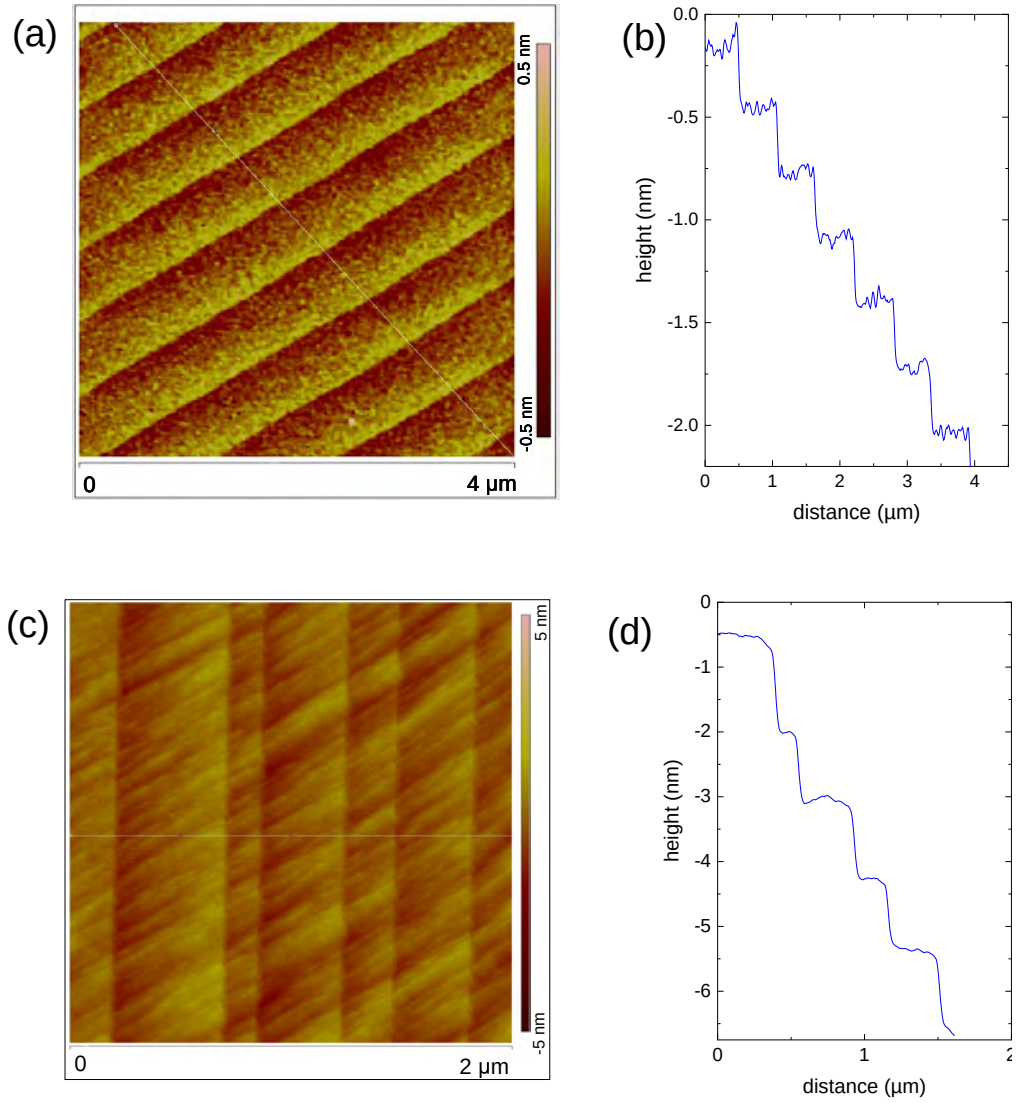

FIGURE 4.20: AFM images of the studied single crystal surfaces. (a) Naturally grown (001) facet of $Pb_{0.20}Sn_{0.80}Te$ showing surface steps. (c) Cleaved (001) surface of $Pb_{0.16}Sn_{0.74}Mn_{0.10}Te$ showing multilayer steps and higher roughness. Panels (b) and (d) depict step height profiles. The obtained values of about 0.3 nm in (b) correspond to a single atomic step (315 pm).

to the tunneling conductance[174, 175]. Later, Altshuler and Aaronov found that carrier correlations in disordered metals affect the density of states (DOS) around the Fermi level, which leads to a zero-bias anomaly without invoking any localized spins[176]. The modification of DOS found by Altshuler and Aronov evolves into the Efros-Shklovskii gap on the insulator side of the metal-to-insulator transition[177]. It has been found more recently that the Kondo effect results in a ZBCP superimposed onto the Coulomb gap in

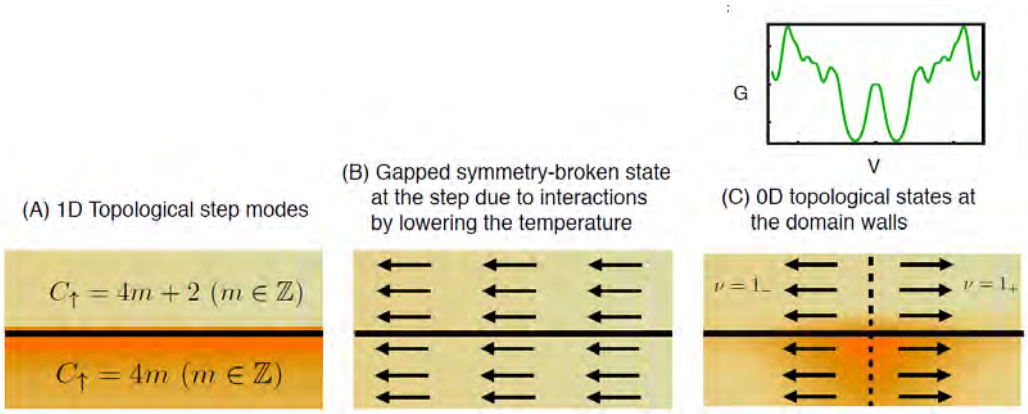

FIGURE 4.21: A sketch of BWH theory. (A) Topological step modes appearing at the boundary of two topologically non-trivial regions with different Chern number. (B) Appearance of gaped symmetry broken state driven by temperature lowering. (C) 0D topological states at the domain walls. Picture by a courtesy of T.Hyart.

spectra of electron tunneling across a quantum dot containing an even number of electrons[178, 179]. There is yet another alternative which may lead to observed spectroscopic features without invoking any superconductivity.

A possible origin of a local collective phase at topological surfaces has recently been proposed by Brzezicki, Wysokiński, and Hyart (BWH) [180], who noted that the electronic structure of one-dimensional (1D) states at atomic steps in TCIs, revealed by scanning tunneling microscopy [163, 181], is significantly richer than anticipated previously [163, 164, 181, 182]. According to BWH, these 1D states are prompt to a low-temperature Peierls-like instability leading to the appearance of low-energy excitations associated with topological states at domains walls of the collective phase. Within this new insight, effects of magnetic instabilities have been considered and the nature of low-energy excitations proposed [180]. In an analogy with the Su–Schreffer–Heeger model [183], the low-energy modes are associated with domain walls between the regions characterized by the opposite directions of the order parameter for which, as proven, topological invariants differ (see Fig 4.21). These walls, and thus, low energy excitations vanish in the magnetic field with a rate determined by a competition of the carrier-carrier exchange coupling with the Zeeman, spin-orbit, and sp–d exchange interactions. Depending on the assumed broadening, the evaluated conductance spectra show a single ZBCP, or a more complex peak structure that reflects the multi-mode excitation spectrum and may resemble the Andreev reflection [180].

Below, I outline all the theoretical explanations proposed to explain observed superconducting point contact phenomenology, as well as the appearance of zero-energy states.

Unconventional, low-dimensional superconductivity

This explanation had been put forward by all the works, done in the field of normal metal/topological material interface [19–23, 25, 26, 29, 145] . It can be summarized in the following points:

- Would naturally explain all the superconducting point contact phenomenology and robustness of the peak at zero bias (impossible to split the peak with magnetic field). The features observed in the point-contact experiments were always observed for junctions between normal metal and superconductors, and it is natural to assign this finding to the superconducting order.
- Requires existence of superconducting order, at interface, sample surface, or topologically non-trivial 1D objects. To date no direct signatures of superconductivity, like Meissner effect or 4-probe zero resistance states were observed.
- There is no microscopic model which would explain the pairing mechanism in such a broad family of materials. However, for the case of TCIs a 2D p-wave superconductivity has been analyzed theoretically[184].

Topological domain wall states

The plausible explanation of observed conductance spectra was just recently proposed by BWH as described in the previous section. This model is particularly appealing, as it does not involve any superconductivity which indeed was not observed experimentally. The main strengths and weaknesses of this model are:

- The explanation does not require superconductivity.
- Can be qualitatively explain all the parametric dependencies observed experimentally.
- For IV-VI based TCIs, the microscopic model is proposed.
- All the collected experimental evidence comes from the point-contact spectroscopy which lacks spatial resolution which is necessary for unambiguous proof of this model.

Trivial superconductivity from superconducting nanoinclusions

As mentioned many times throughout the thesis, the issue of superconducting precipitates should be very carefully addressed before any claim of new, collective low temperature phase is made. The main assumptions of the model are listed below:

- The main features of superconducting point-contact phenomenology could be explained.
- BCS like behavior of the gap would have very direct justification.
- It would naturally explain robustness of superconducting point contacts for topological materials with carrier density ranging from $10^{17}\ cm^{-3}$ to $10^{21}\ cm^{-3}$.

This explanation however also has some drawbacks:

- The work presented in this thesis, has denied the existence of superconducting nano-inclusions.
- Existence of such superconducting order is incompatible with the fact that magnetic impurities enhance the effect, or that the effect is observed equally well with a ferromagnetic electrode [19, 26].
- Not all the phenomenology observed in the conductance spectroscopy can be explained. For example zero-bias conductance peak should not coexist with gap features.

4.3 Conclusions

In this thesis, I studied magnetic and electrical transport properties of single crystals of diamagnetic, paramagnetic, and ferromagnetic $Pb_{1-y-x}Sn_yMn_xTe$. I have mainly focused on the junctions between normal metal (silver) and IV-VI semiconductor, which resembled characteristic of superconducting point contact, if a SnTe-based TCI is in the band inverted regime. For the first time, I have shown that this peculiar features are also seen for ferromagnetic materials. Below I listed all the important observations, which might help to understand physical nature of the peculiarities observed in the conductance spectroscopy of topological matter. These findings are pointing in the new research directions, which go beyond point-contact spectroscopy.

- From all the obtained spectra, I was able to extract the dependence of an energy gap as a function of field and temperature. Although the actual value of the gap might be affected by thermal effects, the energy gap shows a mean-field behavior.

- Despite the fact that several works on Normal Metal/Topological Insulator interface had been reported, results presented in this thesis show, for the first time, that magnetically doped topological material, resemble features characteristic for superconducting point contacts. Passing through the Curie temperature does not affect features obtained by the conductance spectroscopy, what may indicate that the Fermi level is pinned inside the gap.

- Thanks to the very well explored topological phase diagram of IV-VI based topological crystalline insulators, I was able to verify that trivial band structure is detrimental to the "superconducting-like" features obtained in the point contact spectroscopy.

- Transport and magnetization measurements rule out possibility of superconducting order originating from 3D bulk superconductivity or 2D superconducting interface.

- Recently STM measurements proved existence of 1D topological states propagating along odd atomic step edges having a flat dispersion. Although point contact spectroscopy lacks spatial resolution, one of the possible scenarios is that the step itself or interface between the edge and the metal drives new, exotic superconducting order, similarly to a flat band system realized recently in a twisted bilayer graphene[185].

- To date all the experiments were interpreted in terms of superconducting order, due to the striking similarity to superconducting point contacts. However, all the investigated systems and all the control experiments didn't reveal any other signatures characteristic for superconductors. It may be that order parameter emerging under the contact area is not superconducting and may originate from low-energy excitations residing at the domain walls between different topological phases.

- Finally the issue of superconducting precipitates and dislocations is addressed experimentally, for the first time in the context of the observed phenomenology. As all the topological materials reported so far have superconducting element as a constituent, it is necessary to address trivial reason which may explain observed features present in the spectra between normal metal and topological materials.

4.4 Future prospects

The zero-energy states observed in the point-contact spectroscopy studies of topological materials lacks microscopic mechanism which is experimentally supported, despite works like this thesis greatly explored its phenomenology. I propose several further studies which can be realized to better understand this fascinating phenomenon:

- Interface engineering: So far attention of the community was mostly focused on bulk single crystals, with point contacts made either by a silver paint or a tip. However if high quality epitaxial layers would be grown in the future, one could engineer an atomically sharp interface between topological materials and a metal, as it was done for Al/InAs nanowires. This experiments could help to understand what is the role of interface and its quality in the features observed by point contact spectroscopy

- Existence of enhanced density of states at atomic steps in IV-VI semiconductors has been unambigously proven by STM. However, there are still many questions regarding the actual physical properties of this topological states, like their surprising robustness against high magnetic field. A conductance measurements across the step edge is interesting experimental route, which should be taken to better understand their nature. This requires four-nano or microprobe measurements, and a material with Fermi level placed inside the bulk band gap, within the step-edge states.

Appendix A

Author's scientific achievements

A.1 Publications

A.1.1 Publications and preprints co-authored during PhD studies

1. Y. Li, M. Amado, T. Hyart, **G.P. Mazur**, V. Risinggård, T. Wagner, L. McKenzie Sell, G. Kimbell, J. Wunderlich, J. Linder, J. W. A. Robinson, "Competition between canted antiferromagnetic and spin-polarized quantum Hall states at $\nu = 0$ in graphene on a ferrimagnetic insulator", arXiv:1905.06866, 2019

2. S. Prucnal, V. Heera, R. Huebner, M. Wang, **G.P Mazur**, M.J. Grzybowski, X. Qin, Y. Yuan, M. Voelskow, W. Skorupa, L. Rebohle, M. Helm, M. Sawicki, S. Zhou, "Superconductivity in single-crystalline aluminum-and gallium-hyperdoped germanium." Physical Review Materials 3.5 : 054802 (2019).

3. K. Dybko, **G.P. Mazur**, W.Wokanowicz, M.Szot, P.Dziawa, J.Z. Domagala, M.Wiater, T.Wojtowicz, T. Story, "Probing spatial extent of topological surface states by weak antilocalization experiments", arXiv:1812.08711,2018

4. **G.P. Mazur**, K. Dybko, A. Szczerbakow, M. Zgirski, E. Lusakowska, S. Kret, J. Korczak, T. Story, M. Sawicki, T. Dietl, "Experimental search for the origin of zero-energy modes in topological materials", arXiv:1709.04000v2,2018

5. D. Sztenkiel, M. Foltyn, **G.P. Mazur**, R. Adhikari, K. Kosiel, K. Gas, M. Zgirski, R. Kruszka, R. Jakiela, Tian Li, A. Piotrowska, A. Bonanni, M. Sawicki, T. Dietl, "Stretching magnetism with an electric field in a nitride semiconductor", Nat. Commun. 7, 13232 (2016)
   Director award for the best scientific publication at the Institute of Physics, Polish Academy of Sciences.

A.1.2 Publications and preprints co-authored before PhD studies

1. **G.P. Mazur**, O.Zanotti, A.Sadowski, B.Mishra, W. Kluzniak, Oscillations of radiation-pressure supported tori, Monthly Notices of the Royal Astronomical Society 456 (3), 3245-3252, 2016

2. P.Bakala, K.Goluchová, G.Török, E.rámková, M.A.Abramowicz, F.H.Vincent, **G.P. Mazur**, Twin peak high-frequency quasi-periodic oscillations as a spectral imprint of dual oscillation modes of accretion tori, ASTRONOMY & ASTROPHYSICS 581, A35, 2015

3. F. H. Vincent, **G. P. Mazur**, O. Straub, M. A. Abramowicz, G. Torok, and P. Bakala,Spectral signatures of oscillating slender tori surrounding Kerr black holes,ASTRONOMY & ASTROPHYSICS 563, A109, 2014

4. P. Bakala, G. Torok, V. Karas, M. Dovciak, M. Wildner, D. Wzientek, E. Sramkova, M. Abramowicz, K. Goluchova, **G. P. Mazur**, F. H. Vincent, Power density spectra of modes of orbital motion in strongly curved spacetime: obtaining the observable signal, Monthly Notices of the Royal Astronomical Society 439 (2), 1933-1939, 2014

5. **G.P. Mazur**, F.H. Vincent, M. Johansson, E. Sramkova, P. Bakala, M.A. Abramowicz, Towards modelling quasi-periodic oscillations of microquasars with oscillating slender tori, ASTRONOMY & ASTROPHYSICS 554, A57, 2013

A.2 Oral Presentations

1. **G.P. Mazur**, K. Dybko, A. Szczerbakow, M. Zgirski, E. Łusakowska, S. Kret, J. Korczak, T. Story, M. Sawicki,T.Dietl
   "Experimental search for the origin of zero-energy modes in topological materials", Majorana modes and beyond, 26-27 Poland, Warsaw, 2019 - **Invited talk**

2. D. Sztenkiel, M. Foltyn, **G.P. Mazur**, R. Adhikari, K. Kosiel, K. Gas, M. Zgirski, R. Kruszka, R. Jakiela, Tian Li, A. Piotrowska, A. Bonanni, M. Sawicki, T. Dietl
   "Manipulation of magnetic anisotropy through piezoelectromagnetism in a magnetic semiconductor (Ga, Mn)N", Joint European Magnetic Symposia, 21-26 August, Glasgow, 2016 - **Contributed talk**

A.3 Poster Presentations

1. **G.P. Mazur**, K. Dybko, A. Szczerbakow, M. Zgirski, E. Łusakowska, S. Kret, J. Korczak, T. Story, M. Sawicki, T. Dietl, Majorana-like excitations in a ferromagnetic topological crystalline insulator, 10th International School and Conference on Physics and Applications of Spin Phenomena in Solids, August 05-09, 2018, Linz, Austria

2. **G.P. Mazur**, K. Dybko, A. Szczerbakow, M. Zgirski, E. Łusakowska, S. Kret, J. Korczak, T. Story, M. Sawicki, T. Dietl, Majorana-like excitations in a ferromagnetic topological crystalline insulator, 47 th Jaszowiec International School and Conference on the Physics of Semiconductors, June 16-22, 2018, Szczyrk, Polska **Best poster award**

3. **G.P. Mazur**, K. Dybko, A. Szczerbakow, M. Zgirski, E. Łusakowska, S. Kret, J. Korczak, T. Story, M. Sawicki, T. Dietl, Majorana-like excitations in a ferromagnetic topological crystalline insulator, Quantum Complex Matter, June 10-15, 2018, Rome, Italy **Best poster award**

4. **G.P. Mazur**, K. Dybko, A. Szczerbakow, M. Zgirski, E. Łusakowska, S. Kret, J. Korczak, T. Story, M. Sawicki, T. Dietl, Majorana-like excitations in a ferromagnetic topological crystalline insulator, 10 th Superconducting spintronics and Majorana physics symposium, March 15-16, 2018, Cambridge, UK

5. **G.P. Mazur**, K. Dybko, A. Szczerbakow, M. Zgirski, E. Łusakowska, S. Kret, J. Korczak, T. Story, M. Sawicki, T. Dietl, Majorana-like excitations in a ferromagnetic topological crystalline insulator, Age of Interface workshop, August 07-22, 2017, Mainz, Germany

6. Transport and magnetism at ferromagnetic-paramagnetic critical point in (Ga,Mn)As, **G.P. Mazur**, J. Sadowski, T.Story, T. Dietl, M. Sawicki. 46th International School & Conference on the Physics of Semiconductors Jaszowiec,June 17-23,Szczyrk, Poland 2017.

7. Transport and magnetism at ferromagnetic-paramagnetic critical point in (Ga,Mn)As, **G.P. Mazur**, J. Sadowski, T. Dietl, M. Sawicki. 45th International School & Conference on the Physics of Semiconductors Jaszowiec,June 18-24,Szczyrk, Poland 2016.

8. Transport and magnetism at ferromagnetic-paramagnetic critical point in (Ga,Mn)As, **G.P. Mazur**, J. Sadowski, T. Dietl, M. Sawicki. XXII International Summer School Nicolás Cabrera, June 11-16,July, Poland 2015.

A.4 Projects

1. PI of the project "Interplay of magnetization and electric current in dilute ferromagnetic semiconductors" - (PRELUDIUM 10) awarded by the Polish National Science Center (NCN).

2. Polish National Science Center (NCN) graduate fellowship - ETIUDA 5
   With the support of this scholarship I have spent 6 months in the group of Dr. J Robinson and M. Blamire at the Department of Materials Science and Metallurgy, University of Cambridge, UK.

Bibliography

[1] A. Yu. Kitaev. "Unpaired Majorana fermions in quantum wires". In: *Phys.-Usp.* 44 (2001), pp. 131 –136. DOI: 10.1070/1063-7869/44/10S/S29.

[2] Liang Fu and C. L. Kane. "Superconducting Proximity Effect and Majorana Fermions at the Surface of a Topological Insulator". In: *Phys. Rev. Lett.* 100 (2008), p. 096407. DOI: 10.1103/PhysRevLett.100.096407.

[3] J. Alicea. "New directions in the pursuit of Majorana fermions in solid state systems". In: *Rep. Prog. Phys.* 75 (2012), p. 076501. DOI: 10.1088/0034-4885/75/7/076501.

[4] R.M. Lutchyn et al. "Majorana zero modes in superconductorsemiconductor heterostructures". English. In: *Nature Reviews. Materials* 3 (May 2018), pp. 52–68. ISSN: 2058-8437. DOI: 10.1038/s41578-018-0003-1.

[5] Hao Zhang et al. "Quantized Majorana conductance". In: *Nature* 556.7699 (2018), p. 74. DOI: 10.1038/nature26142.

[6] F. Nichele et al. "Scaling of Majorana Zero-Bias Conductance Peaks". In: *Phys. Rev. Lett.* 119 (2017), p. 136803. DOI: 10.1103/PhysRevLett.119.136803.

[7] S. Nadj-Perge et al. "Observation of Majorana fermions in ferromagnetic atomic chains on a superconductor". In: *Science* 346 (2014), pp. 602–607. DOI: 10.1126/science.1259327.

[8] S. Kashiwaya et al. "Edge States of Sr_2RuO_4 Detected by In-Plane Tunneling Spectroscopy". In: *Phys. Rev. Lett.* 107 (2011), p. 077003. DOI: 10.1103/PhysRevLett.107.077003.

[9] Jin-Peng Xu et al. "Experimental Detection of a Majorana Mode in the core of a Magnetic Vortex inside a Topological Insulator-Superconductor $Bi_2Te_3/NbSe_2$ Heterostructure". In: *Phys. Rev. Lett.* 114 (2015), p. 017001. DOI: 10.1103/PhysRevLett.114.017001.

[10] N. Levy et al. "Experimental Evidence for *s*-Wave Pairing Symmetry in Superconducting $Cu_xBi_2Se_3$ Single Crystals Using a Scanning Tunneling Microscope". In: *Phys. Rev. Lett.* 110 (2013), p. 117001. DOI: 10.1103/PhysRevLett.110.117001.

[11] Su-Yang Xu et al. "Momentum-space imaging of Cooper pairing in a half-Dirac-gas topological superconductor". In: *Nat. Phys.* 10 (2014), 943â950. DOI: 10.1038/nphys3139.

[12] Satoshi Sasaki et al. "Topological Superconductivity in $Cu_xBi_2Se_3$". In: *Phys. Rev. Lett.* 107 (2011), p. 217001. DOI: 10.1103/PhysRevLett.107.217001.

[13] M. Sato and Y. Ando. "Topological superconductors: a review". In: *Rep. Prog. Phys.* 80 (2017), p. 076501. DOI: 10.1088/1361-6633/aa6ac7.

[14] K Matano et al. "Spin-rotation symmetry breaking in the superconducting state of $Cu_xBi_2Se_3$". In: *Nat. Phys.* (2016). DOI: 10.1038/nphys3781.

[15] Shingo Yonezawa et al. "Thermodynamic evidence for nematic superconductivity in $Cu_xBi_2Se_3$". In: *Nature Physics* (2017). DOI: 10.1038/nphys3907.

[16] S. Sasaki et al. "Odd-Parity Pairing and Topological Superconductivity in a Strongly Spin-Orbit Coupled Semiconductor". In: *Phys. Rev. Lett.* 109 (2012), p. 217004. DOI: 10.1103/PhysRevLett.109.217004.

[17] M. Novak et al. "Unusual nature of fully gapped superconductivity in In-doped SnTe". In: *Phys. Rev. B* 88 (2013), p. 140502. DOI: 10.1103/PhysRevB.88.140502.

[18] Yu. I. Gorina et al. "Two-band superconductivity of $Sn_{1-x}In_xTe$ crystals with T_c = 3.6–3.8 K". In: *Phys. Solid State* 59 (2017), pp. 1918–1925. DOI: 10.1134/S1063783417100171.

[19] Shekhar Das et al. "Unexpected superconductivity at nanoscale junctions made on the topological crystalline insulator $Pb_{0.6}Sn_{0.4}Te$". In: *Appl. Phys. Lett.* 109 (2016), p. 132601. DOI: 10.1063/1.4963698.

[20] L. Aggarwal et al. "Unconventional superconductivity at mesoscopic point contacts on the 3D Dirac semimetal Cd_3As_2". In: *Nat. Mater.* 15 (2016), pp. 32–37. DOI: 10.1038/nmat4455.

[21] He Wang et al. "Observation of superconductivity induced by a point contact on 3D Dirac semimetal Cd_3As_2 crystals". In: *Nat. Mater.* 15.1 (2016), p. 38. DOI: 10.1038/nmat4456.

[22] L. Aggarwal et al. "Mesoscopic superconductivity and high spin polarization coexisting at metallic point contacts on Weyl semimetal TaAs". In: *Nat. Commun.* 8 (2017), p. 13974. DOI: 10.1038/ncomms13974.

[23] He Wang et al. "Discovery of tip induced unconventional superconductivity on Weyl semimetal". In: *Sci. Bull.* 62 (2017), pp. 425 –430. DOI: 10.1016/j.scib.2017.02.009.

[24] Sungjae Cho et al. "Kondo-like zero-bias conductance anomaly in a three-dimensional topological insulator nanowire". In: *Sci. Rep.* 6 (2016), p. 21767. DOI: 10.1038/srep21767.

[25] Yurii Naidyuk et al. "Surface superconductivity in the Weyl semimetal $MoTe_2$ detected by point contact spectroscopy". In: *2D Materials* 5.4 (2018), p. 045014. DOI: 10.1088/2053-1583/aad3e2.

[26] WL Zhu et al. "Evidence of Interfacial Topological Superconductivity on the Topological Semimetal Tungsten Carbide Induced by Metal Deposition". In: *arXiv preprint arXiv:1811.12129* (2018).

[27] Lei Shan et al. "Superconductivity Induced at a Point Contact on the Topological Semimetal Tungsten Carbide". In: *arXiv preprint arXiv:1811.12213* (2018).

[28] Leena Aggarwal et al. "Tip-induced Superconductivity Coexisting with Preserved Topological Properties in Line-nodal Semimetal ZrSiS". In: *arXiv preprint arXiv:1802.07993* (2018).

[29] Yu G Naidyuk et al. "Yanson point-contact spectroscopy of Weyl semimetal WTe2". In: *arXiv preprint arXiv:1902.11037* (2019).

[30] V. Umansky et al. "MBE growth of ultra-low disorder 2DEG with mobility exceeding 35Œ106cm2/Vs". In: *Journal of Crystal Growth* 311.7 (2009). International Conference on Molecular Beam Epitaxy (MBE-XV), pp. 1658 –1661. ISSN: 0022-0248. DOI: https://doi.org/10.1016/j.jcrysgro.2008.09.151.

[31] J. P. Eisenstein et al. "Insulating and Fractional Quantum Hall States in the First Excited Landau Level". In: *Phys. Rev. Lett.* 88 (7 2002), p. 076801. DOI: 10.1103/PhysRevLett.88.076801.

[32] K. v. Klitzing, G. Dorda, and M. Pepper. "New Method for High-Accuracy Determination of the Fine-Structure Constant Based on Quantized Hall Resistance". In: *Phys. Rev. Lett.* 45 (6 1980), pp. 494–497. DOI: 10.1103/PhysRevLett.45.494.

[33] L Shubnikov and Wander Johannes de Haas. "Magnetische Widerstandsvergrösserung in Einkristallen von Wismut bei tiefen Temperaturen". In: *Comm. Phys. Lab. Univ. Leiden 207a* (1930).

[34] D. J. Thouless et al. "Quantized Hall Conductance in a Two-Dimensional Periodic Potential". In: *Phys. Rev. Lett.* 49 (6 1982), pp. 405–408. DOI: 10.1103/PhysRevLett.49.405.

[35] Yoichi Ando. "Topological Insulator Materials". In: *Journal of the Physical Society of Japan* 82.10 (2013), p. 102001. DOI: 10.7566/JPSJ.82.102001. eprint: https://doi.org/10.7566/JPSJ.82.102001.

[36] K. S. Novoselov et al. "Electric Field Effect in Atomically Thin Carbon Films". In: *Science* 306.5696 (2004), pp. 666–669. ISSN: 0036-8075. DOI: 10.1126/science.1102896. eprint: http://science.sciencemag.org/content/306/5696/666.full.pdf.

[37] K. S. Novoselov et al. "Room-Temperature Quantum Hall Effect in Graphene". In: *Science* 315.5817 (2007), pp. 1379–1379. ISSN: 0036-8075. DOI: 10.1126/science.1137201. eprint: http://science.sciencemag.org/content/315/5817/1379.full.pdf.

[38] C. L. Kane and E. J. Mele. "Quantum Spin Hall Effect in Graphene". In: *Phys. Rev. Lett.* 95 (22 2005), p. 226801. DOI: 10.1103/PhysRevLett.95.226801.

[39] C. L. Kane and E. J. Mele. "Z_2 Topological Order and the Quantum Spin Hall Effect". In: *Phys. Rev. Lett.* 95 (14 2005), p. 146802. DOI: 10.1103/PhysRevLett.95.146802.

[40] B. Andrei Bernevig, Taylor L. Hughes, and Shou-Cheng Zhang. "Quantum Spin Hall Effect and Topological Phase Transition in HgTe Quantum Wells". In: *Science* 314 (2006), p. 1757.

[41] R. Piotrzkowski et al. "Band Structure of HgTe". In: *physica status solidi (b)* 8.3 (1965), K135–K139. DOI: 10.1002/pssb.19650080333. eprint: https://onlinelibrary.wiley.com/doi/pdf/10.1002/pssb.19650080333.

[42] Markus König et al. "Quantum Spin Hall Insulator State in HgTe Quantum Wells". In: *Science* 318.5851 (2007), pp. 766–770. ISSN: 0036-8075. DOI: 10.1126/science.1148047. eprint: http://science.sciencemag.org/content/318/5851/766.full.pdf.

[43] Joseph Maciejko et al. "Kondo Effect in the Helical Edge Liquid of the Quantum Spin Hall State". In: *Phys. Rev. Lett.* 102 (25 2009), p. 256803. DOI: 10.1103/PhysRevLett.102.256803.

[44] Jukka I. Väyrynen, Moshe Goldstein, and Leonid I. Glazman. "Helical Edge Resistance Introduced by Charge Puddles". In: *Phys. Rev. Lett.* 110 (21 2013), p. 216402. DOI: 10.1103/PhysRevLett.110.216402.

[45] Jukka I. Väyrynen et al. "Resistance of helical edges formed in a semiconductor heterostructure". In: *Phys. Rev. B* 90 (11 2014), p. 115309. DOI: 10.1103/PhysRevB.90.115309.

[46] Jukka I. Väyrynen, Dmitry I. Pikulin, and Jason Alicea. "Noise-Induced Backscattering in a Quantum Spin Hall Edge". In: *Phys. Rev. Lett.* 121 (10 2018), p. 106601. DOI: 10.1103/PhysRevLett.121.106601.

[47] Pietro Novelli et al. "Failure of Conductance Quantization in Two-Dimensional Topological Insulators due to Nonmagnetic Impurities". In: *Phys. Rev. Lett.* 122 (1 2019), p. 016601. DOI: 10.1103/PhysRevLett.122.016601.

[48] Andreas Roth et al. "Nonlocal Transport in the Quantum Spin Hall State". In: *Science* 325.5938 (2009), pp. 294–297. ISSN: 0036-8075. DOI: 10.1126/science.1174736. eprint: http://science.sciencemag.org/content/325/5938/294.full.pdf.

[49] Katja C Nowack et al. "Imaging currents in HgTe quantum wells in the quantum spin Hall regime". In: *Nature materials* 12.9 (2013), p. 787.

[50] Chaoxing Liu et al. "Quantum Spin Hall Effect in Inverted Type-II Semiconductors". In: *Phys. Rev. Lett.* 100 (23 2008), p. 236601. DOI: 10.1103/PhysRevLett.100.236601.

[51] Ivan Knez, Rui-Rui Du, and Gerard Sullivan. "Evidence for Helical Edge Modes in Inverted InAs/GaSb Quantum Wells". In: *Phys. Rev. Lett.* 107 (13 2011), p. 136603. DOI: 10.1103/PhysRevLett.107.136603.

[52] Fabrizio Nichele et al. "Edge transport in the trivial phase of InAs/GaSb". In: *New Journal of Physics* 18.8 (2016), p. 083005. DOI: 10.1088/1367-2630/18/8/083005.

[53] Sanfeng Wu et al. "Observation of the quantum spin Hall effect up to 100 kelvin in a monolayer crystal". In: *Science* 359.6371 (2018), pp. 76–79. ISSN: 0036-8075. DOI: 10.1126/science.aan6003. eprint: http://science.sciencemag.org/content/359/6371/76.full.pdf.

[54] Shujie Tang et al. "Quantum spin Hall state in monolayer 1T'-WTe 2". In: *Nature Physics* 13.7 (2017), p. 683.

[55] Zaiyao Fei et al. "Edge conduction in monolayer WTe 2". In: *Nature Physics* 13.7 (2017), p. 677.

[56] M. Z. Hasan and C. L. Kane. "Colloquium: Topological insulators". In: *Rev. Mod. Phys.* 82 (4 2010), pp. 3045–3067. DOI: 10.1103/RevModPhys.82.3045.

[57] David Hsieh et al. "A topological Dirac insulator in a quantum spin Hall phase". In: *Nature* 452.7190 (2008), p. 970.

[58] Yuqi Xia et al. "Observation of a large-gap topological-insulator class with a single Dirac cone on the surface". In: *Nature physics* 5.6 (2009), p. 398.

[59] David Hsieh et al. "A tunable topological insulator in the spin helical Dirac transport regime". In: *Nature* 460.7259 (2009), p. 1101.

[60] Yoichi Ando and Liang Fu. "Topological Crystalline Insulators and Topological Superconductors: From Concepts to Materials". In: *Annual Review of Condensed Matter Physics* 6.1 (2015), pp. 361–381. DOI: 10.1146/annurev-conmatphys-031214-014501. eprint: https://doi.org/10.1146/annurev-conmatphys-031214-014501.

[61] Liang Fu. "Topological Crystalline Insulators". In: *Phys. Rev. Lett.* 106 (10 2011), p. 106802. DOI: 10.1103/PhysRevLett.106.106802.

[62] Jeffrey C. Y. Teo, Liang Fu, and C. L. Kane. "Surface states and topological invariants in three-dimensional topological insulators: Application to $Bi_{1-x}Sb_x$". In: *Phys. Rev. B* 78 (4 2008), p. 045426. DOI: 10.1103/PhysRevB.78.045426.

[63] Timothy H. Hsieh et al. "Topological crystalline insulators in the SnTe material class". In: *Nat. Commun.* 3 (2012), p. 982. DOI: 10.1038/ncomms1969.

[64] P. Dziawa et al. "Topological crystalline insulator states in $Pb_{1-x}Sn_xSe$". In: *Nat. Mater.* 11 (2012), pp. 1023–1027. DOI: 10.1038/nmat3449.

[65] Y. Tanaka et al. "Experimental realization of a topological crystalline insulator in SnTe". In: *Nat. Phys.* 8 (2012), pp. 800–803. DOI: 10.1038/nphys2442.

[66] Su-Yang Xu et al. "Observation of a topological crystalline insulator phase and topological phase transition in $Pb_{1-x}Sn_xTe$". In: *Nat. Commun.* 3 (2012), p. 1192. DOI: 10.1038/ncomms2191.

[67] Bastian M Wojek et al. "Direct observation and temperature control of the surface Dirac gap in a topological crystalline insulator". In: *Nature communications* 6 (2015), p. 8463.

[68] B. A. Assaf et al. "Quantum coherent transport in SnTe topological crystalline insulator thin films". In: *Applied Physics Letters* 105.10 (2014), p. 102108. DOI: 10.1063/1.4895456. eprint: https://doi.org/10.1063/1.4895456.

[69] A. A. Taskin et al. "Topological surface transport in epitaxial SnTe thin films grown on Bi_2Te_3". In: *Phys. Rev. B* 89 (12 2014), p. 121302. DOI: 10.1103/PhysRevB.89.121302.

[70] Ryo Ishikawa et al. "Thin film growth of a topological crystal insulator SnTe on the CdTe (111) surface by molecular beam epitaxy". In: *Journal of Crystal Growth* 453 (2016), pp. 124 –129. ISSN: 0022-0248. DOI: https://doi.org/10.1016/j.jcrysgro.2016.08.027.

[71] Hua Guo et al. "Topological crystalline insulator PbxSn1-xTe thin films on SrTiO3 (001) with tunable Fermi levels". In: *APL Materials* 2.5 (2014), p. 056106. DOI: 10.1063/1.4876637.

[72] Chen-Hui Yan et al. "Growth of topological crystalline insulator SnTe thin films on Si(111) substrate by molecular beam epitaxy". In: *Surface Science* 621 (2014), pp. 104 –108. ISSN: 0039-6028. DOI: https://doi.org/10.1016/j.susc.2013.11.004.

[73] Bing Cheng et al. "Magnetoterahertz Response and Faraday Rotation from Massive Dirac Fermions in the Topological Crystalline Insulator $Pb_{0.5}Sn_{0.5}Te$". In: *Phys. Rev. Lett.* 122 (9 2019), p. 097401. DOI: 10.1103/PhysRevLett.122.097401.

[74] Yoshinori Okada et al. "Observation of Dirac Node Formation and Mass Acquisition in a Topological Crystalline Insulator". In: *Science* 341.6153 (2013), pp. 1496–1499. ISSN: 0036-8075. DOI: 10.1126/science.1239451.

[75] Shinobu Hikami, Anatoly I. Larkin, and Yosuke Nagaoka. "Spin-Orbit Interaction and Magnetoresistance in the Two Dimensional Random System". In: *Progress of Theoretical Physics* 63.2 (1980), pp. 707–710. DOI: 10.1143/PTP.63.707.

[76] H. Steinberg et al. "Electrically tunable surface-to-bulk coherent coupling in topological insulator thin films". In: *Phys. Rev. B* 84 (23 2011), p. 233101. DOI: 10.1103/PhysRevB.84.233101.

[77] J. Chen et al. "Tunable surface conductivity in Bi_2Se_3 revealed in diffusive electron transport". In: *Phys. Rev. B* 83 (24 2011), p. 241304. DOI: 10.1103/PhysRevB.83.241304.

[78] Yong Seung Kim et al. "Thickness-dependent bulk properties and weak antilocalization effect in topological insulator Bi_2Se_3". In: *Phys. Rev. B* 84 (7 2011), p. 073109. DOI: 10.1103/PhysRevB.84.073109.

[79] A. A. Taskin et al. "Manifestation of Topological Protection in Transport Properties of Epitaxial Bi_2Se_3 Thin Films". In: *Phys. Rev. Lett.* 109 (6 2012), p. 066803. DOI: 10.1103/PhysRevLett.109.066803.

[80] K Dybko et al. "Probing spatial extent of topological surface states by weak antilocalization experiments". In: *arXiv preprint arXiv:1812.08711* (2018).

[81] G. Tkachov and E. M. Hankiewicz. "Weak antilocalization in HgTe quantum wells and topological surface states: Massive versus massless Dirac fermions". In: *Phys. Rev. B* 84.3 (2011), p. 035444. ISSN: 1098-0121. DOI: 10.1103/PhysRevB.84.035444.

[82] Yi Zhang et al. "Crossover of the three-dimensional topological insulator Bi 2 Se 3 to the two-dimensional limit". In: *Nature Physics* 6.8 (2010), p. 584.

[83] H. P. R. Frederikse and W. R. Hosler. "GALVANOMAGNETIC EFFECTS IN n-TYPE InSb AT 4.2ř K." In: *Canadian Journal of Physics* 34.12A (1956), pp. 1377–1378. DOI: 10.1139/p56-153.

[84] K. Dybko et al. "Experimental evidence for topological surface states wrapping around a bulk SnTe crystal". In: *Phys. Rev. B* 96 (20 2017), p. 205129. DOI: 10.1103/PhysRevB.96.205129.

[85] G. P. Mikitik and Yu. V. Sharlai. "Manifestation of Berry's Phase in Metal Physics". In: *Phys. Rev. Lett.* 82 (10 1999), pp. 2147–2150. DOI: 10.1103/PhysRevLett.82.2147.

[86] D. Shoenberg. *Magnetic Oscillations in Metals*. Cambridge Monographs on Physics. Cambridge University Press, 1984. DOI: 10.1017/CBO9780511897870.

[87] A. K. Okazaki et al. "Shubnikov–de Haas oscillations in topological crystalline insulator SnTe(111) epitaxial films". In: *Phys. Rev. B* 98 (19 2018), p. 195136. DOI: 10.1103/PhysRevB.98.195136.

[88] Chen Fang, Matthew J. Gilbert, and B Andrei Bernevig. "Large-Chern-Number Quantum Anomalous Hall Effect in Thin-Film Topological Crystalline Insulators". In: *Phys. Rev. Lett.* 112 (4 2014), p. 046801. DOI: 10.1103/PhysRevLett.112.046801.

[89] Chengwang Niu et al. "Topological crystalline insulator and quantum anomalous Hall states in IV-VI-based monolayers and their quantum wells". In: *Phys. Rev. B* 91 (20 2015), p. 201401. DOI: 10.1103/PhysRevB.91.201401.

[90] B. A. Assaf et al. "Inducing magnetism onto the surface of a topological crystalline insulator". In: *Phys. Rev. B* 91 (19 2015), p. 195310. DOI: 10.1103/PhysRevB.91.195310.

[91] S Safaei et al. "Quantum spin Hall effect in IV-VI topological crystalline insulators". In: *New Journal of Physics* 17.6 (2015), p. 063041. DOI: 10.1088/1367-2630/17/6/063041.

[92] Junwei Liu and Liang Fu. "Electrically tunable quantum spin Hall state in topological crystalline insulator thin films". In: *Phys. Rev. B* 91 (8 2015), p. 081407. DOI: 10.1103/PhysRevB.91.081407.

[93] Junwei Liu et al. "Spin-filtered edge states with an electrically tunable gap in a two-dimensional topological crystalline insulator". In: *Nature materials* 13.2 (2014), p. 178. DOI: https://doi.org/10.1038/nmat3828.

[94] G. Grabecki et al. "PbTeA new medium for quantum ballistic devices". In: *Physica E: Low-dimensional Systems and Nanostructures* 34.1 (2006), pp. 560 –563. ISSN: 1386-9477. DOI: https://doi.org/10.1016/j.physe.2006.03.100.

[95] V. A. Chitta et al. "Multivalley transport and the integer quantum Hall effect in a PbTe quantum well". In: *Phys. Rev. B* 72 (19 2005), p. 195326. DOI: 10.1103/PhysRevB.72.195326.

[96] N Kh Abrikosov. *Semiconducting II–VI, IV–VI, and V–VI Compounds*. Springer, 2013.

[97] S. Miotkowska et al. "Solubility limit of Mn in the semimagnetic semiconductor $Pb_{1-x-y}Sn_xMn_yTe$". In: *J. Cryst. Growth* 172.3 (1997), pp. 455 –458. DOI: 10.1016/S0022-0248(96)00753-1.

[98] J. O. Dimmock, I. Melngailis, and A. J. Strauss. "Band Structure and Laser Action in $Pb_xSn_{1-x}Te$". In: *Phys. Rev. Lett.* 16 (26 1966), pp. 1193–1196. DOI: 10.1103/PhysRevLett.16.1193.

[99] M.P. Mathur et al. "Superconductivity as a function of carrier density and magnetic spin concentration in the SnTe-MnTe system". In: *Journal of Physics and Chemistry of Solids* 34.2 (1973), pp. 183 –188. ISSN: 0022-3697. DOI: https://doi.org/10.1016/0022-3697(73)90075-9.

[100] Louis A. Hemstreet. "Cluster calculations of the effects of single vacancies of the electronic properties of PbS". In: *Phys. Rev. B* 11 (6 1975), pp. 2260–2270. DOI: 10.1103/PhysRevB.11.2260.

[101] GW Prat. "Vacancy and Interstitial States in the Lead Salts". In: *J. Nonmetals* 1 (1973), p. 103.

[102] Nelson J. Parada and George W. Pratt. "New Model for Vacancy States in PbTe". In: *Phys. Rev. Lett.* 22 (5 1969), pp. 180–182. DOI: 10.1103/PhysRevLett.22.180.

[103] RR Galazka and J Kossut. "Narrow Gap Semiconductors: Physics and Applications". In: *Lecture Notes in Physics Series (Springer, Berlin, 1980)* 133 (1980), p. 18.

[104] Tomasz Dietl and Hideo Ohno. "Dilute ferromagnetic semiconductors: Physics and spintronic structures". In: *Rev. Mod. Phys.* 86 (1 2014), pp. 187–251. DOI: 10.1103/RevModPhys.86.187.

[105] J. K. Furdyna. "Diluted magnetic semiconductors". In: *Journal of Applied Physics* 64.4 (1988), R29–R64. DOI: 10.1063/1.341700. eprint: https://doi.org/10.1063/1.341700.

[106] M. A. Ruderman and C. Kittel. "Indirect Exchange Coupling of Nuclear Magnetic Moments by Conduction Electrons". In: *Phys. Rev.* 96 (1 1954), pp. 99–102. DOI: 10.1103/PhysRev.96.99.

[107] Kei Yosida. "Magnetic Properties of Cu-Mn Alloys". In: *Phys. Rev.* 106 (5 1957), pp. 893–898. DOI: 10.1103/PhysRev.106.893.

[108] Tadao Kasuya. "A Theory of Metallic Ferro- and Antiferromagnetism on Zener's Model". In: *Progress of Theoretical Physics* 16.1 (July 1956), pp. 45–57. ISSN: 0033-068X. DOI: 10.1143/PTP.16.45.

[109] H. Ohno et al. "(Ga,Mn)As: A new diluted magnetic semiconductor based on GaAs". In: *Applied Physics Letters* 69.3 (1996), pp. 363–365. DOI: 10.1063/1.118061.

[110] C. Zener. "Interaction Between the *d* Shells in the Transition Metals". In: *Phys. Rev.* 81 (3 1951), pp. 440–444. DOI: 10.1103/PhysRev.81.440.

[111] H. Ohno et al. "Spontaneous splitting of ferromagnetic (Ga, Mn)As valence band observed by resonant tunneling spectroscopy". In: *Applied Physics Letters* 73.3 (1998), pp. 363–365. DOI: 10.1063/1.121835. eprint: https://doi.org/10.1063/1.121835.

[112] T. Dietl, H. Ohno, and F. Matsukura. "Hole-mediated ferromagnetism in tetrahedrally coordinated semiconductors". In: *Phys. Rev. B* 63 (2001), p. 195205. DOI: 10.1103/PhysRevB.63.195205.

[113] Tomasz Dietl et al. "Zener model description of ferromagnetism in zinc-blende magnetic semiconductors". In: *science* 287.5455 (2000), pp. 1019–1022. DOI: 10.1126/science.287.5455.1019.

[114] M. Sawicki et al. "In-plane uniaxial anisotropy rotations in (Ga,Mn)As thin films". In: *Phys. Rev. B* 71 (12 2005), p. 121302. DOI: 10.1103/PhysRevB.71.121302.

[115] Tomasz Dietl. "A ten-year perspective on dilute magnetic semiconductors and oxides". In: *Nature materials* 9.12 (2010), p. 965. DOI: https://doi.org/10.1038/nmat2898.

[116] G Bauer, H Pascher, and W Zawadzki. "Magneto-optical properties of semimagnetic lead chalcogenides". In: *Semiconductor Science and Technology* 7.6 (1992), pp. 703–723. DOI: 10.1088/0268-1242/7/6/001.

[117] M. Escorne et al. "Magnetic and transport properties of $Pb_{1-x}Mn_xTe$ spin-glass". In: *Phys. Rev. B* 29 (11 1984), pp. 6306–6318. DOI: 10.1103/PhysRevB.29.6306.

[118] T. Story et al. "Carrier-concentration-induced ferromagnetism in PbSnMnTe". In: *Phys. Rev. Lett.* 56 (1986), pp. 777–779. DOI: 10.1103/PhysRevLett.56.777.

[119] H. J. M. Swagten et al. "Hole density and composition dependence of ferromagnetic ordering in Pb-Sn-Mn-Te". In: *Phys. Rev. B* 37 (1988), pp. 9907–9910. DOI: 10.1103/PhysRevB.37.9907.

[120] T Story et al. "Compositional dependence of the band structure and magnetic properties of PbSnMnTe narrow-gap semimagnetic semiconductor". In: *Semiconductor Science and Technology* 5.3S (1990), S138–S140. DOI: 10.1088/0268-1242/5/3s/030.

[121] M. Ocio. "Hall coefficient and mobility in $Pb_{1-x}Sn_x$ Te with high carrier densities". In: *Phys. Rev. B* 10 (10 1974), pp. 4274–4283. DOI: 10.1103/PhysRevB.10.4274.

[122] P. Lazarczyk et al. "Magnetic phase diagram of Pb1xySnyMnxTe semimagnetic semiconductors". In: *Journal of Magnetism and Magnetic Materials* 169.1 (1997), pp. 151 –158. ISSN: 0304-8853. DOI: https://doi.org/10.1016/S0304-8853(96)00720-2.

[123] Tomasz Story. "Electron and spin properties of topological crystalline insulator (Pb, Sn) Se". In: *Bulletin of the American Physical Society* 60 (2015). DOI: http://meetings.aps.org/link/BAPS.2015.MAR.M7.1.

[124] R. S. Gonnelli et al. "Direct Evidence for Two-Band Superconductivity in MgB_2 Single Crystals from Directional Point-Contact Spectroscopy in Magnetic Fields". In: *Phys. Rev. Lett.* 89 (24 2002), p. 247004. DOI: 10.1103/PhysRevLett.89.247004.

[125] Andrei Vladimirovich Khotkevich and Igor K Yanson. *Atlas of point contact spectra of electron-phonon interactions in metals*. Springer Science & Business Media, 2013.

[126] D Daghero and R S Gonnelli. "Probing multiband superconductivity by point-contact spectroscopy". In: *Supercond. Sci. Technol.* 23.4 (2010), p. 043001. DOI: 10.1088/0953-2048/23/4/043001. eprint: 0912.4858.

[127] A M Duif, A G M Jansen, and P Wyder. "Point-contact spectroscopy". In: *Journal of Physics: Condensed Matter* 1.20 (1989), pp. 3157–3189. DOI: 10.1088/0953-8984/1/20/001.

[128] V Baltz et al. "Conductance features in point contact Andreev reflection spectra". In: *Journal of Physics: Condensed Matter* 21.9 (2009), p. 095701. DOI: 10.1088/0953-8984/21/9/095701.

[129] D Sztenkiel et al. "Stretching magnetism with an electric field in a nitride semiconductor". In: *Nature communications* 7 (2016), p. 13232.

[130] B. A. Assaf et al. "Modified electrical transport probe design for standard magnetometer". In: *Review of Scientific Instruments* 83.3 (2012), p. 033904. DOI: 10.1063/1.3697998.

[131] Olli V Lounasmaa. *Experimental principles and methods below 1K*. Academic Press, 1974.

[132] G. Grabecki et al. "Contact superconductivity in In-PbTe junctions". In: *J. Appl. Phys.* 108 (2010), p. 053714. DOI: 10.1063/1.3475692.

[133] R.F. Brebrick. "Non-stoichiometry in binary semiconductor compounds, M12N12+ (c)". In: *Progress in Solid State Chemistry* 3 (1967), pp. 213 – 264. ISSN: 0079-6786. DOI: https://doi.org/10.1016/0079-6786(67)90035-0.

[134] Andrzej Szczerbakow and Ken Durose. "Self-selecting vapour growth of bulk crystals Principles and applicability". In: *Progress in Crystal Growth and Characterization of Materials* 51.1 (2005), pp. 81 –108. ISSN: 0960-8974. DOI: https://doi.org/10.1016/j.pcrysgrow.2005.10.004.

[135] Escorne, M. and Mauger, A. "Magnetic order effects on electric susceptibility hole mass of Sn1-x MnxTe". In: *J. Phys. France* 40.4 (1979), pp. 347–354. DOI: 10.1051/jphys:01979004004034700.

[136] U Sondermann. "Magnetische untersuchungen an mischkristallen der quasibinären legierungssysteme (Cd Te)1-x (Mn Te)x und (Sn Te)1-x (Mn Te)x". In: *Journal of Magnetism and Magnetic Materials* 2.1 (1975), pp. 216 –222. ISSN: 0304-8853. DOI: https://doi.org/10.1016/0304-8853(75)90125-0.

[137] M. Escorne and A. Mauger. "Transport properties of Sn1xMnxTe at low magnetic field". In: *Solid State Communications* 31.11 (1979), pp. 893 –895. ISSN: 0038-1098. DOI: https://doi.org/10.1016/0038-1098(79)90412-5.

[138] M. Brando et al. "Metallic quantum ferromagnets". In: *Rev. Mod. Phys.* 88 (2 2016), p. 025006. DOI: 10.1103/RevModPhys.88.025006.

[139] R Küchler et al. "Thermodynamic evidence for valley-dependent density of states in bulk bismuth". In: *Nature materials* 13.5 (2014), p. 461.

[140] E. K. H. Salje et al. "Tin telluride: A weakly co-elastic metal". In: *Phys. Rev. B* 82 (18 2010), p. 184112. DOI: 10.1103/PhysRevB.82.184112.

[141] M. Sawicki, W. Stefanowicz, and A. Ney. "Sensitive SQUID magnetometry for studying nanomagnetism". In: *Semicon. Sci. Technol.* 26 (2011), p. 064006. DOI: 10.1088/0268-1242/26/6/064006.

[142] V. Novák et al. "Curie Point Singularity in the Temperature Derivative of Resistivity in (Ga,Mn)As". In: *Phys. Rev. Lett.* 101 (7 2008), p. 077201. DOI: 10.1103/PhysRevLett.101.077201.

[143] M. Górska and J. R. Anderson. "Magnetic susceptibility and exchange in V-VI compound diluted magnetic semiconductors". In: *Phys. Rev. B* 38 (1988), pp. 9120–9126. DOI: 10.1103/PhysRevB.38.9120.

[144] T. Dietl et al. "Mechanisms of exchange interactions between carriers and Mn or Eu spins in lead chalcogenides". In: *Phys. Rev. B* 49 (1994), p. 2230. DOI: 10.1103/PhysRevB.49.2230.

[145] O. O. Shvetsov et al. "Surface superconductivity in a three-dimensional Cd_3As_2 semimetal at the interface with a gold contact". In: *Phys. Rev. B* 99 (12 2019), p. 125305. DOI: 10.1103/PhysRevB.99.125305.

[146] C. M. Polley et al. "Observation of surface states on heavily indium-doped SnTe(111), a superconducting topological crystalline insulator". In: *Phys. Rev. B* 93 (7 2016), p. 075132. DOI: 10.1103/PhysRevB.93.075132.

[147] N. Berchenko et al. "Surface oxidation of SnTe topological crystalline insulator". In: *Appl. Surf. Sci.* 452 (2018), pp. 134 –140. DOI: 10.1016/j.apsusc.2018.04.246.

[148] Goutam Sheet, S. Mukhopadhyay, and P. Raychaudhuri. "Role of critical current on the point-contact Andreev reflection spectra between a normal metal and a superconductor". In: *Phys. Rev. B* 69 (13 2004), p. 134507. DOI: 10.1103/PhysRevB.69.134507.

[149] Qing Lin He et al. "Chiral Majorana fermion modes in a quantum anomalous Hall insulator–superconductor structure". In: *Science* 357 (2017), pp. 294–299. DOI: 10.1126/science.aag2792.

[150] Wenjie Ji and Xiao-Gang Wen. "$\frac{1}{2}(e^2/h)$ Conductance Plateau without 1D Chiral Majorana Fermions". In: *Phys. Rev. Lett.* 120 (2018), p. 107002. DOI: 10.1103/PhysRevLett.120.107002.

[151] G. E. Blonder, M. Tinkham, and T. M. Klapwijk. "Transition from metallic to tunneling regimes in superconducting microconstrictions: Excess current, charge imbalance, and supercurrent conversion". In: *Phys. Rev. B* 25 (7 1982), pp. 4515–4532. DOI: 10.1103/PhysRevB.25.4515.

[152] A. Plecenník et al. "Finite-quasiparticle-lifetime effects in the differential conductance of $Bi_2Sr_2CaCu_2O_y$/Au junctions". In: *Phys. Rev. B* 49 (14 1994), pp. 10016–10019. DOI: 10.1103/PhysRevB.49.10016.

[153] Y. Bugoslavsky et al. "Possibilities and limitations of point-contact spectroscopy for measurements of spin polarization". In: *Phys. Rev. B* 71 (10 2005), p. 104523. DOI: 10.1103/PhysRevB.71.104523.

[154] N. D. Zhigadlo et al. "Crystal growth, characterization, and point-contact Andreev-reflection spectroscopy of the noncentrosymmetric superconductor Mo_3Al_2C". In: *Phys. Rev. B* 97 (21 2018), p. 214518. DOI: 10.1103/PhysRevB.97.214518.

[155] S. D. Darchuk et al. "Phase states and magnetic structure of superconducting lead inclusions in a narrow-gap PbTe semiconducting host". In: *Semiconductors* 32 (1998), pp. 700 –703. DOI: 10.1134/1.1187487.

[156] Katarzyna Gas and Maciej Sawicki. "In situ compensation method for high-precision and high-sensitivity integral magnetometry". In: *Measurement Science and Technology* (2019). DOI: http://iopscience.iop.org/10.1088/1361-6501/ab1b03.

[157] Evelyn Tang and Liang Fu. "Strain-induced partially flat band, helical snake states and interface superconductivity in topological crystalline insulators". In: *Nat. Phys.* 10 (2014), pp. 964–969. DOI: 10.1038/nphys3109.

[158] K. Murase et al. "Superconducting behavior in PbTe–SnTe superlattices". In: *Surf. Sci.* 170 (1986), pp. 486 –490. DOI: 10.1016/0039-6028(86)91008-3.

[159] N. Ya. Fogel et al. "Direct evidence for interfacial superconductivity in two-layer semiconducting heterostructures". In: *Phys. Rev. B* 73 (2006), 161306(R). DOI: 10.1103/PhysRevB.73.161306.

[160] W.-H. Li et al. "Quantum size effects on the superconducting parameters of zero-dimensional Pb nanoparticles". In: *Phys. Rev. B* 68 (2003), p. 184507. DOI: 10.1103/PhysRevB.68.184507.

[161] C. T. Black, D. C. Ralph, and M. Tinkham. "Spectroscopy of the Superconducting Gap in Individual Nanometer-Scale *Aluminum* Particles". In: *Phys. Rev. Lett.* 76 (1996), pp. 688–691. DOI: 10.1103/PhysRevLett.76.688.

[162] M. F. Merriam and M. Von Herzen. "Superconductivity in the Indium-Tin System". In: *Phys. Rev.* 131 (1963), pp. 637–643. DOI: 10.1103/physrev.131.637.

[163] P. Sessi et al. "Robust spin-polarized midgap states at step edges of topological crystalline insulators". In: *Science* 354 (2016), pp. 1269–1273. DOI: 10.1126/science.aah6233.

[164] Craig M. Polley et al. "Fragility of the Dirac Cone Splitting in Topological Crystalline Insulator Heterostructures". In: *ACS Nano* 12.1 (2018). PMID: 29251489, pp. 617–626. DOI: 10.1021/acsnano.7b07502.

[165] V. V. Volobuev et al. "Topological Crystalline Insulator Films Controlled by Bi Doping in the Bulk". In: *Adv. Mater.* 29 (2017), p. 1604185. DOI: 10.1002/adma.201604185.

[166] Raymond T. Tung. "The physics and chemistry of the Schottky barrier height". In: *Appl. Phys. Rev.* 1 (2014), p. 011304. DOI: 10.1063/1.4858400.

[167] S. Kundu and V. Tripathi. "Role of Hund's splitting in electronic phase competition in $Pb_{1-x}Sn_xTe$". In: *Phys. Rev. B* 96 (20 2017), p. 205111. DOI: 10.1103/PhysRevB.96.205111.

[168] S. Kundu and V. Tripathi. "Competing effects of Hund's splitting and symmetry-breaking perturbations on electronic order in Pb _{1 − x} Sn _{x} Te". In: *arXiv preprint arXiv:1709.02322* (2017). DOI: https://arxiv.org/abs/1709.02322.

[169] Xiao-Liang Qi, T. L. Hughes, and Shou-Cheng Zhang. "Chiral topological superconductor from the quantum Hall state". In: *Phys. Rev. B* 82 (2010), p. 184516. DOI: 10.1103/PhysRevB.82.184516.

[170] K.Yu. Arutyunov, D.S. Golubev, and A.D. Zaikin. "Superconductivity in one dimension". In: *Phys. Reports* 464 (2008). DOI: 10.1016/j.physrep.2008.04.009.

[171] K. Byczuk and T. Dietl. "Realistic electron-electron interaction in a quantum wire". In: *Phys. Rev. B* 60 (1999), pp. 1507–1510. DOI: 10.1103/PhysRevB.60.1507.

[172] T. Dietl et al. "Carrier-mediated ferromagnetic interactions in structures of magnetic semiconductors". In: *Mater. Sci. Eng. B* 63 (1999), pp. 103 –110. DOI: 10.1016/S0921-5107(99)00059-8.

[173] J.-P. Pouget. "The Peierls instability and charge density wave in one-dimensional electronic conductors". In: *C. R. Physique* 17 (2016), pp. 332–356. DOI: 10.1016/j.crhy.2015.11.008.

[174] J. Appelbaum. "'"$s - d$" Exchange Model of Zero-Bias Tunneling Anomalies". In: *Phys. Rev. Lett.* 17 (1966), pp. 91–95. DOI: 10.1103/PhysRevLett.17.91.

[175] P. W. Anderson. "Localized Magnetic States and Fermi-Surface Anomalies in Tunneling". In: *Phys. Rev. Lett.* 17 (1966), pp. 95–97. DOI: 10.1103/PhysRevLett.17.95.

[176] B. L. Al'tshuler and A. G. Aronov. "Contribution to the theory of disordered metals in strongly doped semiconductors". In: *Sov. Phys. JETP* 50 (1979), pp. 968–976.

[177] A. L. Efros and B. I. Shklovskii. "Coulomb gap and low temperature conductivity of disordered systems". In: *J. Phys. C* 8 (1975), pp. L49–L51. DOI: 10.1088/0022-3719/8/4/003.

[178] Y. Meir, N. S. Wingreen, and Patrick A. Lee. "Low-temperature transport through a quantum dot: The Anderson model out of equilibrium". In: *Phys. Rev. Lett.* 70 (1993), pp. 2601–2604. DOI: 10.1103/PhysRevLett.70.2601.

[179] M. Pustilnik and L. I. Glazman. "Kondo Effect in Real Quantum Dots". In: *Phys. Rev. Lett.* 87 (2001), p. 216601. DOI: 10.1103/PhysRevLett.87.216601.

[180] W. Brzezicki, M. M. Wysokiński, and T. Hyart. "Complete description of symmetry-protected topological properties of $Sn_{1-x}Pb_xTe_{1-y}Se_y$ multilayers with a step edge". In: *arXiv:1812.02168* (2018).

[181] D. Iaia et al. "Topological nature of step edge states on the surface of topological crystalline insulator $Pb_{0.7}Sn_{0.3}Se$". In: *arXiv:1809.10689* (2018).

[182] R. Rechciński and R. Buczko. "Topological states on uneven (Pb,Sn)Se (001) surfaces". In: *Phys. Rev. B* 98 (2018), p. 245302. DOI: 10.1103/PhysRevB.98.245302.

[183] A. J. Heeger et al. "Solitons in conducting polymers". In: *Rev. Mod. Phys.* 60 (3 1988), pp. 781–850. DOI: 10.1103/RevModPhys.60.781.

[184] S. Kundu and V. Tripathi. "Chiral p-wave superconductivity in $Pb_{1-x}Sn_xTe$: Signatures from bound-state spectra and wave functions". In: *Phys. Rev. B* 99 (20 2019), p. 205105. DOI: 10.1103/PhysRevB.99.205105.

[185] Yuan Cao et al. "Unconventional superconductivity in magic-angle graphene superlattices". In: *Nature* 556.7699 (2018), p. 43. DOI: 10.1038/nature26160.